Journal of Research of the National Bureau of Standards Vol. 45, No. 2, August 1950 Research Paper 2116

Cotton Powder for Infrared Transmission Measurements[1]

By Florence H. Forziati, Walter K. Stone, John W. Rowen, and William D. Appel

Cotton cut in a Wiley mill to pass a 20-mesh screen was ground in a vibratory ball mill similar to one that has been used in Germany and Holland. Contamination of the cotton was practically eliminated by using a chromium-plated hardened steel jar and chromium alloy balls. The jar holder is held by a slip ring instead of being bolted in place. The jar and holder automatically rotate slowly on their axis, and this motion counteracts the tendency of the cotton in the jar to settle and grind nonuniformly. The jar is cooled by blowing air over it and becomes barely warm to the touch.

Five grams of dried cotton disintegrated rapidly during the first 15 minutes of milling. The largest particles remaining after 30 minutes of milling were about 10 microns in major dimension, and there was little reduction of the maximum size with longer milling. Cuprammonium fluidity of the cotton increased rapidly in the first hour of milling and more gradually thereafter. The carboxyl content of the cotton increased very slowly with time of milling and reached only about 0.2 percent after 8 hours. The moisture regain of the cotton at 65-percent relative humidity at 21° C increased rapidly during the first hour of milling, from 7.1 to 12.5 percent, and then remained practically constant. X-ray diffraction measurements showed that the cellulose was converted almost completely to the amorphous form in 30 minutes, and that it underwent little change thereafter.

The powdered cotton obtained from the vibratory ball mill was mulled in mineral oil. The resulting paste was injected into rock salt cells for infrared absorption measurements. The powder worked reasonably well in this procedure, distinctly better than the coarse powders obtained by other methods of grinding. No significant differences were found in the infrared absorption of a regenerated cellulose film, the cotton ground in a Wiley mill to 200 mesh, and cotton ground in the vibratory ball mill for periods of time from 15 minutes to 8 hours.

It is concluded that the vibratory ball mill, as modified, reduces cotton, rapidly and completely, to a very fine powder, suitable for infrared transmission measurements and other purposes. Milling results in practically negligible oxidation of the cellulose, but in a marked decrease in degree of polymerization, and in almost complete conversion of crystalline to amorphous cellulose.

I. The Problem

The first problem arising in the attempt to apply infrared spectrophotometry to cotton cellulose was to prepare the cotton in a form suitable for introduction into the beam of the spectrophotometer. Microspectrophotometers applicable to single cotton fibers were not available at the time the work was started, though promising instruments are now being developed [1, 2, 3, 4].[2] Spectra obtained from fibers laid side by side were not encouraging. Preparation of films from the cotton, for example by converting it to cellulose acetate and then, as in previous work [5], casting a film and deacetylating it, did not seem to answer the problem, not only because of the changes in structure that would result but because such a procedure would not be applicable to some degraded cottons. It was, therefore, decided to try to reduce the fibers to a powder and measure the absorption of the powder in a mat or in suspension in a suitable liquid.

Several well-known methods for grinding materials were tried. They included grinding in a Wiley mill in which the material is cut between fixed and rapidly moving blades, in a ball mill using both stone and steel balls in a porcelain jar, and in a Waring Blendor. An ultrasonic generator, operating at 8 kc and 250 ma, was tried. The products obtained by these methods contained much coarse material. A method that would reduce the entire sample to a finely divided state, without contamination and with a minimum of chemical change, was desired.

The work of Hermans and Weidinger [6] on cellulose, ground in a vibratory ball mill, suggested the possibility of this type of machine for this purpose. This mill appeared to be quite different in its grinding action from an ordinary ball mill [7]. Examination of a sample of rayon ground in this type of mill led to the construction of a similar mill. Several changes in construction were made in order to fit the mill for this work.

This report describes the mill and discusses the changes that cotton underwent when ground in it.

II. Vibratory Ball Mill

Descriptions of the vibratory ball mill, the principle of its action, and a mathematical analysis of the motions of the balls in it, have been published by Kiesskalt [7] and Bachmann [8]. Therefore, only a brief description of the mill built at the National Bureau of Standards is given here.[3]

The mill is illustrated in figures 1, 2, and 3. It consists of a horizontal shaft connected at one end, by means of a flexible coupling, to a ¼-horsepower motor having a speed of 1,800 rpm, and at the other to an eccentric weight. The weight rotates in a

[1] A report of work done under cooperative agreement with the United States Department of Agriculture and authorized by the Research and Marketing Act. The agreement is being supervised by the Southern Regional Research Laboratory of the Bureau of Agricultural and Industrial Chemistry.

[2] Figures in brackets indicate the literature references at the end of this paper.

[3] Working drawings of the mill built at the National Bureau of Standards may be obtained upon request to the National Bureau of Standards, Textiles Section, Washington 25, D. C.

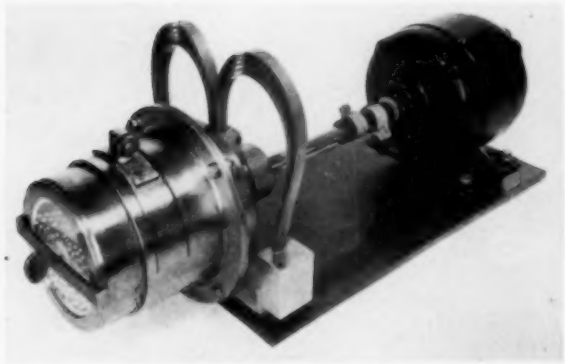

FIGURE 1. *Vibratory ball mill.*

Jar shown with transparent plastic cover instead of chromium-plated steel cover; safety guard removed from shaft.

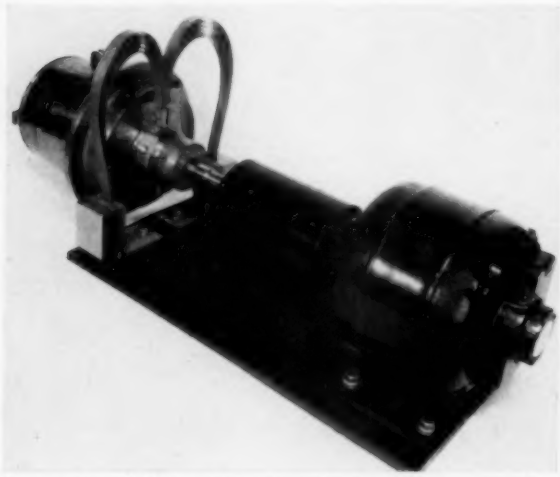

FIGURE 2. *Vibratory ball mill, showing spring suspension; safety guard for shaft in position.*

housing suspended from leaf springs. A cylindrical jar of approximately 1-liter capacity slips into a holder attached to the housing. The housing, with attached holder and jar, is moved in a circular path by the rotation of the eccentric weight. Steel balls in the jar are set into rapid motion by this movement, and their collisions grind the material placed in the jar with them.

The cellulose milled in P. H. Hermans' mill contained inorganic material from the ceramic jar. Hermans suggested the use of steel balls to reduce contamination. Not only was this done, but the jar was machined from a solid block of Stentor tool steel. Trial runs were carried out with this jar, three-fourths full of ¼-in. steel balls, on 5-g samples of cotton, previously ground in a Wiley mill to pass a 20-mesh screen. At the close of a 3-hr run, the balls had lost their polish, while the sample was gray in color and contained about 0.4 percent by weight of iron.

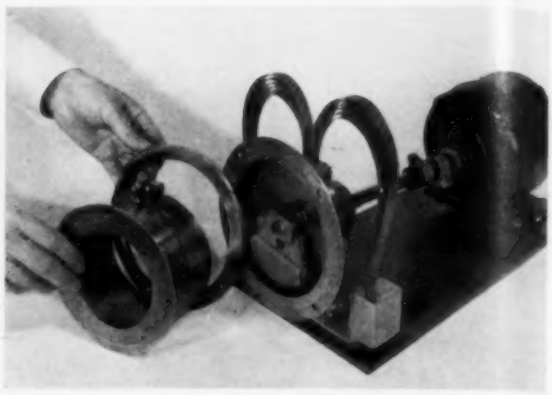

FIGURE 3. *Vibratory ball mill, partly disassembled to show, from left to right, the jar holder, slip ring, and eccentric weight on the end of the shaft in the weight housing.*

The jar was then hardened to "C" 61 Rockwell and chromium plated. The steel balls were replaced with chrome alloy balls of hardness of approximately "C" 64. With this combination, the contamination of 5g of cotton was less than 0.05 percent in a run of 8 hr.

Experience with the mill showed that the material being ground tended to settle to the lower side of the jar. In order to insure uniform pulverization, it was necessary to stop the machine at frequent intervals and redistribute the contents of the jar by rotating it 180 degrees. Observations, through a plastic cover, showed that the balls moved slowly in a direction opposite to that of the eccentric weight. This suggested that the jar might rotate in the same direction as the balls if it were free to do so and thus automatically redistribute the charge. Accordingly, a slip ring, shown in figures 1 and 3, was substituted for the bolts with which the jar holder was originally attached to the weight housing. With this change, the jar rotates at a rate of approximately 1 rpm, and the material being ground does not settle out.

III. Changes in Cotton During Grinding

Empire cotton (lot AP845), supplied by the Southern Regional Research Laboratory, U. S. Department of Agriculture, was used in studying the effects of milling in the modified vibratory ball mill. This cotton was extracted for 8 hr in a Soxhlet with ethanol, washed with distilled water, dried in air at room temperature, and ground in a Wiley mill to pass a 20-mesh screen. Five-gram specimens were then dried for 1 week over magnesium perchlorate and placed in the jar of the vibratory mill with enough ¼-in. chrome-steel balls to fill it three-fourths full. In order to minimize heating of the cotton during grinding, a fan was used to blow the room air over a jar. Without this cooling, the temperature of the jar and balls rose to 65° C and higher in 3 hr of continuous milling. With the cooling, the jar was barely warm to the touch at the end of 8 hr. Cotton milled for periods of time

ranging from 15 min to 8 hr, was examined with respect to particle size, fluidity in cuprammonium solution, carboxyl content, and moisture regain after exposure to air at 65-percent relative humidity at 21° C. In addition, X-ray diffraction and infrared transmission measurements were made. The results follow.

1. Particle Size

Microscopic examination of the products mulled in a water-white mineral oil, figure 4, showed that the fibers disintegrated rapidly during the first 15 min of milling. Some relatively large fragments were present after 15 min, but not after 30 min, of milling. The largest particles remaining after 30 min were about 10 μ in major dimension. There was little or no reduction of the maximum size of the particles with longer milling. Although mulling produced a limited amount of fiber disintegration, it was used in the microscopic work to overcome the tendency of the particles of the milled samples to form aggregates.

2. Cuprammonium Fluidity

The fluidity of the products in cuprammonium solution, measured by the Wilson and Launer modification of the standard method [9], is shown in table 1 and figure 5. An extremely rapid decrease in the length of the cellulose chains is indicated by the increase in fluidity. This is in agreement with the results reported by Hess and his coworkers [10, 11, 12]. They showed that the kinetic energy of the balls is converted directly into molecular vibrational energy of the material under impact. In addition, they found the degradation, as measured by solution viscosity, to be independent of the temperature of milling between 0° and 90° C.

TABLE 1. *Effects of the milling on cotton*

Milling period	Cuprammonium fluidity	Carboxyl	Moisture regain [a]
Hours	*Rhes*	*Percent* [b]	*Percent*
0	5.4	0.00	7.1
¼	15.2	.03	10.3
½	25.3	.03	11.9
¾	30.4	.03	12.0
1	36.9	.03	12.7
2	46.1	.08	12.6
4	51.9	.11	12.8
8	57.7	.22	12.5

[a] At 65% relative humidity and 21° C.
[b] Calculated on oven-dray basis.

3. Carboxyl Content

The carboxyl contents of the products, determined by the method of Yackel and Kenyon [13], are shown in table 1 and figure 5. The increase in carboxyl content in the first hour of milling was extremely small. The small increase in 8 hr of milling supports the view of Hess and his coworkers [10, 11] that the effect of this type of milling on the cellulose is primarily mechanical.

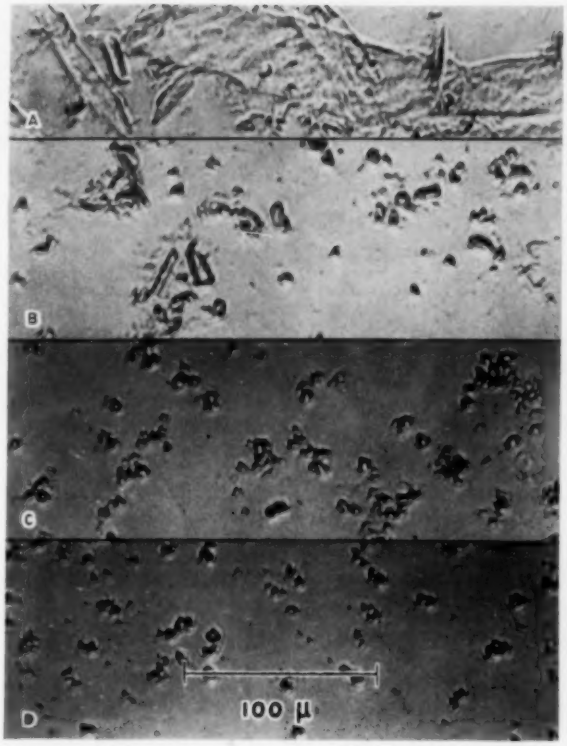

FIGURE 4. *Cotton that has been ground and then mulled in mineral oil.*

A, Ground in Wiley mill to pass 20-mesh screen; *B*, as in *A* and, in addition, ground in vibratory ball mill for 15 minutes; *C*, as in *B* but ground in vibratory ball mill for 30 minutes; *D*, as in *B* but ground in vibratory ball mill for 1 hour.

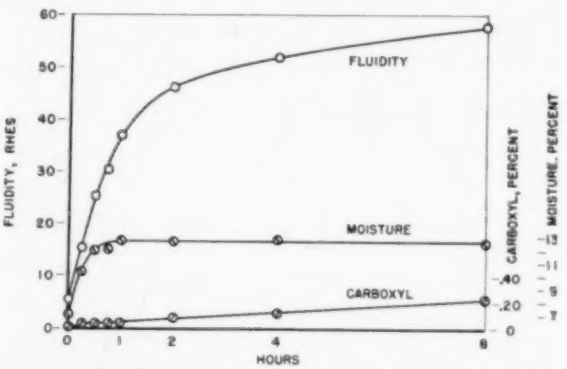

FIGURE 5. *Cuprammonium fluidity, moisture regain at 65-percent relative humidity at 21° C, and carboxyl content of cotton verses time of milling in the vibratory ball mill.*

4. Moisture Regain

The moisture regain of the powders when exposed to air of 65-percent relative humidity at 21° C after grinding, table 1 and figure 5, increased rapidly during the first hour of milling, from 7.1 to 12.5

percent, and remained practically constant with increase in time of milling up to 8 hr. The moisture capacity of cellulose is generally considered to be proportional to the amorphous fraction of the cellulose. If this is so, the milling increased the proportion of amorphous cellulose in the sample. The fact that no substantial increase in moisture regain occurred after the first hour of milling indicates that the crystalline material was converted to noncrystalline during the first hour.

5. X-Ray Diffraction

X-ray diffraction patterns of the powders, figure 6, were obtained with a Geiger counter spectrometer, operating at 40 kv and 15 ma and using copper radiation, $\lambda = 1.54050$ A. The powders were packed in a flat specimen holder 0.8 mm deep and 13.5 mm in diameter.

A rapid and profound change in the X-ray diffraction pattern of the cotton resulted from milling in the vibratory ball mill. The 20-mesh control sample gave the X-ray diffraction pattern characteristic of the crystal lattice of cellulose I (native cellulose). The patterns obtained with samples that were milled for periods of time ranging from 30 min to 8 hr showed only the broad diffuse band characteristic of amorphous cellulose [14]. The position of the bands in the pattern of the sample that had been milled for 15 min indicates that cellulose II (mercerized cellulose) is formed during the early stages of milling in the vibratory ball mill and is then converted to amorphous cellulose.

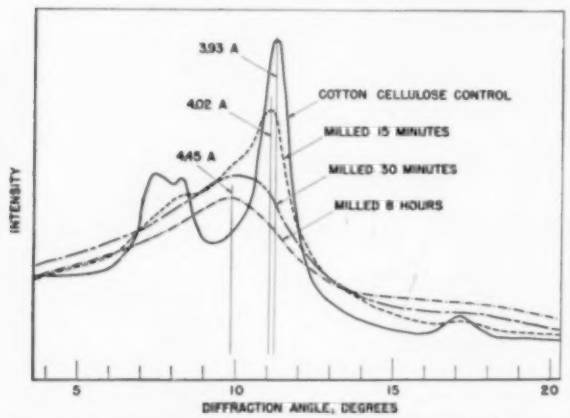

FIGURE 6.—*X-ray diffraction patterns of cotton that has been ground in the Wiley mill to pass a 20-mesh screen and then in the vibratory ball mill for 15 minutes, 30 minutes, and 8 hours.*

The figures shown on the curves give the interplanar spacings corresponding to the most intense bands.

6. Infrared Absorption

The powders were prepared for infrared absorption studies by mulling in water-white mineral oil and injecting into demountable rock salt cells.

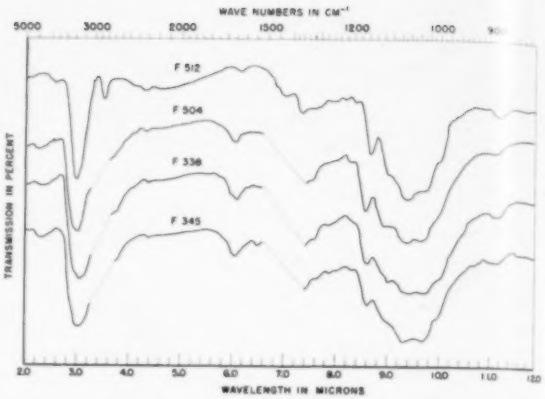

FIGURE 7. *Infrared absorption spectra.*

Dotted lines are shown in the regions obscured by the absorption of the mineral oil. F512, Regenerated cellulose film; F504, cotton ground in Wiley mill to pass 200-mesh screen and then mulled in mineral oil; F338, cotton ground in vibratory ball mill for 15 minutes and then mulled in mineral oil; F345, same as F338 except that cotton was ground in the vibratory ball mill for 8 hours.

Cells of two or more thicknesses were used for each powder. Spectra, figure 7, were obtained with a Baird spectrophotometer. The results show no significant differences between cotton that had been ground in a Wiley mill to pass a 200-mesh [4] screen, cotton that had been ground in the vibratory ball mill for periods of time ranging from 15 min to 8 hr, and a film of regenerated cellulose [5]. Thus, such functional groups as may be introduced by milling the cotton in the vibratory ball mill are not detectable in the infrared absorption spectrum. The absence of an absorption band at 5.75 μ, the region of the spectrum in which the C=O of the carboxyl groups absorbs, is in agreement with the very low values for carboxyl content, obtained by chemical means. Such decreases in degree of polymerization as are indicated by the cuprammonium fluidities would not be expected to result in changes in infrared absorption. Thus, the infrared absorption measurements constitute additional evidence for the conclusion of Hess and his coworkers [10] that the degradation produced by the mill is hydrolytic rather than oxidative. The possibility is not eliminated, however, that oxidation may have resulted in the formation of groups that were not detected by the infrared absorption measurements.

IV. Conclusions

The results indicate that the vibratory ball mill, as modified, reduces the cotton rapidly and completely to a very fine powder suitable for infrared transmission measurements and other purposes. Milling results in practically negligible oxidation of the cellulose, but in a marked decrease in degree of polymerization and in conversion of crystalline to amorphous cellulose.

[4] Due to excessive scattering of light, absorption measurements could not be made on the 20-mesh control.

The authors express their appreciation of the help received from P. H. Hermans, Utrecht, The Netherlands. He ground material for us in his mill and supplied drawings of the mill. The authors are indebted to the machine shop of the Bureau for assistance in the design and construction of the mill at the Bureau, to Sanford Newman and Emil Borysko for the preparation of photomicrographs, and to Howard E. Swanson for the X-ray diffraction patterns.

V. References

[1] C. R. Burch, Proc. Phys. Soc. **59,** 1, 47 (1947).
[2] R. Barer, A. R. H. Cole, and H. W. Thompson, Nature **163,** 198 (1949).
[3] E. R. Blout, G. R. Bird, and D. S. Grey, J. Opt. Soc. Am. **40,** 304 (1950).
[4] L. V. Foster, Anal. Chem. **21,** 432 (1949).
[5] J. W. Rowen, C. M. Hunt, and E. K. Plyler, J. Research NBS **39,** 133 (1947) RP1816.
[6] P. H. Hermans and A. Weidinger, J. Am. Chem. Soc. **68,** 2547 (1946).
[7] S. Kiesskalt, Z. Ver. Deut. Ing. Beih. Verfahrenstechnik **1936,** No. 1, 1 and DRP 619,662; 620,721.
[8] D. Bachmann, Z. Ver. Deut. Ing. Beih. Verfahrenstechnik **1940,** No. 2, 43.
[9] H. F. Launer and W. K. Wilson, Anal. Chem. **22,** 455 (1950).
[10] K. Hess, H. Kiessig, and J. Gundermann, Z. Physik. Chem. **B49,** 64 (1941).
[11] K. Hess, E. Steurer, and H. Fromm, Kolloid Z. **98,** 148, 290 (1942).
[12] K. Hess, Z. Ver. Deut. Ing. Beih. Verfahrenstechnik **1943,** 61; Chem. Zentr. **1944,** I, 6 and Chem. Abs. **39,** 2905[9] (1945).
[13] E. C. Yackel and W. O. Kenyon, J. Am. Chem. Soc. **64,** 121 (1942).
[14] P. H. Hermans and A. Weidinger, Bul. Soc. Chim. Belg. **57,** 123 (1948).

WASHINGTON, April 30, 1950.

Journal of Research of the National Bureau of Standards Volume 45, No. 2, August 1950 Research Paper 2117

Gravimetric Analysis of Exhaust Gas From Gas Turbine Combustion Chambers[1]

By Fillmer W. Ruegg and Carl Halpern

Because of the high air-fuel ratio used in combustion chambers of gas turbines, the concentration of products of combustion is so low that standard volumetric methods of analysis have proved unreliable. A gravimetric method of anaylsis was developed and applied to the problem, not to identify all of the constituents, but primarily to determine the efficiency of the combustion process. In this method the products of complete combustion, water and carbon dioxide, are separated from each other and from the remainder of the sample, which is then passed into a furnace to burn the combustible components. Carbon dioxide and water are determined by change of weight of solid absorbents. Experiments showed that the method may be used to provide accurate information about the magnitude of the loss of heat due to incomplete combustion, and partial information about the nature of the components of the exhaust gas.

I. Introduction

The primary objective of application of the combustion process in combustion chambers of gas turbines, and in fact in nearly all of its applications, is the release of energy in the fuel to heat the working fluid from its initial to its final temperature. Change of temperature of the working fluid is an indication of its enthalpy change, but temperature alone is inadequate to relate this enthalpy change to the energy available in the fuel. In order to obtain such a relation, calculation of a heat balance involving rates of flow as well as temperature must be made. It is inconvenient or perhaps impossible in some cases to make accurate measurements of these quantities, and it is in such instances that gas analysis may be called upon to supply the desired information about the efficiency of the combustion process. Even in cases where the heat balance can be calculated from experimental data, the measurements are subject to uncertainties, and an accurate method of analysis of the exhaust gas is useful as an independent check. The analysis also provides information regarding the nature of the components of the exhaust, which may be useful in the design and development of combustion chambers.

Accurate analysis of exhaust gases from gas turbine combustion chambers is difficult because the fuel is burned with so much excess air that the concentration of the products of combustion is very low. Because of this dilution the more common methods of analysis, such as that employed in Orsat instruments, have proved unreliable. Gravimetric methods of analysis are known to afford precise results when dealing with small quantities, and it appeared that such methods could be applied to the problem of analysis of exhaust gas from combustion chambers for gas turbines. Jordan and Eckman [1][2] used gravimetric methods for the determination of gases in metals. The application to analysis of exhaust gas would depend on efficient separation of the prod-

[1] The work described in this report was sponsored by the Bureau of Aeronautics, Department of the Navy.

[2] Figures in brackets indicate the literature references at the end of this paper.

ucts of complete combustion, namely water and carbon dioxide, from each other and from the remainder of the sample. It was proposed to make the separation by using solid reagents to absorb water and carbon dioxide, and then to burn the combustibles remaining in the gas in a furnace over copper oxide. Water and carbon dioxide formed by combustion could then be separated and absorbed similarly. Use of a relatively large volume of sample would serve to minimize effects of errors in weighing on the accuracy of the determinations.

Separate determination of carbon monoxide, and relation of the amount so determined to the carbon dioxide and water produced by combustion in the furnace, was introduced to make the analysis more complete. Calculation of combustion efficiency from data of this type is possible, and the accuracy of the efficiency so calculated depends primarily on the completeness of separation of the various components and on the accuracy of the determination of the amounts of carbon dioxide and water before and after the treatment in the furnace. It was not proposed to identify and determine the quantity of each component of the exhaust gas, because it was considered that the time consumed and equipment required for such determinations would be prohibitive.

It is recognized that sampling technique is important if an accurate picture of the combustion process is to be had by gas analysis. As the primary interest was in the analytical technique, sampling was done to give an average sample rather than a picture of the combustion process at any particular point. The samples were taken at positions in the combustion systems where concentration gradients in the gas were at a minimum, the gas temperature was low enough that combustion reactions were probably stopped, and the problem of continued reaction in the water-cooled sampling probes did not arise.

The first application of the method at this laboratory was made in 1944, and since that time the investigation has been continued to determine the accuracy and the most efficient form of application of the method.

II. Combustion Efficiency

As one of the primary objects of exhaust-gas analysis is the determination of the efficiency of the combustion process, it is desirable to specify what is meant by combustion efficiency and what is required for its calculation. The primary interest in combustion problems is in the increase of enthalpy of the working fluid, and consequently combustion efficiency is usually expressed in terms of heat quantities, or in terms that are related to heat quantities. Numerous definitions have been proposed, and three that are commonly used are

$$\eta_b = \frac{\Delta h_{\text{actual}}}{\Delta h_{\text{ideal}}} \tag{1}$$

$$\eta_b = \frac{\Delta T_{\text{actual}}}{\Delta T_{\text{ideal}}} \tag{2}$$

$$\eta_b = \frac{f_{\text{ideal}}}{f_{\text{actual}}} \tag{3}$$

The first definition relates the actual to the ideal change o enthalpy, and this has been considered the orthodox definition. In practice, Δh_{actual} is evaluated from a knowledge of the initial temperature of fuel and air and the temperature of the products of combustion, and from a knowledge of the specific heats of the components of the exhaust gas. Usually it is necessary to assume a composition, and the accuracy of the assumption will affect the accuracy of the evaluation of η_b. For many purposes, the assumption is made that the actual products have the same enthalpy-temperature relation as the products of complete combustion. The ideal change of enthalpy is generally replaced by the heat of complete combustion of the fuel, and therefore this definition is one that may be described as based on "stoichiometric" completeness. Heat of combustion of the fuel may be defined in several different ways, and generally the heating va'ue for combustion at constant pressure is used. There is no general agreement about the choice between the lower and upper heating value, and opinions differ whether these enthalpy changes should be evaluated with respect to some standard re'erence temperature, T_0, or to the initial temperature, T_1, of the reactants.

The second definition may be considered an approximation of the first. The third definition, which was proposed by A. L. London [2], relates the ideal amount of fuel required to produce the observed temperature after combustion to the actual amount of fuel burned. These definitions are used by some investigators in the field of combustion. Where the temperature of the products of combustion is high enough to cause dissociation of the carbon dioxide, water, oxygen and nitrogen, some investigators prefer to base the ideal rise of temperature or ideal fuel on the temperature that the gases attain when dissociation is considered and when equilibrium is established among the constituents of the exhaust gas. This is often referred to as "thermodynamically" complete combustion, and at temperatures over 1,550° K, η_b based on thermodynamic completeness will differ substantially from that based on stoichiometric completeness.

This brief discussion has indicated that there is no general agreement about the definition of combustion efficiency and that each can be calculated in various ways. Fortunately, it is unnecessary to further complicate the situation by injecting a different definition derived from data of chemical analysis. Equation 1 may be used as the basis for defining η_b with suitable rearrangement to accommodate the type of data obtained from chemical analysis. Equations 2 and 3 require calculations that are lengthy and more complex.

For the purpose of these calculations, it may be assumed that the air and fuel are brought together at temperatures T_a and T_f, respectively, and that the weight ratio of fuel to air is f. Further, it may be assumed that the air and fuel mix at constant pressure with no change of phase and arrive at a common temperature T_1. A heat balance equation may be set up,

$$f[h_f]_{T_f}^{T_1}=[h_a]_{T_1}^{T_a} \tag{4}$$

and this may be solved for T_1. After the fuel and air mix, it is assumed that combustion takes place at constant pressure and that products of combustion of amount $(1+f)$ are formed.

Equation 1 may be written in the form

$$\eta_b=\frac{\Delta h_{\text{actual}}}{\Delta h_{\text{ideal}}}=\frac{(1+f)[h_b]_{T_1}^{T_2}}{-f(\Delta Hc)_{T_1}}, \tag{5}$$

which states that η_b is the change of enthalpy of the products of combustion divided by the specific lower heat of combustion of the fuel for isothermal constant pressure reaction at the initial temperature. The negative sign indicates an exothermic reaction. It can be considered that the reaction takes place in two steps, the first of which is an isothermal reaction forming the actual products of combustion, and the second step is one in which the heat of the isothermal reaction is applied to the products to raise them to temperature T_2. Thus the numerator of eq 5 may be written

$$(1+f)[h_b]_{T_1}^{T_2}=-(\Delta H_{\text{actual}})_{T_1}, \tag{6}$$

where $(\Delta H_{\text{actual}})_{T_1}$ is the heat of reaction at T_1, in which the actual products of amount $(1+f)$ are formed. In the real case, combustion is not complete, and the heat that can still be produced by continued reaction is determined by the difference between the heat of combustion of the fuel and the actual heat of reaction. Thus if the products of incomplete combustion were caused to react to completion at temperature T_1, the heat of this reaction would be determined by

$$(\Delta H)_{T_1}=f(\Delta Hc)_{T_1}-(\Delta H_{\text{actual}})_{T_1} \tag{7}$$

If eq 7 is solved for $(\Delta H_{\text{actual}})_{T_1}$ and if its value is substituted in eq 5, η_b will be defined by

$$\eta_b=1-\frac{(\Delta H)_{T_1}}{f(\Delta Hc)_{T_1}}, \tag{8}$$

which is approaching a form amenable to application of data from exhaust gas analysis.

If all of the components of exhaust gas could be identified and determined quantitatively, it would be only necessary to find in the literature the values of the heat of reaction (or combustion) of the various components, and enter these values in the numerator, weighted according to the relative amounts of each. However, a complete determination of all the components would be extremely difficult, and some other means of arriving at a satisfactory answer is necessary. By standard thermochemical procedure we may write for oxidation of the combustible material

$$\left.\begin{aligned}-(\Delta H)_{T_1}=&-(\Sigma\Delta Hf_{\text{products}}-\Sigma\Delta Hf_{\text{combustibles}})_{T_0}\\&+[h_{\text{combustibles}}]_{T_0}^{T_1}-[h_{\text{products}}]_{T_0}^{T_1}\end{aligned}\right\}, \tag{9}$$

and for the fuel

$$\left.\begin{aligned}-f(\Delta Hc)_{T_1}=&-(\Sigma\Delta Hf_{\text{products}}-\Sigma\Delta Hf_{\text{fuel}})_{T_0}\\&+[h_{\text{fuel}+o_2}]_{T_0}^{T_1}-[h_{\text{products}}]_{T_0}^{T_1}\end{aligned}\right\}, \tag{10}$$

where ΔHf is the heat of formation. The amounts of products and reactants are determined by the chemical equation for the complete oxidation of combustible and of fuel in amount f. Substitution of eq 9 and 10 in eq 8 leads to

$$\eta_b=1-\frac{-(\Sigma\Delta Hf_{\text{prod.}}-\Sigma\Delta Hf_{\text{comb.}})_{T_0}+[h_{\text{comb.}+o_2}]_{T_0}^{T_1}-[h_{\text{prod.}}]_{T_0}^{T_1}}{-(\Sigma\Delta Hf_{\text{prod.}}-\Sigma\Delta Hf_{\text{fuel}})_{T_0}+[h_{\text{fuel}+o_2}]_{T_0}^{T_1}-[h_{\text{prod.}}]_{T_0}^{T_1}}. \tag{11}$$

The magnitude of the change of heat of combustion with temperature for some of the more common fuels and products of combustion was calculated, and it was found that the change is small. The most extreme change, for hydrogen, is only about 3½ percent over the range from 0° to 1,000° K. Hence this effect may usually be neglected, and the enthalpy terms of eq 11 may thus be ignored.

Obviously, if the combustibles are not identified, it is not possible to use the value of their heats of formation, and hence it is necessary either to neglect this term in the numerator of eq 11, or to estimate its value. The heat of combustion of saturated hydrocarbons is generally about 90 to 97 percent of the sum of the heats of formation of their products of combustion. If for these hydrocarbons, the sum of the heats of formation of their products is used in eq 11 and if their heats of formation are ignored, an error will be introduced, amounting to about 0.03 percent to 0.1 percent for every 1 percent of combustion loss due to these compounds. In the case of olefins the error will be smaller, and for acetylene, the error thus introduced will amount to about 0.2 percent, but it is doubted that acetylene is present in exhaust gas in any significant amount. For partially oxidized compounds, such as carbon monoxide and formaldehyde, the error will be still larger, but these compounds may be identified and their quantity determined with relative ease, and the correct values can be used in the equation for η_b.

From these considerations, eq 11 may be reduced to

$$\eta_b = 1 - \left(\frac{\Sigma \Delta H f_{\text{products from combustibles}}}{\Sigma \Delta H f_{\text{products from fuel}}} \right) r_c \qquad (12)$$

The heats of formation of carbon dioxide and water are well established and are listed below:

$$C + O_2 \rightarrow CO_2,\ \Delta H_{298.15°K} = -2{,}137 \text{ cal/g } CO_2,$$

$$H_2 + \frac{1}{2} O_2 \rightarrow H_2O,\ \Delta H_{298.16°K} = -3{,}208 \text{ cal/g } H_2O.$$

All products and reactants are gaseous, except carbon, which is graphite. These heat values are listed on a weight basis, since the components are determined by weight in the analysis.

Let it be assumed that the weight of carbon dioxide originally in the exhaust gas sample, and the weight of carbon dioxide and water from combustion of unburned material have been determined. With this information, eq 12 may be written

$$\eta_b = 1 - \frac{2137\ (\text{wt } CO_2) + 3208\ (\text{wt } H_2O)}{2137\ (\text{wt total } CO_2) + 3208\ (\text{wt total } H_2O)}, \qquad (13)$$

where the terms in the numerator are from the unburned material, and the weight of total carbon dioxide is the sum of the carbon dioxide originally in the sample and the carbon dioxide from the unburned material. The quantity of total water is not determined experimentally but is calculated from the hydrogen and carbon content of the fuel. All terms of this equation may be divided by the heat of formation of carbon dioxide, which leads to

$$\eta_b = 1 - \frac{(\text{wt } CO_2) + 1.50(\text{wt } H_2O)}{(\text{wt total } CO_2) + 1.50\ (\text{wt total } H_2O)}. \qquad (14)$$

Carbon monoxide is present in exhaust gas in relatively large quantity, and therefore it is necessary to correct for it. Let it be assumed that a separate analysis has determined the quantity of carbon dioxide from combustion of carbon monoxide. The ratio of the heat of combustion of carbon monoxide to the heat of formation of carbon dioxide is 0.719, and hence eq 14 may be corrected to the following:

$$\eta_b = 1 - \frac{0.719\ (\text{wt } CO_2 \text{ from CO}) + (\text{wt } CO_2 - \text{wt } CO_2 \text{ from CO}) + 1.50\ (\text{wt } H_2O)}{\text{wt total } CO_2 + 1.50\ (\text{wt total } H_2O)}. \qquad (15)$$

Similar modifications to eq 14 may be made for other compounds if the necessary information is determined about their quantity.

If the volume fractions of carbon dioxide and carbon monoxide in a gas sample are known in addition to the weight of free carbon dioxide, then the amount of carbon dioxide from combustion of the carbon monoxide may be calculated by the following equation:

$$\text{wt } CO_2 \text{ from CO} = \frac{\text{vol CO}}{\text{vol } CO_2} (\text{wt } CO_2). \qquad (16)$$

The amount of total water may be calculated from the observed total weight of carbon dioxide by the equation,

$$\text{wt total } H_2O = (\text{wt total } CO_2) \times \frac{\text{at. wt C}}{\text{mol. wt } CO_2} \times \frac{\text{mol. wt } H_2O}{\text{mol. wt } H_2} \times \frac{\text{wt H}}{\text{wt C}}, \qquad (17)$$

where the weight percent hydrogen and carbon in the fuel is either estimated from its physical properties [3] or determined directly by methods such as outlined in reference [4].

Air-fuel ratio by gas analysis of this kind is based on the volume fraction of carbon dioxide in the dry gas as established by the volumetric analysis. When combustion is complete, carbon dioxide concentration may be used as an indication of the air-fuel ratio, and the relation

$$(\text{vol } CO_2)_{\eta_b = 100} = \text{vol } CO_2 \times \frac{\text{wt free } CO_2 + CO_2 \text{ from combustibles}}{\text{wt free } CO_2}, \qquad (18)$$

may be used to establish the concentration for the hypothetical case of complete combustion. This equation is not strictly correct, but its accuracy is sufficient for the present purpose. Air-fuel ratio may then be calculated by the equation

$$\frac{1}{f} = \frac{240\ C}{(\text{vol \% } CO_2)_{\eta_b = 100}} + 7.15\ (1 - C), \qquad (19)$$

where C is the weight fraction of carbon in the hydrocarbon fuel. This equation may be derived from the chemical equation describing the relation among reactants and products of complete combustion of hydrocarbon fuels in air. If a gas sample representative of average conditions in the combustion chamber is desired, then the air-fuel ratio by gas analysis may be used as a criterion in judging the quality of the sample.

III. Experimental Apparatus

The combustion train used in this laboratory was patterned after that described by Wagman and Rossini [4].

A diagram of the assembled apparatus is shown in figure 1, in which *A* represents a source of com-

pressed air; *B*, control valve; *C*, 3-gal jar filled with activated alumina; *D*, mercury manometer; *E*, quartz combustion tube containing copper oxide wire; *F*, electric heater; *G*, female Pyrex connection, standard taper; *H*, graded seal, quartz to Pyrex; *I*, Pyrex absorption tube containing in order, anhydrone and ascarite; J, Pyrex absorption tube containing in order ascarite and anhydrone; *K* Pyrex absorption tube containing phosphorus pentoxide. Components of the system *B* through *K* comprise the purification section. *L* is a three-way stopcock; *M*, 16-liter stainless-steel sample container; *N*, three-way stopcock; *O*, Pyrex glass cold trap; *P*, female Pyrex connection, standard taper; *Q* and *R*, electric heaters; *S*, quartz combustion tube packed with copper oxide wire; *T*, graded seal, quartz to Pyrex and *U*, flow meter; 1, Turner absorption bottle containing in order drierite and phosphorus pentoxide, separated by asbestos; 2, Turner absorption bottle containing in order ascarite and phosphorus pentoxide, separated by asbestos; 3 and 5, Turner absorption bottles containing in order anhydrone and phosphorus pentoxide, separated by asbestos; 4 and 6, Turner absorption bottles containing in order ascarite and phosphorus pentoxide, separated by asbestos. These bottles may be closed by turning the body under the cap. Temperature is measured by Chromel-Alumel thermocouples placed along the combustion tubes. Components *O* through *U* and absorption bottles 1 to 6 comprise the analysis section. The combustion tube is made of quartz; the length is 100 cm; the internal diameter 20 mm; and the wall thickness 5 mm. Only the last 55 cm are heated in the furnace. The Turner absorption bottles that contain the reagents were modified by attaching 12/5 male spherical joints to the caps. The cold trap was made of Pyrex glass, the inner tube of which was wrapped with glass wool, and a side arm was used to insert a copper-constantan thermocouple to measure the temperature of the gas. The freezing mixture, which gives a temperature of −78° C, was prepared by adding crushed dry ice to a mixture of equal weights of carbon tetrachloride and chloroform.

The balance used has a capacity of 200 g and a sensitivity of 0.1 mg. Before weighing the absorption bottles, the lubricant was carefully washed from the ball joints with carbon tetrachloride, and then the whole surface was washed with ethyl alcohol. The bottles were allowed to rest in the balance case for 20 min before weighing. A closed absorption bottle containing ascarite was used as a counterpoise.

The gas sampling tube consisted of an outer nominal ½-in. standard iron pipe with an inner ⅛-in. thin-walled copper tube. This sampling tube, or probe, was cooled by passing water through the space between the tube and pipe.

The stainless steel container had an internal volume of 1,000 in.^{3} and was fitted with a needle valve at each end and with a compound vacuum-pressure gage. Gas was drawn through the inner tube of the water-cooled probe and pumped into an evacuated tank by a diaphragm pump to a pressure

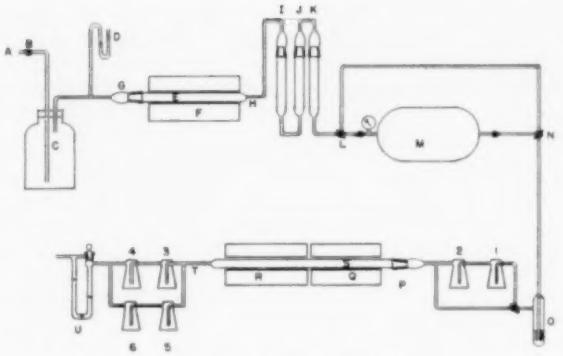

FIGURE 1. *Combustion train.*

of about 30 lb/in.^{2} gage. In some cases samples were collected at combustion-chamber pressure (usually near atmospheric) by connecting the evacuated container directly to the probe and opening the valve.

The volume fraction of carbon dioxide in the sample was found by analyzing a portion in an improved Orsat apparatus as described by Shepherd [5]. Colorimetric tubes described by Shepherd [6] were used to determine the carbon monoxide content. These tubes contain palladium sulfate and ammonium molybdate on silica gel. Passage of gas over this material produces a change of color, and a comparison with color standards indicates the concentration of carbon monoxide in the gas. The colorimetric tubes used in this investigation were designed and calibrated for passage of 90 ml of gas at the rate of 1¼ ml/sec, and the change of color indicated concentration of carbon monoxide from 0.0025 to 0.020 percent by volume. Usually it was necessary to dilute a portion of the exhaust gas with air and pass 90 ml of the mixture through the tubes. The concentration of carbon monoxide in the exhaust gas was then calculated from the observed concentration in the mixture.

IV. Analytical Procedure and Results

Air was passed through the system until the furnaces reached the operating temperature of 1,000° C, the absorption bottles were put in place, and then the exhaust gas was passed through the analyzing section of the system. When the gas sample in the container was at atmospheric pressure, it was displaced into the analysis section by air from the purification section. For samples at higher pressure, the gas was discharged into the analysis section, and the rate was controlled by adjustment of the needle valve on the sample container. The sample rate in most experiments was 400 ml/min. After the sample was passed through the cold trap and bottles 1 to 4, inclusive, the condensate in the trap was volatilized by gentle heating and flushed directly into the furnace and thence to bottles 5 and 6 by air from the purification section. All bottles were removed, and the combustion tubes were then

allowed to cool while the flow of air was continued.

While this part of the analysis was in progress, a small sample of the exhaust gas was analyzed for its carbon dioxide and carbon monoxide content. These data, in conjunction with the observed increase of weight of absorption bottles 2, 3, 4, and 6 were used to calculate combustion efficiency. Change of weight of bottle 5 was not measured since water vapor condensed in the trap and susequently was absorbed in bottle 5. Hence it was necessary to estimate the quantity of water from combustion of condensed hydrocarbons, and this was done on the assumption that the condensed material was original fuel. Equation 17 was used with the change of weight of bottle 6 to calculate the water of combustion in bottle 5.

Experimental results from a series of tests in which 80 octane unleaded gasoline was burned are presented in table 1, in which the observed changes of weight of the various absorption bottles are listed under the numbers that identify the bottles in figure 1. Change of weight of absorption bottle 6 was corrected by subtracting 8 mg, as it was found that this amount of carbon dioxide was held up in the trap, some as gas and some occluded or dissolved in the condensate. This correction was established by flowing exhaust gas samples of the same size and composition (32 liters containing about 3 vol % carbon dioxide) through a cold trap at −78° C and then warming and flushing the condensate into two absorption bottles by a stream of air free from carbon dioxide, water, and combustibles. The increase of weight of the ascarite bottle varied in four tests from 9.2 to 10.4 mg and averaged 10 mg. It was estimated that approximately 6 mg of this observed change was due to gaseous carbon dioxide remaining in the trap, and 2 mg due to adsorbed hydrocarbons. Subtracting these estimated corrections from the observed change of weight of 10 mg left 2 mg of carbon dioxide dissolved or occuluded in the trap. The tests were made without flushing the cold trap with air before volatilizing the condensate, and the correction to bottle 6 in these tests was considered to be 8 mg.

TABLE 1. *Analyses of exhaust gas*

Run	Observed change of weight of bottle number—					CO_2	CO	Combustion loss					η_b
	2	3	4	[a]6	[a]4+6			CO as CO_2	C_nH_x and H_2 determined as—		C_nH_x in trap determined as—		
									CO_2	H_2O	CO_2	[b] H_2O	
	g	g	g	g	g	%	%	%	%	%	%	%	%
1	1.6642	0.0266	0.1000	0.0658	0.226	2.87	0.16	2.12	2.14	1.28	2.11	1.36	91.0
2	1.5161	.0180	.1150	.0393	.154	2.88	.15	2.07	1.29	0.98	1.42	0.92	93.2
3	1.4163	.0169	.1286	.0339	.163	3.02	.20	2.60	1.31	.97	1.30	.84	93.0
4	1.5161	.0197	.1449	.0371	.182	3.28	.16	1.90	2.51	1.05	1.32	.86	92.3
5	1.4178	.0217	.1395	.0573	.197	3.10	.18	2.23	2.12	1.22	2.15	1.39	90.9
6	1.4827	.0244	.1463	.0536	.200	3.10	.17	2.09	2.35	1.32	1.93	1.25	91.1
7	1.4600	.0226	.1463	.0633	.210	3.01	.18	2.29	2.12	1.23	2.29	1.49	90.6
8	1.7377	.0263	.1688	.0437	.212	3.18	.16	1.96	2.51	1.23	1.36	0.88	92.1
9	1.2196	.0083	.0107	.0089	.020	3.77	.02	0.23	0.21	0.02	0.43	.28	98.8
10	1.3144	.0162	.1189	.0516	.171	2.57	.15	2.32	1.62	1.03	2.10	1.36	91.6

[a] Corrected for 8 mg of CO_2 retained in cold trap.
[b] Calculated from the amount of CO_2 from C_nH_x in trap, assuming that the composition of the condensate was the same as the fuel, 85% of C and 15% of H by weight.

An independent check on the amount of carbon dioxide occluded in the trap was obtained by a volumetric method. As before, about 32 liters of exhaust gas, containing 2 percent of carbon dioxide by volume in this case, was passed through a trap at −78° C, and the trap was purged at low temperature with air free from carbon dioxide. It was then connected to an evacuated container (with a small trap at 0° C between) and warmed to about +80° C. The small trap at 0° C was used to collect water and some combustibles. It was realized that some carbon dioxide would possibly be held up in the small trap, but probably in insignificant amount. The gas collected in the evacuated container was analyzed by treating with alkali in an Orsat apparatus, and the contraction in volume was considered to be the volume of carbon dioxide from the cold trap. Five tests of this type were made, giving an average volume of 0.9 ml and an average weight of 1.6 mg of carbon dioxide. The weight of carbon dioxide was estimated from the observed volume. The average amount occluded from about 32 liters of gas containing 2 percent by volume of carbon dioxide was thus 1.6 mg. These results are in good agreement with the gravimetric determination of 2 mg, when the difference of carbon dioxide concentration in the samples is considered. If 2 mg is considered applicable to the data of table 1, neglect of this factor would have decreased the indicated η_b by about 0.1 percent. This correction, however, may be dependent on the carbon-dioxide content of the exhaust gas, the apparatus used, rate of flow, etc., and probably must be determined for the special conditions under which the analysis is made.

Loss of combustion efficiency was calculated from the experimental data for the various types of combustible material, and the results are presented in table 1. These data indicate for these samples a combustion loss due to carbon monoxide of about 2 percent, that from hydrocarbons and hydrogen that passed through the trap about 3 percent, and that from combustibles of higher molecular weight retained in the trap also about 3 percent.

V. Accuracy of the Method

Three samples of known composition were prepared and were diluted with air until the resulting mixtures contained components in concentrations that are considered typical of exhaust gases from combustion chambers. If it is assumed that these mixtures of known composition resulted from burning a fuel (gasoline) containing 85 percent of C and 15 percent of H by weight, then the combustion efficiencies would have been 94.7, 98.5, and 87.6 percent. The degree to which these values could be duplicated by the results of the analyses would constitute a check on the method.

The dependency of the values of combustion efficiency, which it is desired to check, upon the ratio of carbon to hydrogen in the fuel is slight. If the fuel that had been burned to give the first sample had been propane, which consists of 81.7 percent of C and 18.3 percent of H, then the efficiency would have been 95.1 percent instead of the figure 94.7 percent for gasoline.

Data on the samples of known composition, and on the analyses of these samples, are given in table 2. The cold trap was not used in these tests. The agreement of the values of combustion efficiency calculated from the analytical results, with those calculated on the basis of the known composition, indicates that the method is capable of yielding reliable values of efficiency.

TABLE 2. *Analyses of prepared samples*

Sample composition			
Sample number	1	2	3
Mole percent of CH_4	2.35±0.05		
Mole percent of CO	2.60±0.05	0.46±0.025	4.15
Mole percent of H_2	2.58±0.05	.58±0.025	4.20
Mole percent of C_2H_4		.51±0.025	4.20
Mole percent of CO_2	92.47	98.45	87.45
Calculated comb. eff.[a]	94.7±0.1	98.5±0.1	87.6

	Analytical results										
Run number	1	2	3	4	5	6	7	8	9	10	11
Sample number	1	1	1	1	2	2	3	3	3	3	3
Sample rate, ml/min	400	400	400	400	400	400	150	250	600	800	800
Vol. CO_2, after dilution, %			2.7	2.3		2.4	2.6	2.3	2.5	2.9	2.5
1/f	30	110	74	87	84	86	70	80	73	65	73
Vol. CO (exptl.), %			0.060	0.059		0.013	0.04	0.04	0.04	0.05	.04
Vol. CO (known), %[b]			.076	.064		.011	.13	.11	.12	.14	.12
CO_2 bottle 2, g	2.0491	0.4785	.5304	.4647	0.4970	.3631	.2788	.2843	.3939	.4588	.3782
CO_2 bottle 4, g	0.1082	.0242	.0288	.0239	.0065	.0058	.0416	.0380	.0572	.0625	.0548
H_2O bottle 3, g	.0643	.0127	.0174	.0152	.0036	.0037	.0181	.0211	.0237	.0289	.0278
Comb. eff. from analytical data[c]	94.7	95.2	94.6	94.6	98.6	98.3	87.7	87.6	88.2	88.4	87.2
Comb. eff., calc.[a]	94.6 ±0.1	94.6 ±0.1	94.6 ±0.1	94.6 ±0.1	98.6 ±0.1	98.6 ±0.1	88.4	88.4	88.4	88.4	88.4

[a] η_b calculated, using eq 11. Fuel assumed to have been 85% of C, 15% of H, and $\Delta Hc/\Sigma\Delta Hf=0.965$.
[b] In runs 7 to 11, the known value of CO was used in the calculation of η_b.
[c] η_b calculated, using eq 15.

Tests on the third sample of known composition were made to determine the effect of rate of flow on the analytical results. At the rate of 800 ml/min, the computed combustion efficiency was less consistent, and it was deemed advisable to stay below this rate for better precision. It was decided to establish a rate of 400 ml/min as a standard, since tests at this rate on the first two known samples were satisfactory. Determination of carbon monoxide was inaccurate in the tests of the third sample, probably because of the relatively high concentration of unsaturated material in the gas. Shepherd states [6] that unsaturated organic compounds interfere in the determination of carbon monoxide by this method. Combustion efficiency was computed using the known concentration in order to better determine the accuracy of the gravimetric part of the analysis.

Accuracy of the results of the tests of the prepared samples also may be determined by a comparison of the experimental with the known values of the ratio of the weight of carbon dioxide from combustibles to the free carbon dioxide in the sample. A comparison can also be made of values of the ratio of water from combustibles to free carbon dioxide. Combustion efficiency is determined by the values of these ratios, and an accurate determination is desirable.

Average values of these ratios are plotted in figure 2, and it may be seen that the value of the carbon dioxide ratio determined by analysis in the combustion train is very close to that calculated on the basis of the known composition. Values of the ratio of water from the combustible material to the weight of carbon dioxide in the third sample is somewhat higher than the known value, but agreement is good for the first and second samples.

Another check on the accuracy of the analytical method was by a comparison of combustion efficiency by gas analysis with that established by heat balance across several combustion chambers. Analyses were made using the original method in which the cold trap was not used, and it was on the basis of these tests that the procedure was revised.

Seventeen analyses were made on exhaust gas from combustion of gasoline, and seven were made on gas from combustion of kerosine, or fuel similar to kerosine. When gasoline was used, combustion

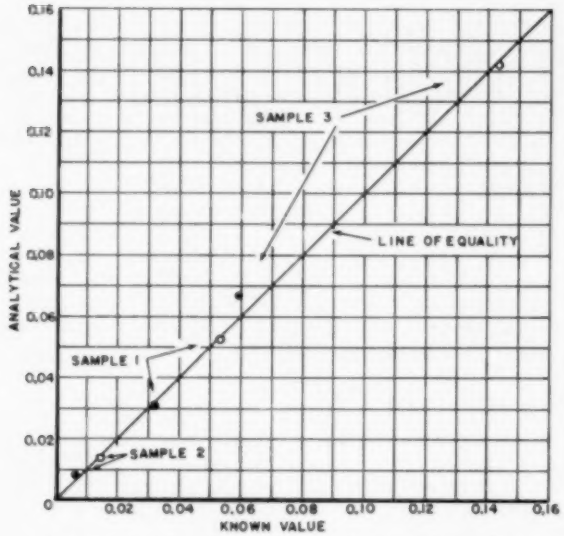

FIGURE 2. *Results of analyses of prepared samples.*

○, $\frac{\text{wt } CO_2\text{, bottle 4}}{\text{wt } CO_2\text{, bottle 2}}$ ●, $\frac{\text{wt } H_2O\text{, bottle 3}}{\text{wt } H_2O\text{, bottle 2}}$

efficiency indicated by gas analysis was on the average 2 percent higher, and after correcting the heat balance observations for such factors as loss of heat from the system and thermocouple, incomplete recovery of dynamic temperature, and the small water content of the air, the difference was reduced to 1 percent. When kerosine was burned, the difference was considerably greater and in the same direction. In this case it was considered that the major part of the difference was caused by loss of combustible material from these samples by condensation in the sampling probe, vessel, and connecting tubes. This explanation did not seem to apply to the samples from combustion of gasoline. In this case it was found that combustibles of higher molecular weight were adsorbed in bottles 1 and 2. It was for this reason that the procedure was revised to include the use of the cold trap. By this means these combustibles could be separated from the gas before passage through the adsorption bottles and later passed directly into the furnace.

A series of tests was made in which identical samples were analyzed with and without the cold trap in the train, and η_b was on the average about 1 percent lower when the trap was used. Since the previous comparison of η_b by heat balance and by gas analysis had indicated that gas analysis was high by about 1 percent, results of these tests indicated that agreement would be excellent with the improved method of analysis.

A comparison of the data from the two methods of analysis indicated that approximately 45 percent of the combustibles of higher molecular weight were adsorbed in bottles 1 and 2 when the trap was not used. It was found that recovery was possible by flushing the absorption reagents with air, but it appeared that recovery was only 55 percent complete after 3 hr of flushing. The correction of 2 mg for adsorbed hydrocarbons that was mentioned in the preceding section in connection with the amount of carbon dioxide occluded in the trap was also estimated from these data.

It is known that formaldehyde is present in exhaust gas under some conditions of combustion. However, only a trace of formaldehyde was found in one of a number of samples taken from various combustion chambers operating on different fuels. If the cold trap is used in the combustion train, presence of formaldehyde will not introduce a large error, as it will condense in the trap and be burned with other condensed compounds. A small error will result, since the heat of formation of formaldehyde is neglected when η_b is calculated. If the cold trap is not used, experiment has shown that formaldehyde is completely absorbed by the ascarite in absorption bottle 2, and a separate analysis would be necessary.

Blank runs. Fourteen blank runs were made to determine the experimental error to be expected in these analyses. Air, freed from carbon dioxide, water, and combustibles in the purification section of the train, was passed for a period of 3 hr at the rate of 400 ml/min through the train. The cold trap was not used. Results from these runs showed that the average error was of the order of 1.5 mg. Some determinations also were made of the reproducibility of weighing. A clean absorption bottle packed with reagents was first weighed, and then handled as usual, including greasing, followed by the cleaning operation. Air was not passed through the bottle. Change of weight was no more than 0.2 mg in the weighing experiments. It is probable that passage of the large quantity of air through the bottles was responsible for the larger experimental error determined above.

VI. Conclusion

A gravimetric method of analysis was developed and found applicable to exhaust gas from gas-turbine combustion chambers. Combustion efficiency determined by this method agreed with that calculated from the composition of prepared samples to about ½ percent; combustion efficiency obtained by the analysis of actual gas samples agreed with that calculated by heat balance to better than ½ percent. It is concluded that the gravimetric method may be used to provide accurate information about the magnitude of the loss of heat due to incomplete combustion, and partial information about the nature of the components of the exhaust gas.

VII. References

[1] Louis Jordan and J. R. Eckman, The determination of oxygen and hydrogen in metals by fusion in vacuum, BS Sci. Pap. **18**, 445 (1925) S514.

[2] A. L. London, Gas-turbine plant combustion-chamber efficiency, Trans. ASME **70**, 317 (1948).

[3] Thermal properties of petroleum products, NBS Misc. Pub. M97 (1929).
[4] D. D. Wagman and F. D. Rossini, A note on the macro-analysis of carbon and hydrogen by combustion, J. Research NBS **32**, 95 (1944) RP1577.
[5] Martin Shepherd, An improved apparatus and method for the analysis of gas mixtures by combustion and absorption, BS J. Research **6**, 121 (1931) RP266.
[6] Martin Shepherd, Rapid determination of small amounts of carbon monoxide, Anal. Chem. **19**, 77 (1947).

WASHINGTON, February 13, 1950.

Journal of Research of the National Bureau of Standards Vol. 45, No. 2, August 1950 Research Paper 2118

Absorption of Near-Infrared Energy by Certain Glasses[1]

By Jack M. Florence, Charles C. Allshouse, Francis W. Glaze, and Clarence H. Hahner

An analysis has been made of the absorption bands of various glasses by calculation of the internal transmittances and surface losses. The wavelengths, in microns, associated with broad absorption bands have been measured, and the active vibrating groups causing the absorption are as follows: 2.7, CO_2; 2.75, OH; 2.75, CO_2; 2.9, OH associated; 3.5, CO_3^{--}; 3.65, (NO_3^-); 3.8, Si—O bond; 4.0, CO_3^{--}; 4.15, (NO_3^-); 4.25, CO_2; 4.45, Si–O bond; and 4.7, OH associated. The greatest loss of infrared energy for a number of glasses is caused by surface losses, rather than by true internal absorption.

I. Introduction

1. Gaseous Components of Glasses

Glasses contain, in solution and as bubbles, small amounts of gaseous components. These are residues of the decomposition products of the original batch materials or the result of contact with the furnace atmosphere. The gaseous components in the body of the glass may be considered as present in two conditions: namely, in true solution and as a part of the internal structure. The internal transmittances for any glass, when plotted against wavelength, will contain absorption bands in the region of the spectrum in which these gases absorb. The intensity of the absorption bands depends upon the concentration and the absorbing power of the gas.

Because the surfaces of many glasses are chemically active toward the atmosphere, they also become of importance in the transmission of near-infrared energy. Weyl [1][2] explains that the configuration of the ions in the surface layer of a glass is not identical with that in the internal structure. He has explained the presence of OH^- in a glass as being a surface phenomenon. The surface of silica glass has a film of OH^- formed from the hydrolysis of Si-O-X bonds, where X is either an alkali or an alkaline earth ion. The X forms a water soluble salt that is leached out and replaced by a hydroxonium ion (H_3O^+). The surface contains those Si-O-Si bonds that were originally present in the glass and a number of the Si-OH groups.

The above explanation may be carried further by X forming first a hydroxide and then a carbonate. Taking a lithium silicate glass as an example, it follows:

$$\text{-Si-O-Li} + 2\text{HOH} \longrightarrow \text{SiO-OH}_3 + \text{LiOH}$$

$$\text{-SiO-OH}_3 \longrightarrow \text{SiOH} + \text{HOH}$$

$$2\text{LiOH} + \text{CO}_2 \longrightarrow \text{Li}_2\text{CO}_3 + \text{HOH}$$

The products of the reaction, plus any sorbed water from the atmosphere, remain on or near the surface of the glass.

Roman, Marboe, and Weyl also found that glass surfaces containing Ba^{++} and Pb^{++} ions, among others, showed decreasing hygroscopicity with decreasing ionic potential [2]. It has been found that glasses containing BaO and PbO have a high transmissivity for infrared energy for wavelengths of 2.5 to 4.5 μ [3, 4].

2. Characteristic Wavelengths of the Vibrating Groups

The identification of the vibrating groups has been made from the knowledge of the gaseous components that may be expected to be in a glass and their characteristic wavelengths. It has been possible to identify the vibrating groups to be expected in a glass through a knowledge of the decomposition products of the batch materials used and their characteristic absorption bands. The precise location of the wavelengths at which these absorption bands occur has been amply discussed by Herzberg [5].

The wavelength of the fundamental vibration of OH in water vapor has been identified at 2.66 μ. The hydroxyl vibration becomes broader and stronger and moves to a longer wavelength when "hydrogen bonding" occurs [5]. The substitution of a silicon atom for one of the hydrogen atoms of the HOH dipole also creates a difference in the internuclear distance of the OH bond, thereby changing the observed wavelength for this vibration. The wavelength for the OH vibration in the vapor phase, obtained from glasses, is 2.75 μ. When the water is

[1] This project was supported by the Department of the Navy, Bureau of Ships.
[2] Figures in brackets indicate the literature references at the end of this paper.

in the liquid state, the characteristic vibrations occur at wavelengths of 2.9, 4.7, and 6.25 μ [6]. Dorsey gives the wavelengths from several sources as 2.663 μ for the vapor phase, and 2.97 μ for the liquid phase for pure water [7].

Any caronate ion (CO_3^{--}) that may be absorbed on a glass surface will have characteristic absorption bands. It has strong absorption bands at about 3.5 and 4.0 μ, which is in the region of absorption by the first harmonic of the intense fundamental vibration at 6.8 μ, that shift with the increase or decrease in equivalent weight of the metallic cation. The composite transmission curve for salts containing this ion (fig. 1) was prepared from the data of Coblentz [8] and of Schaefer, Bormuth, and Matossi [9]. Carbon dioxide gas (CO_2) has absorption bands at 2.7, 2.75, and 4.25 μ and may be identified by the 4.25-absorption band [5].

The transmittance curves for salts containing the nitrate ion (NO_3^-) (fig. 2) show absorption bands at approximately the same wavelength as those for the carbonate ions [8, 10]. The fundamental vibration of shortest wavelength for the nitrate ion occurs at 7.25 μ, the band occurring at 3.65 μ being the first harmonic of this vibration.

3. Absorption of Glasses

A recent publication has identified the absorption of near-infrared energy at wavelengths of 2.7 to 3.0 μ as the OH^- vibrational absorption introduced by the water content of the glass [11]. Glasses do not show fine line structure of absorption in the infrared, but rather wide regions of absorption and transparency. This has led to the general conclusion that the absorption of energy at wavelengths of 3.0 to 4.0 μ is influenced by the water-absorption band. Further identification of this absorption region is attempted in this paper. Also, a method is presented for the determination of the behavior of certain glasses in the near-infrared region and, from such data, the specific absorption bands may be more easily identified.

II. Preparation and Measurement of the Glasses

The glasses, with the exception of the fused silica and Pyrex glass No. 774 samples, were prepared for this work and were melted in platinum crucibles of 300- to 500-g capacity. The batch materials, in most cases, were those used in the production of precision optical glass; hence they were of high commercial purity. No attempt was made to further purify these materials prior to use. The only metallic oxide believed to be present in sufficient quantities to affect the transmission was iron. The amount of iron present, as Fe_2O_3, in the glass is estimated to be less than 0.02 percent. Its presence is shown by an absorption band at or near 1.0 μ (fig. 13).

The glasses were melted and fined in either a platinum resistance or a Globar furnace in about 6 hr and then poured into steel molds to form samples approximately ½ in. thick. The quality of the samples generally equaled that of the requirements for optical glass. Samples were prepared for measurement by grinding and polishing into plates, with plane parallel faces, 2 in. square.

The spectral transmittances from 2 μ and beyond were determined by a Baird automatic infrared spectrometer. Where values below 2 μ are reported, these data were determined radiometrically by means of a fluorite prism mirror spectrometer, Nernst glower, and a vacuum thermopile. All of the infrared transmission data was supplied by the Radiometry Section of the Bureau.

The compositions of the glasses discussed in this paper are given in table 1.

TABLE 1.—*Glass Composition*

(weight percent)

Glass type	SiO_2	B_2O_3	Li_2O	Na_2O	K_2O	BeO	BaO	PbO	Al_2O_3	Cr_2O_3	MnO_2
Fused silica	100.00										
Lithium silicate	80.72		19.26								
Lithium-beryllium silicate	84.53		8.42			7.05					
Sodium-barium silicate	40.00			20.00			40.00				
Potassium silicate	70.00				31.00						
Pyrex No. 774 [14]	80.5	12.9		3.8	0.4				2.2		
NBS-IR-1	48.16			9.94				35.80		5.63	0.47

III. Calculation of Internal Transmittances

Because the absorption of near-infrared energy by glasses may, in part, be a surface phenomenon, it becomes highly desirable to determine the internal transmittance of the glass itself. A method used for the determination of the transmittance of visible light for optical glass, and also used by Rubens for the infrared spectra, is to measure the total transmittance [3] for two thicknesses of a given glass sample [12].

The total transmittance of a sample of glass is defined as

$$T = (1-S)^2 T_i,^4 \quad (1)$$

[3] Total transmittance, as used in this paper, means the percentage of incident energy emerging perpendicular to the surface of the sample and parallel to the direction of propagation of the energy.

[4] George W. Morey, The properties of glass, p. 367. (Reinhold Publishing Corp., New York, N. Y., 1938). This can be proved as follows: The energy entering the glass is $(1-S)$. If $(1-T_i)$ is the internal absorptance of the glass sample, the energy reaching the second surface is $(1-S)-(1-S)(1-T_i)$. Then, the energy leaving the glass is $(1-S)-(1-S)(1-T_i)-[(1-S)-(1-S)(1-T_i)]S$, which is equal to T. So

$$T=(1-S)(1-1+T_i)-(1-S)(1-1+T_i)S$$
$$=(1-S)T_i(1-S)$$
$$=(1-S)^2 T_i$$

It must be remembered that the above derivation does not take into account multiple reflection, which may produce an appreciable error.

where T is the total transmittance, T_i the internal transmittance, S the fractional surface loss at, and $(1-S)$ the fraction transmitted through, one surface of the sample. Then, for two thicknesses of the same glass

$$\frac{T_1}{T_2}=\frac{(1-S)^2T_{i_1}}{(1-S)^2T_{i_2}}=\frac{T_{i_1}}{T_{i_2}},$$

and

$$\log T_1-\log T_2=\log T_{i_1}-\log T_{i_2}, \qquad (2)$$

where the subscripts 1 and 2 indicate the thin and thick samples, respectively. According to Lambert's law,

$$-\log T_i=a_ib, \qquad (3)$$

where a_i [5] is the internal absorbance index, and b is the thickness in millimeters. Therefore, $\log T_1-\log T_2=-a_ib_1+a_ib_2=a_i(b_2-b_1)$, and solving for a_i,

$$a_i=\frac{\log T_1-\log T_2}{b_2-b_1}. \qquad (4)$$

The internal transmittance, T_{i_3}, can then be calculated from the absorbance index for any given thickness, b_3, by means of the following:

$$T_{i_3}=\text{antilog}\,(-a_ib_3). \qquad (5)$$

The loss of energy at one surface of the sample by reflection, scattering and absorption of the film is obtained from the equation

$$S=1-\left(\frac{T}{T_i}\right)^{1/2}.$$

The above equation is based on the assumption that the surface losses for samples of the same glass, but of different thicknesses, are the same. Calculations of absorbance indices from several thicknesses of the same melt of glass (NBS-IR-1) vary, but the curves drawn from these data tend to show the same maxima.

The above method of calculating the internal absorbance index of a glass is not too accurate when the total absorbance ($-\log T_i$) is small or is changing rapidly. In part, this is due to the degree of accuracy of the infrared spectrometer, which is of the order of ± 1 percent; also, instrument lag in the automatic instruments, shifts caused by temperature variations within the spectrometer, etc., enter into the picture.

The results obtained by the preceding method are not reproducible when applied to glasses of high hygroscopicity, such as those of some of the binary systems, because of the changes in water sorbed during preparation and measurement of the samples. These data should only be used qualitatively to show absorption bands and regions of high surface loss when comparing two different glasses. Recent evidence indicates that more consistent results are obtained with fused silica and complex glasses of low hygroscopicity.[6]

IV. Absorption for Wavelengths from 2.7 to 3.0 Microns

The fused silica sample reported in a previous paper [3] had an absorption band at 2.74 to 2.80μ (fig. 3), which could be either OH or CO_2. Subsequent measurements on two fused silica samples of different thicknesses (fig. 4) have shown this band as occurring at 2.75 μ. The binary glass of lithium silicate (fig. 5) has an absorption band at 2.9 μ, indicating that the water contained by this glass is predominantly in the liquid phase.

The absorption band of the water, in the liquid phase, in a glass is so strong that it usually overlaps the absorption band for water in the vapor phase. However, in an experimental glass of the composition $Li_2O{\cdot}BeO{\cdot}5SiO_2$ (fig. 6), the two bands at 2.75 and 2.9 μ appear almost equal in intensity for the particular sample measured. The absence of the 4.25 band (CO_2) eliminates the possibility that the 2.75 band might also be caused by CO_2. It is suggested that the 2.75-μ band represents water in the vapor phase. However, this should not be considered as a proof of its existence, as it is possible that certain constituents of this glass might have weak bands in this region.

V. Absorption for Wavelengths Longer Than 3.0 Microns

The carbonate ion has two strong absorption bands (at 3.5 and 4.0 μ) that shift with the increase or decrease in equivalent weight of the metallic cation. In figure 5 the lithium silicate glass has absorption bands at 3.5 and 4.0 μ, corresponding to those of the carbonate ion. However, the mere presence of absorption bands at 3.5 and 4.0 μ is not positive identification of the carbonate ion, since the nitrate ion absorption bands occur at approximately the same wavelengths. The batch ingredients must be known before these absorption bands can be positively associated with the carbonate ion alone. An example of the 4.25 band for carbon dioxide is shown in figure 7 for a glass of the sodium-barium silicate system made from a batch containing both sodium carbonate and barium carbonate. This band has also been observed on a number of other glasses made from batch materials containing carbonates.

The substitution of nitrates for carbonates in the glass batch improves the transmission of infrared energy of the resulting glass. This is very evident from a comparison of figure 8, A and B. The glass from which the internal transmittance curves in figure 8, A were obtained was made with potassium carbonate in its batch; that from which the curves in

[5] The nomenclature used follows closely that of NBS Letter Circular LC857 (May 19, 1947).

[6] The hygroscopicity of a glass may be determined by the method of Hubbard, J. Research NBS **36**, 365 (1946) RP1706.

figure 8, B were obtained was made with potassium nitrate. The total ionic charge of the carbonate ions in the one batch was made equal to the total ionic charge of the nitrate ions in the other batch. The 3.5- and 4.0-μ absorption bands for CO_3^{--} in the first instance and the 3.65 and 4.15 bands for NO_3^- in the second are evident. These curves show rather conclusively that the CO_3^{--} is a much stronger absorbent of infrared energy than the NO_3^-. The carbonate ion also produces greater surface losses.

Fused silica has strong absorption bands at 3.8 and 4.45 μ, as indicated in figures 3 and 4. These two absorption bands are caused by the silicon-oxygen bond [11] and are of sufficient intensity to be identified in more complex glasses.

In the following tabulation the above absorption bands observed for glasses are listed by wavelengths and vibrating groups for reference:

Wavelength	Vibrating group	Wavelength	Vibrating group
Microns		*Microns*	
2.7	CO_2	3.8	Si–O bond
2.75	OH	4.0	CO_3^{--}
2.75	CO_2	4.15	NO_3^-
2.9	OH associated	4.25	CO_2
3.5	CO_3^{--}	4.45	Si–O bond
3.65	NO_3^-	4.7	OH associated

VI. Individual Glasses

1. Fused Silica

In figure 4 the two transmittance curves for two thicknesses of fused silica are shown with a curve for the calculated internal transmittance. Figure 4 also shows the calculated surface losses. The curves show the following absorption bands: 2.75, 3.0, 3.5, 3.8, 4.0, 4.45, and 4.7 μ. With the exception of the 2.75-, 3.5-, 4.0- and 4.7-μ bands, these absorption bands more or less coincide with the stronger bands of crystalline quartz [13]. The absorption bands at 3.5 and 4.0 μ might indicate the presence of a small amount of the carbonate ion. The absorption band of silica at 4.45 μ is very definite. It is important to note that apparently the OH is present in the internal structure of the glass, as indicated by the internal transmittances and the absence of an increase in surface losses in the region of 2.75 μ.

2. K_2O-SiO_2 Glass

The calculation of the internal transmittances and the surface losses for a glass from the potash-silica system shows that the greater loss of energy is at the surface of the glass. These results are plotted in figure 8, A and B. The internal transmittance curves show considerable absorption for wavelengths longer than 2.7 μ. indicating that some of the absorbing media is contained in the internal structure of the glass. The curves for the surface losses indicate the presence of carbonate ions and nitrate ions on or near the surface. The magnitude of the surface losses appears to be greater than that which could be reasonably attributed to reflection by the glass alone. This glass is, therefore, unsuitable for the transmission of infrared energy.

3. Corning Pyrex glass No. 774

The samples of untreated and vacuum-degassed Pyrex glass No. 774 used by Harrison [11] were measured at this Bureau in 1935. Applying the mathematical analysis to these data gives the transmittance curves shown in figures 9, 10, and 11. These curves indicate that the OH is present. A comparison of the internal transmittances for two samples, shown in figure 11, indicates that the vacuum treatment at the temperatures used considerably improved the internal transmittance of the glass; figure 12 shows that the treatment practically removed the surface loss caused by the OH. It seems, therefore, that the presence of the OH, is in part, a surface phenomenon, corroborating Weyl's statement [1].

4. IR Filter No. 1

Filter glass NBS–IR–1, developed for the Bureau of Ships, Department of the Navy, absorbs the visible spectrum but has a high transmittance of the near-infrared energy. The transmittance curves for this glass, figure 13, show the absorption bands in the tabulation above, including the band for CO_2 at 4.25 μ. This CO_2 absorption is indicated by the internal transmittance curve. The surface losses, shown in figure 13, indicate very little water on the surface of the glass. These data indicate that a considerable amount of the absorbing media is contained in the internal structure of this particular glass.

VII. Conclusions

A study of the transmittance of near-infrared energy by glasses of different compositions has been made from data available in the literature and experimental glasses prepared at this Bureau. The internal transmittance and surface losses of the glasses were calculated for specific wavelengths of radiant energy. It was found that, at certain wavelengths, much of the energy was reflected, scattered, and absorbed by identified groups that occurred at or near the surface of the glass. Other conditions being similar, the total transmittance of a glass for infrared energy, in the range from 2.5 to 5.0 μ, varies inversely with the hygroscopicity. This absorption of near-infrared energy may be attributed to the free water in the liquid phase, OH, CO_3^{--}, and NO_3^- ions, free CO_2, and the silicon-oxygen bond.

The authors are indebted to the Radiometry Section for supplying the data on the transmittances of these glasses, and Mason H. Black for this assistance in making some of the glasses.

VIII. References

[1] W. A. Weyl, Some practical aspects of the surface chemistry of glass, part IV, Glass Ind. **28,** 411 (1947).

[2] M. K. Roman, E. E. Marboe, and W. A. Weyl, The influence of heavy metal ions on the hygroscopicity of a glass surface, J. Soc. Glass Tech. **32,** 260 (1948).

[3] J. M. Florence, F. W. Glaze, C. H. Hahner, and R. Stair, Transmittance of near infrared energy by binary glasses, J. Am. Ceramic Soc. **30,** 328 (1948); J. Research NBS **41,** 623 (1948) RP1945.

[4] J. M. Florence, F. W. Glaze, C. H. Hahner, Transmittance of near-infrared energy by some three-component glasses, presented at American Ceramic Society meeting, April 27, 1948, Chicago, Ill. To be published in J. Am. Ceramic Soc.

[5] G. Herzberg, Infrared and Raman spectra of polyatomic molecules (D. Van Nostrand Co., Inc., New York, N. Y., 1945).

[6] J. J. Fox and A. E. Martin, Investigations of infrared spectra (2.5–7.5μ). Absorption of water, Proc. Roy. Soc. [A], **174,** 234 (1940).

[7] N. E. Dorsey, Properties of ordinary water-substance (Reinhold Publishing Corp., New York, N. Y., 1940).

[8] W. W. Coblentz, Investigations of infrared spectra (Carnegie Institution of Washington, 1906).

[9] C. Schaefer, C. Bormuth, and F. Matossi, The infrared absorption spectrum of the carbonate, Z. Physik **39,** 648 (1926).

[10] C. Schaefer and C. Bormuth, The infrared absorption of sodium nitrate, Z. Physik. **62,** 508 (1930).

[11] A. J. Harrison, Water content and infrared transmission of simple glasses, J. Am. Ceramic Soc. **30,** 363 (1947).

[12] H. Rubens, The dispersion of infrared radiation, Wied. Ann. **45,** 238 (1892).

[13] E. K. Plyler, Phys. Rev. **33,** 48 (1929).

[14] C. J. Phillips, Glass: the miracle maker (Pitman Publishing Co., New York City and Chicago, Ill., 1941).

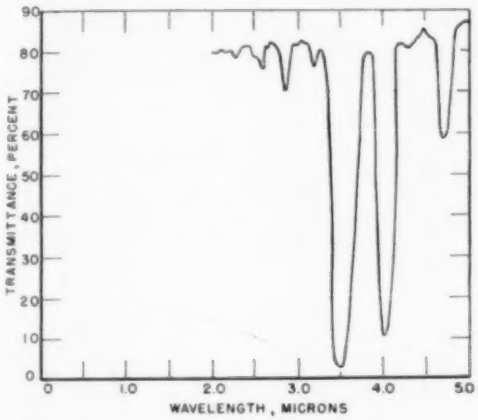

FIGURE 1. *Composite transmittance curve for metal carbonates.*

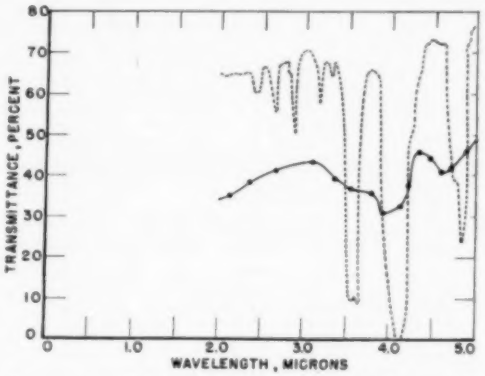

FIGURE 2. *Total transmittance of infrared energy by alkali nitrates.*

●, KNO_3 as determined by Coblentz; ○, $NaNO_3$ as determined by Schaefer, Bormuth, and Matossi.

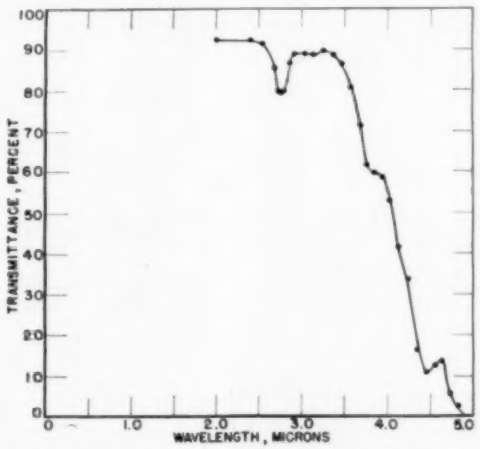

FIGURE 3. *Total transmittance of infrared energy by fused silica.*

Thickness of sample = 2.85 mm.

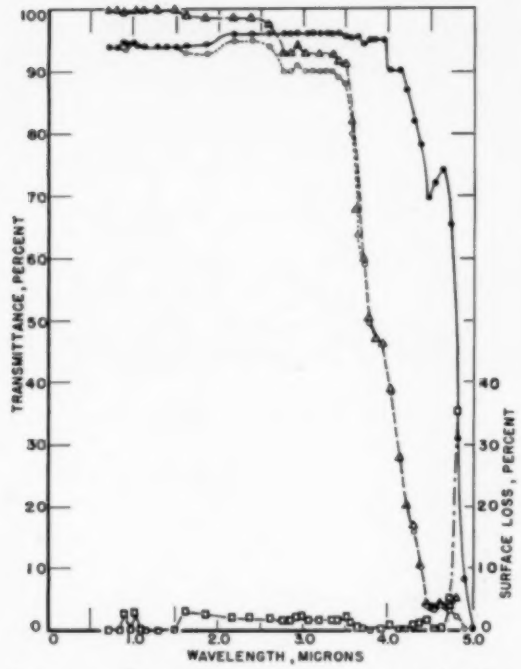

FIGURE 4. *Transmittance of infrared energy and surface losses by fused silica for two thicknesses of sample*

●, Total transmittance, thickness of sample=0.5 mm. ○, total transmittance, thickness of sample=5.0 mm; △, internal transmittance, equivalent thickness=5.0 mm; □, calculated surface losses, one surface.

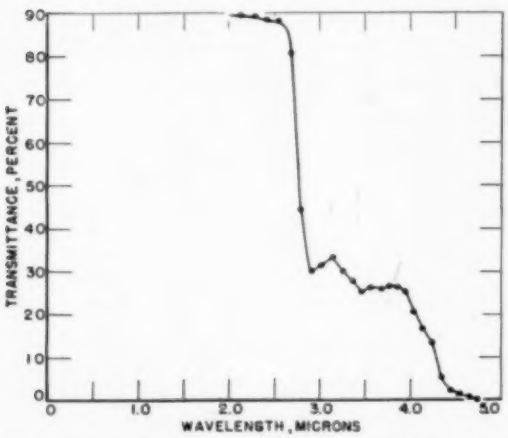

FIGURE 5. *Total transmittance of infrared energy by a lithium silicate experimental glass.*

Thickness of sample=5.74 mm.

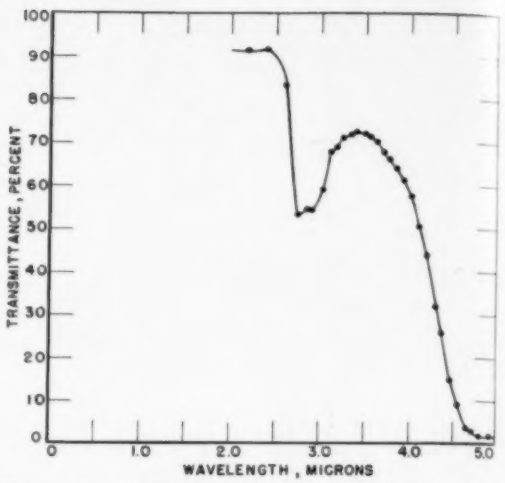

FIGURE 6. *Total transmittance of infrared energy by a lithium-beryllium silicate glass.*

Thickness of sample=2.23 mm.

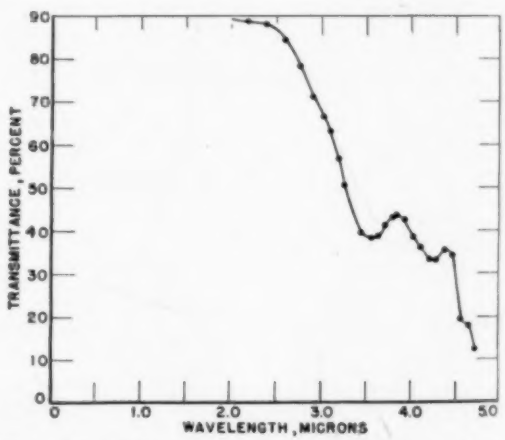

FIGURE 7. *Total transmittance of infrared energy by a sodium-barium silicate glass showing a carbon dioxide absorption band at 4.25 μ.*

Thickness of sample=2.02 mm.

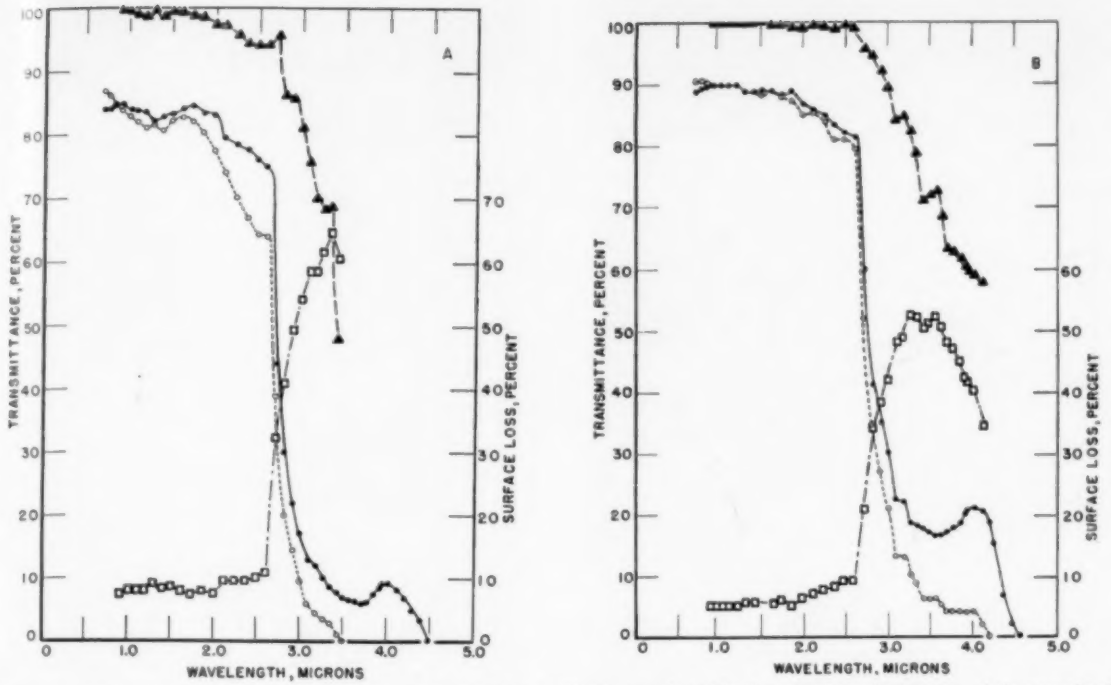

FIGURE 8. *Transmittance of infrared energy by a potassium silicate experimental glass for two thicknesses of the sample, the internal transmittance, and surface losses.*

A, Made with potassium carbonate: ●, total transmittance, thickness of sample=2.02 mm; ○, total transmittance, thickness of sample=7.57 mm; ▲, internal transmittance, thickness of sample=2.02 mm; □, calculated surface losses, one surface. B, Made with potassium nitrate; ●, total transmittance, thickness of sample=1.97 mm; ○, total transmittance, thickness of sample=8.18 mm; ▲, internal transmittance, thickness of sample=1.97 mm; □, calculated surface losses, one surface.

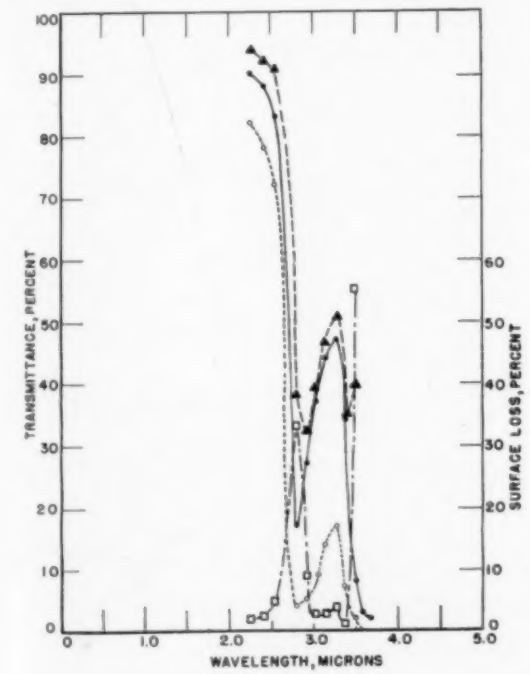

FIGURE 9. *Transmittance of infrared energy by untreated Pyrex glass No. 774.*

●, Total transmittance, thickness of sample=2 mm; ○, total transmittance, thickness of sample=5 mm; ▲, internal transmittance, equivalent thickness=2 mm; □, calculated surface losses, one surface.

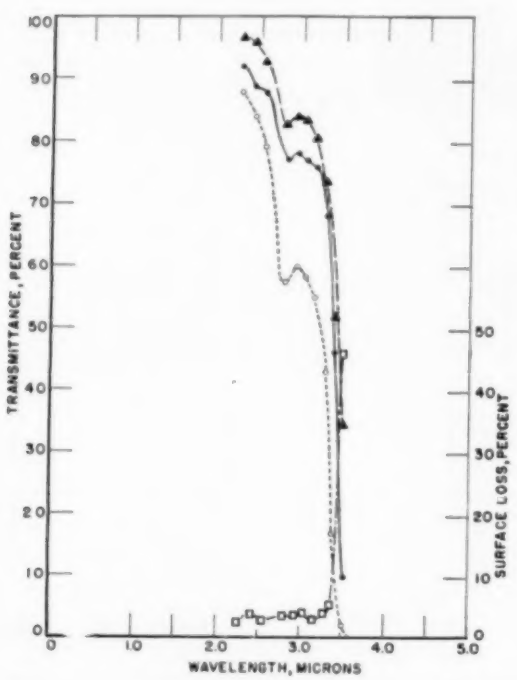

FIGURE 10. *Transmittance of infrared energy by degassed Pyrex glass No. 774.*

●, Total transmittance, thickness of sample = 2 mm; ○, total transmittance, thickness of sample = 5 mm; ▲, internal transmittance, equivalent thickness = 2 mm; ▲, calculated surface losses, one surface.

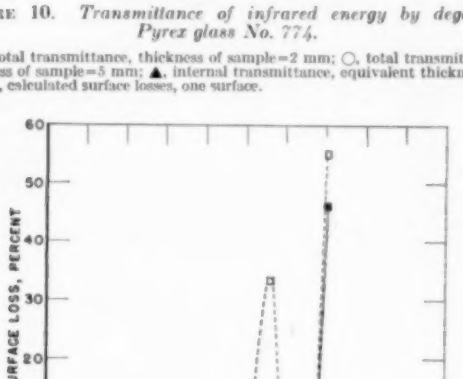

FIGURE 12. *Calculated surface losses, on one surface, of infrared energy by untreated and degassed Pyrex glass No. 774.*

□, Untreated; ■, treated.

FIGURE 13. *Transmittance of infrared energy by NBS–IR–1 filter, and surface losses.*

●, Total transmittance, thickness of sample = 1.08 mm; ○, total transmittance, thickness of sample = 4.00 mm; ▲, internal transmittance, equivalent thickness = 1.08 mm; □, calculated surface losses, one surface.

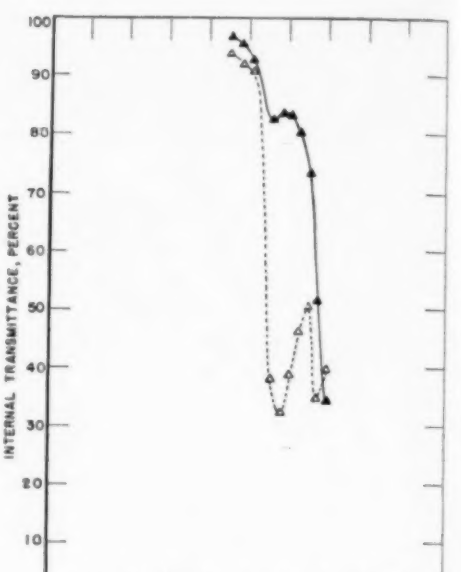

FIGURE 11. *Comparison of internal transmittances of untreated and degassed Pyrex glass No. 774.*

△, Internal transmittance untreated sample, thickness of sample = 2 mm; ▲, internal transmittance degassed sample, thickness of sample = 2 mm.

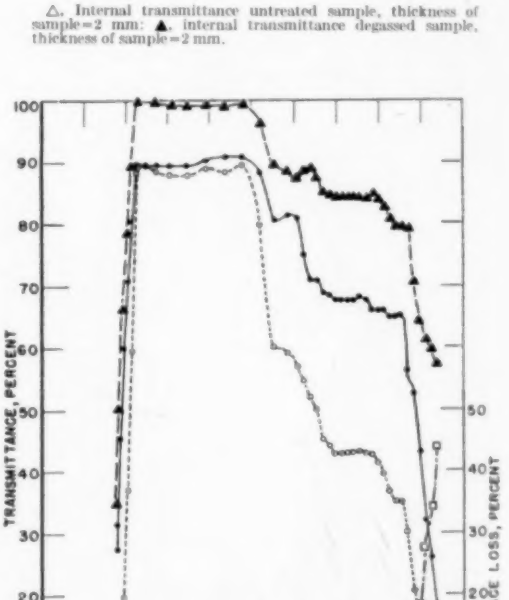

WASHINGTON, March 27, 1950.

Journal of Research of the National Bureau of Standards Vol. 45, No. 2, August 1950 Research Paper 2119

Tensile Properties of Ingot Iron at Low Temperatures

By Glenn W. Geil and Nesbit L. Carwile

True stress-strain curves obtained in tension tests at temperatures ranging from −196° to +100° C with ingot iron as annealed, normalized, quenched and tempered, hot-rolled and cold-drawn are presented. Numerous simultaneous load and diameter measurements were made during the entire course of each test. The effects of prior thermal and mechanical treatment of the iron on the true stress-strain relations are discussed.

Graphs are presented showing the influence of the testing temperature, the ferrite grain size, and the initial condition of the iron on the work-hardening characteristics, namely, strain-hardening and strain-aging. The effects of the above factors on yield stress and ultimate stress, and on true stress and true strain at maximum load and at fracture, are presented. The twinning of iron in the tests at low temperatures is briefly discussed.

I. Introduction

The ordinary tension test is a commonly used method for determining some of the important mechanical properties of materials, namely, proportional limit, yield stress, ultimate stress, breaking stress, percentage elongation, and percentage reduction of area. The procedure for this test has been standardized and is specified in detail in ASTM standards for the Tension Test, ASTM Standards 1946 (E8–46). Stress-strain curves, when drawn, are based on the original dimensions of the specimen. It is desirable, however, to have a tension test reveal more information about the material than is indicated by the above-mentioned properties. This was first pointed out by Ludwik [1][1] and discussed in some detail by MacGregor [2], who enumerated many of the advantages obtained by determining a true stress-strain curve for the material tested in tension under controlled test conditions. True stress is the load divided by the minimum area prevailing at that instant. MacGregor has shown that true strain during a tension test may be represented by $\log_e A_0/A$, in which A_0 and A represent the initial and the current minimum cross-sectional areas, respectively. If the deformation of the specimen is uniform throughout the gage length and no local contraction occurs before fracture, and assuming the volume of the specimen remains constant, the strain also may be represented by $\log_e L/L_0$, in which L_0 and L represent the initial and current gage lengths. However, as shown in a previous paper [4], local contraction may even occur during the deformation between yield and maximum load, and thus simultaneous load and diameter measurements during the entire tension test are essential for an accurate determination of the true stress-strain curve.

Many investigators [2 to 21] have determined true stress-strain curves for various steels tested in tension. Several comprehensive surveys of the literature on the mechanical properties of metals at low temperatures and the flow, fracture, ductility, and work-hardening characteristics have been published recently [22 to 28]. Several of the investigators [2, 5 to 11] have reported a linear relationship between true stress and true strain from the point representing maximum load to fracture of the specimen. Siegle [12] shows true stress-strain curves obtained with ingot iron tested in tension at temperatures ranging from −132° to 23° C. The diameter measurements were made from photographic images of the specimen taken during the test; although some difficulty was encountered in obtaining good images of the test specimen, especially at a temperature of about −130° C or lower. Siegle's reported results do not conform to a linear true stress-strain relationship from maximum load to fracture. However, only a few experimental points were determined between maximum load and fracture in the tests at subzero temperatures, and some of the irregularity in the data was ascribed to the difficulty of accurately measuring inferior photographic images. Gensamer, Saibel, Ransom and Lowrie [22] state, "It is evident that beyond that point of maximum load, the stress-strain curve in the tensile test is complicated by the introduction of radial and transverse stress components as well as by non-uniformity of the axial stress. The fact that the plot of average stress vs average strain at the minimum section is a straight line from the point of maximum load onward is purely fortuitous."

In previous investigations at this Bureau [16 to 20] in which true stress-strain curves were determined for various steels and nonferrous metals tested in tension at room temperature, the results, in general, do not conform to a linear stress-strain relation from the points representing maximum load to fracture of the specimens.

The purpose of the present investigation was to determine the influence of the testing temperature and various metallurgical factors on the true stress-strain curves and other mechanical properties of ingot iron tested in tension in the temperature range of −196° to +100° C.

II. Material and Method of Investigation

The material used in this investigation was ingot iron. The principal chemical constituents of this material other than iron, as determined by chemical analysis, are (in percent) as follows: carbon, 0.02; manganese, 0.02; phosphorus, 0.005; sulfur, 0.018;

[1] Figures in brackets indicate the literature references at the end of this paper.

silicon, 0.002; copper, 0.10; oxygen, 0.058; nitrogen, 0.002; hydrogen, 0.0005. This iron was prepared from a single heat and furnished by the manufacturer in the hot-rolled and cold-drawn conditions, with the cold-drawn rods being reduced from hot-rolled rods without intermediate annealing. The cold-drawn rods were furnished in two degrees of cold work, namely 14- and 24-percent reduction of area. The iron was studied in the conditions (1) as annealed, (2) as normalized, (3) as quenched and tempered, (4) as hot-rolled, and (5) as cold-drawn. The heat treatments that were made at the National Bureau of Standards and applied exclusively to the hot-rolled material are summarized in table 1. Typical structures of some of these materials are shown in figure 1. The number, size, and distribution of the inclusions are considered normal for ingot iron. The numerous oxide inclusions were dispersed as relatively small particles throughout the ferritic matrix, the massive elongaged inclusions composed essentially of manganese sulfide were elongated in the direction of rolling. Some precipitation occurred in the parent grain boundaries, especially in those specimens that were cooled slowly from 1,750° or 1,330° F to room temperature (fig. 1, A, B and C). Iron carbide could be identified in some grain boundaries of the specimens as annealed (fig. 1, A) and as quenched and tempered (fig. 1, B), and it also appeared to be present to a lesser degree in the specimens in each of the other conditions. It would be expected that the relative amount of carbon retained in solid solution should be a minimum in the specimens as annealed or as quenched and tempered, intermediate in the specimens as cold-drawn and a maximum in the specimens as hot-rolled or as normalized. The nitrogen content of this iron was very low (0.002% as determined by a modified Allen method), and the amount retained in solid solution should be about the same for each of the initial conditions. Although the phenomenon of strain aging has been attributed by some investigators to the presence of nitrogen, it is expected that this small amount would be ineffective in producing the marked strain-aging observed in some of the tension tests made at temperatures within the range of about +60° to +100° C.

TABLE 1. *Heat treatment of ingot iron* [a]

Designation	Diameter of rod	Temperature	Time	Remarks
	in.	*° F*	*hr*	
Annealed	0.875	1,750	1	Furnace-cooled to 800° F (20 hr) then air-cooled.
Normalized	.875	1,750	1	Air-cooled.
Quenched and tempered	[b] .500	1,700	½	Quenched in iced brine.
		1,330	1	Furnaced-cooled to 100° F (45 hr).

[a] All specimens were prepared from hot-rolled rods.
[b] Specimens machined to approximately ½ in. in diameter in reduced section and ¾ in. in diameter in shoulders prior to heat treatment.

The ferrite grain size varied considerably in each initial condition of the iron. The average ASTM grain size numbers are given in table 2, along with some of the mechanical properties of the iron at room temperature. The ferrite grain size was found to be approximately the same for the iron in the conditions as hot-rolled, quenched and tempered, and cold-drawn to 14- and 24-percent reduction in area. However, the grain size of the normalized iron was slightly larger, and the grain size of the annealed iron was considerably larger than that of the other conditions.

TABLE 2. *Mechanical properties of ingot iron at room temperature*

Condition	Hardness Rockwell B	Ferrite grain size ASTM No.	Yield stress		Ultimate stress	True breaking stress [a]	Reduction of area at maximum load	Reduction of area at initial fracture	Reduction of area at final fracture
			Upper	Lower					
			1000 psi	*1000 psi*	*1000 psi*	*1000 psi*	*%*	*%*	*%*
Annealed	24	2–3	16.7	14.7	41.2	85.0	23.7	67.0	72.1
Normalized	37	3–4	22.3	20.5	43.7	95.2	23.3	69.5	74.4
Quenched and tempered	31	4–5	24.0	20.5	39.7	88.4	23.6	71.2	76.0
Hot-rolled	32	4–5	29.6	24.7	43.3	105.0	23.2	74.9	78.4
Cold-drawn 14% reduction of area	78	4–5	[b] 60		65.0	98.0	5.6	56.0	61.4
Cold-drawn 24% reduction of area	86	4–5	[b] 72		73.2	100.9	4.3	49.1	56.1

[a] At initial fracture.
[b] No drop of beam, stress at 0.2% offset.

Cylindrical tensile specimens with a reduced section of 2-in. gage length were used. The reduced section was gradually tapered from each end; the diameter at the midsection of the gage length was about 0.003 in. less than that at the ends. A minimum gage diameter of 0.438 in. instead of the standard 0.505 in. was employed to avoid fracture in the threaded ends of the specimens during testing at low temperatures. The specimens were finished to the final dimensions by grinding and polishing in the axial direction, to avoid circumferential tool marks from acting as transverse notches. The ends of the specimen were machined with ¾-in.×10 threads and the shoulder fillets were machined to a radius of 1.5 in.

A pendulum hydraulic testing machine of 50,000-lb capacity was used for these tests. To obtain the desired test temperatures, the specimens, except for those tested at room temperature, were fully immersed in an appropriate liquid contained in a cylindrical vessel. One threaded end of the specimen passed through the bottom of the cylindrical vessel into the lower adapter of the testing machine. Lead washers were used at this position to seal

against loss of the bath liquid. The outside of the vessel was covered with several layers of wool felt for thermal insulation. The felt in turn was enclosed with a covering of thin sheet aluminum to prevent condensation of moisture on the felt. The upper and lower adapters were made as long as the clearance of the testing machine would permit. When the test temperature was −78° C or lower, the adjacent portions of the head and base of the testing machine were surrounded with pulverized solid CO_2 to minimize the temperature gradient in the adapters.

For obtaining test temperatures of +100° and +60° C, the bath, water with sodium chromate added as an inhibitor to corrosion, was heated with an electrical immersion heater. For temperatures between room (27° to 30° C) and −78° C, a bath mixture of equal parts by volume of carbon tetrachloride and chloroform was cooled by the gradual addition of small quantities of pulverized CO_2. A temperature of −78° C was maintained in the carbon tetrachloride-chloroform bath with an excess of pulverized CO_2. For temperatures of −120°, −138°, and −154° C, a bath of dichloro-difluoromethane (Freon 12) was cooled by passing liquid nitrogen through an immersed copper coil; the bath was stirred constantly with an electric stirrer. A chromel-alumel thermocouple was attached to the specimens at the upper end of the reduced gage section for measuring the test temperature. For temperatures of −188° and −196° C, the specimens were fully immersed in baths of liquid air and liquid nitrogen, respectively.

The rate of loading was less than is usual in a tension test to avoid local heating of the specimens during the plastic deformation. The loading was so controlled that the rate of contraction of the specimens beyond the initial yielding was maintained at approximately 1-percent reduction of area per minute. The maintenance of this rate of contraction of the specimen after the maximum load had been reached was achieved by a gradual closing of the control valve on the hydraulic testing machine.

A common type of reduction-of-area gage with wedge anvils was used for determining the change in the minimum diameter of the specimen during the tension tests at room temperature. However, this gage could not be used with the tests at other temperatures. A reduction-of-area gage of special design, which could function satisfactorily while largely submerged in the bath, was constructed for use at subzero and moderately elevated temperatures. A detailed description of the gage and its calibration and manipulation is given in a previous paper [4]. Changes in diameter of a specimen can be measured by this instrument with an accuracy of ±0.0001 in.

III. True Stress-Strain Curves

The true stress-strain curves obtained for specimens of ingot iron as annealed, normalized, quenched and tempered, hot-rolled and cold-drawn, tested in tension at temperatures ranging from −196° to +100° C, are given in figures 2 to 7. A scale of actual values of A_0/A is given at the top of each diagram for convenience in comparing these results with previous results obtained at this Bureau [16 to 20], in which the data were plotted on this scale. The true stress values at the initiation of fracture as obtained during test through the use of the reduction-of-area gage will be designated in this paper as the fracture stresses, whereas the points designated as crosses are the values usually reported as the true breaking stresses or fracture stresses. The latter values are obtained by dividing the load at initial fracture by the minimum area of the specimen as determined from diameter measurements made after the specimen has been fractured. Fracture of an unnotched specimen tested in tension is usually initiated at its axis, and the crack propagates toward the periphery; the metal at the periphery often extends longitudinally and contracts radially during the fracture. This "rim effect" varies with the composition, structure, and condition of the metal, as well as the temperature during the tension test. Thus, fracture stress values as determined from diameter measurements made after fracture of a ductile specimen may be of little significance.

The true stress-strain curves (figs. 2 to 7) obtained for ingot iron specimens tested at temperatures ranging from −196° to +100° C do not conform to a linear relationship for the portion of the curves between the points representing maximum load and either initial or complete fracture. This portion of the curves is absent for all specimens tested at −196° C, except for hot-rolled ingot iron, as fracture occurred before the maximum load conditions were attained. The divergence from a linear relationship usually increases slightly as the testing temperature is lowered. The divergence also varies with the initial condition of the iron and is greater for the normalized, annealed, and hot-rolled specimens than for the quenched and tempered and cold-drawn specimens.

The plastic deformation was not uniform along the gage length during the testing of the ingot iron, irrespective of the initial conditions. Some local contraction even occurred during initial yielding of the iron. At a strain value slightly above the yield, the minimum diameter of the specimen usually continued to decrease and the region of local contraction extended longitudinally along the gage length. In some specimens, however, local contraction occurred in two or more regions. As the strain approached that produced by the ultimate stress, the trend was for the specimen to become nearly cylindrical throughout its entire gage length. After the ultimate stress was attained, the specimen started to contract locally (neck) in the usual manner, and this condition continued to complete fracture. It should be pointed out, however, that the change in deformation with stress in this range, ultimate to fracture, frequently occurred in a cyclic manner as illustrated by the position of the experimental points given for the hot-rolled specimens tested at −120° and at −138° C (fig. 5).

The nonuniform deformation associated with pronounced strain-aging is manifested by the serrations in the true stress-strain curves for some of the tests at +100° C. Oscillations of the pendulum of the testing machine occurred during the deformation from yield to fracture. The magnitude of the oscillations at +100° C varied both with the degree of strain and the initial condition of the iron. For annealed, hot-rolled, and cold-drawn specimens, the oscillations were relatively small throughout the range of strain from the initial yielding to the maximum load; the magnitude generally increased slightly during the earlier portion of this range and decreased during the latter portion to very small values at the maximum load. At strains considerably greater than that at maximum load, the magnitude of the oscillations suddenly increased greatly and continued in this manner as the specimens were extended to fracture. The oscillations for the quenched and tempered specimen were relatively small and were observed only in the first half of the strain range from initial yielding to maximum load. For the normalized specimen, the oscillations were relatively small immediately following initial yielding, but increased continuously as the specimen was extended to fracture. Only variations in the true stress-strain curves corresponding to the larger oscillations are shown in figures 2 to 7. Smaller and less uniform oscillations also were observed in some of the tests at 60° C.

The change in diameter of the specimen during each oscillation could be followed with the reduction-of-area gage. The diameter decreased rapidly during each drop of the pendulum. It remained almost constant during the subsequent rise of the pendulum until the load reached a critical value and a new oscillation was initiated. The strain-aging and strain-hardening of the metal resulting from the rapid deformation that accompanied the drop of the pendulum apparently was of sufficient magnitude to prevent further deformation until the true stress was again increased to a new critical value by an increase of the applied load.

The locus of fracture curves, L, (figs. 2 to 7) are drawn through the points representing initial fracture at the various temperatures and depict the influence of the testing temperature on the fracture stress and strain at fracture of the ingot iron in each of the initial conditions. The influence of the testing temperature on the strain at fracture varies with the initial condition, and this may result in a large change in the shape of these curves as illustrated by the double reversal in curvature in those for the normalized and hot-rolled specimens (figs. 3 and 5) in contrast to the absence of reversals in those for the other specimens (figs. 2, 4, 6, 7). The influence of these factors will be reported in more detail later in the discussion of the diagrams representing the influence of the testing temperature on the mechanical properties of the iron.

IV. Influence of Temperature on the Work-Hardening Characteristics

The most satisfactory method of studying the work-hardening of metals is by means of the relation between true stress and true strain in a simple tension test in which the load and the change in diameter of the specimen are accurately measured throughout the entire test. As the term "work-hardening" relates to the increase of the true stress, σ, with increase in the true strain, δ, ($\delta = \log_e A_o/A$), the slope of the true stress-strain curve, $d\sigma/d\delta$, at any strain is a measure of the instantaneous rate of work-hardening at that strain. If aging or recovery occurs during the tension test, the total work-hardening is the combined effect of these factors and the ordinary strain-hardening, and $d\sigma/d\delta$ represents the instantaneous rate of the total work-hardening.

Several investigators [8, 10, 22, 28 to 31] have presented data indicating that the true stress-strain relationship for metals tested in tension is parabolic and may be expressed mathematically as follows

$$\sigma = k\delta^m, \tag{1}$$

in which k and m are constants, characteristic of the material. According to this relationship, the true stress and true strain values plotted on logarithmic coordinates should conform to a straight-line graph with the slope of the line equal to m. The coefficient m is generally designated the strain-hardening coefficient, and the rate of work-hardening is given by

$$\frac{d\sigma}{d\delta} = m\frac{\sigma}{\delta}, \tag{2}$$

if the relationship expressed in eq 1 is valid.

It should be pointed out, however, that many of the logarithmic true stress-strain curves, presented as evidence confirming the above parabolic relationship (eq 1) were plotted on scales of equal logarithmic cycle length for both axes, thus giving lines of very small slope. Any deviations from a linear relationship are not detected easily in graphs of this kind.

Now let any general relationship be assumed between the true stress σ and the true strain δ, namely $\sigma = f(\delta)$. If σ and δ are plotted on logarithmic coordinates, the slope, b, of such a curve at any point would be:

$$b = \frac{d(\log_e \sigma)}{d(\log_e \delta)} = \frac{d\sigma}{\sigma}\Big/\frac{d\delta}{\delta}, \tag{3}$$

and as

$$\delta = \log_e A_o/A, \tag{4}$$

then

$$d\delta = -dA/A. \tag{5}$$

Substituting in eq 3, one obtains

$$\frac{d\sigma}{\sigma}\Big/\frac{dA}{A}=-b/\delta. \tag{6}$$

At the upper and lower yield points and at maximum load (where $dL=d(\sigma A)=0$)

$$\frac{d\sigma}{\sigma}=-\frac{dA}{A}. \tag{7}$$

Substituting in eq 6, one obtains

$$\delta=b. \tag{8}$$

Therefore, the slope of a logarithmic true stress-strain curve at the upper and lower yield points and at the maximum load is equal to the respective strains at these points.

By substituting $b=\delta$ in eq 3, one obtains the relation

$$\frac{d\sigma}{d\delta}=\sigma \tag{9}$$

Thus, the rate of work-hardening at the upper and lower yield points and at the maximum load is equal to the respective true stresses at these points.

The relation expressed in eq 9 has been developed in a slightly different manner by Gensamer [29] and by Voce [21]. The relation, $\delta=m$ at the maximum load has been developed by Hollomon [10], although it was based on the true stress-strain relationship given in eq 1. However, as shown in the development presented above (eq 3 to 9), the relationships given in eq 8 and 9 do not depend upon any specified true stress-strain relation.

Hollomon [10] presented evidence indicating that the relationship $\sigma=k\delta^m$ was valid for plastic deformation beyond the end of initial yielding to that at the maximum load or to strains of about 0.4 for steels tested in tension. The results obtained in the present investigation, however, do not confirm this relationship; the true stress-strain values plotted on logarithmic coordinates do not necessarily show a linear relationship. Some of the data obtained in tension tests at various temperatures with the hot-rolled ingot iron are presented in figure 8. It should be noted that in this figure the length of a logarithmic cycle on the scale of true stress is twice that for the scale of true strain. This method of plotting reveals the curvature of these lines. The dashed lines in this figure are drawn through the points U, representing true stress-strain values at the maximum load, with the slopes of the lines equal to the strains at the maximum load ($b=\delta$). The true stress-strain values in the immediate vicinity of the maximum load conform very closely to these dashed lines. These lines, however, do not pass through the points, E, representing the end of the initial yielding.[2] Moreover, the true stress-strain values for deformation between the end of initial yielding and maximum load cannot be represented accurately by a straight line. Similar results were obtained in tension tests with the ingot iron in the other initial conditions. Thus, no constant work-hardening coefficient can be determined from these tension tests, and the work-hardening rates cannot be derived readily from the logarithmic true stress-strain graphs.

The work-hardening rate, $d\sigma/d\delta$, at any strain can be ascertained from the slope of the true stress-strain curves (figs. 2 to 7) at the designated strain, although some difficulty may be encountered in accurately determining the tangent line to the curve at the designated strain value. On the other hand, an average work-hardening rate, $\Delta\sigma/\Delta\delta$, over a range of strain $\Delta\delta$ can be determined readily from the true stress-strain curves. This method has been used in this investigation to determine the influence of temperature on the work-hardening characteristics of the ingot iron during the tension test. The results are summarized in figures 9 to 13. As the strain, M, at the minimum point of the true stress-strain curve after initiation of yielding varies with the temperature of the specimen, it was deemed advisable to choose this point as the initial reference point for the $\Delta\delta$ values. Thus the average work-hardening rates at the various temperatures for a specified strain range at the small strains are established from approximately corresponding portions of the true stress-strain curves. The broken-line curve through the completely filled circles in each figure represents the influence of the testing temperature on the rate of work-hardening at the maximum load, ($d\sigma/d\delta=\sigma$). Straight lines tangent to the true stress-strain curves at the maximum load point have slopes that agree very closely with the value of the true stress at the maximum load. These data are summarized in table 3.

All of the sets of curves in figures 9 to 13 have several features in common. The curves are generally lowered as the strain of the specimen increases; this change is greatest for the small strains and progressively decreases in magnitude as the strain increases. At the larger strains (strains from maximum load to fracture) the decrease in work-hardening rate with increase in strain is relatively small except at the very low temperatures. At very low temperatures the curves A for the smallest strain range, M to $M+0.02$ drop below some of those for the progressively larger strains. This factor reflects the influence of the testing temperature on the initial yielding of the specimen. At room temperature or at slightly elevated temperatures, the degree of heterogeneous deformation during the initial yielding was very small, and the corresponding true stress-strain curves (figs. 2 to 7) rise sharply after reaching the minimum true stress.[3] As the testing temperature

[2] In this investigation, the end of the nearly horizontal portion of the load-extension curve associated with the lower yield point was considered as the end of the initial yielding.

[3] The minimum of the true stress-strain curve at which $d\sigma/d\delta=0$, occurs at a slightly smaller strain than that at the minimum load of the lower yield point. At the latter point the slope of the true stress-strain curve must be positive and equal to the value of the true stress. The physical significance of the portion of the curves representing the initial yielding may be questionable, as these curves are based on average values of the true stress and strain during the heterogeneous deformation.

TABLE 3. *Rate of work-hardening of ingot iron specimens at the maximum load (1,000 psi)*

Temperature	As annealed		As normalized		As quenched and tempered		As hot-rolled		As cold-drawn 14% reduction of area		As cold-drawn 26% reduction of area	
	$\frac{d\sigma}{d\delta}$ [a]	σ [b]	$\frac{d\sigma}{d\delta}$ [a]	σ [b]	$\frac{d\sigma}{d\delta}$ [a]	σ [b]	$\frac{d\sigma}{d\delta}$ [a]	σ [b]	$\frac{d\sigma}{d\delta}$ [a]	σ [b]	$\frac{d\sigma}{d\delta}$ [a]	σ [b]
°C												
+100	65	66	73	72	57	58	65	68	72	73	80	80
+60	56	57	56	60	50	51	57	57	73	67	78	77
+30	54	53	55	56	52	52	55	55	68	69	78	81
−30	60	60	60	60	57	58	60	62	72	76	85	84
−78	65	65	66	67	63	63	68	68	84	82	96	96
−120	78	78	80	79	80	79	80	79	100	98	107	109
−138							85	85				
−154	94	92	100	98	100	95	100	102	110	112		
−188							120	124				
−196							130	130				

[a] Slope of tangent line to the true stress-strain curve at the maximum load.
[b] True stress at the maximum load.

is lowered, the strain during the initial yielding increases and the curve rises less abruptly beyond the minimum point. At the low temperatures, the relatively flat portion of the curve is an appreciable proportion of the total strain range $\Delta\delta$ from M to $M + 0.02$, and this factor is the cause of the lowering of the work-hardening curves A at the low temperatures. The sharp rise in these curves for the temperature range of room to +100° C is a result of the large increase in the magnitude of the strain-aging of the iron during the tension test.

The curves B to I of figures 9 to 13 are not appreciably affected by the sharpness of the rise of the true stress-strain curves beyond the minimum point, except curve B for the iron in the cold-drawn conditions. These curves are representative of the influence of the testing temperature on the total work-hardening characteristics of the iron for the designated strain ranges. They show a general trend of a decrease in the rate of total work-hardening with increase in temperature from −196° to about −120° C for some curves and from −154° to about −120° C for others. As the temperature is increased from −120° to −30° C, the total work-hardening rates for any specified strain range either remains approximately constant or increases. The work-hardening rates decrease as the temperature is increased from −30° to about +30° C and increase again as the temperature is raised to +100° C.

The rate of total work-hardening of the iron at the maximum load, irrespective of its initial condition, decreases continuously as the temperature is raised from −196° to about +30° C in some cases and from −154° to about +30° C in other cases, and usually increases with further increase of the temperature to +100° C. These curves are not a comparison of work-hardening rates at a constant strain, as the strain at maximum load in each case varied greatly with the testing temperature. They indicate the influence of the testing temperature on the rate of work-hardening of the iron at the maximum load conditions (eq 7, 8, and 9).

The portions of the total work-hardening curves (B to I in figs. 9 to 12) for temperatures ranging from −196° to −120° C for some curves and from −154° to −120° C for the others manifest the influence of a decrease in strain-hardening with increase in temperature, as the total work-hardening at these temperatures is mainly strain-hardening. However, as the temperature is increased above −120° C, the strain-aging becomes a significantly influencing factor in increasing the total work-hardening rates, and the magnitude of this factor is as great or greater than the decrease in the ordinary strain-hardening rates. Above about +30° C, the influence of the strain-aging predominates, and the total work-hardening rates increase greatly.

Another factor that probably has considerable influence on the variation of the rate of work-hardening with temperature is the mechanism of deformation. Deformation by twinning (Neumann bands) occurred in the specimens tested in tension at temperatures below −120° C, but no evidence of this was found in specimens tested at temperatures above −120° C. The extent of twinning during the tension test increased as the temperature was lowered from −120° to −196° C as illustrated by the microstructures (fig. 14) for the hot-rolled ingot iron. The twinning occured to a similar extent in the iron tested in the conditions as annealed, normalized, and quenched and tempered (fig. 15). The twinning in the iron in the conditions as cold-drawn was restricted to the portion of the specimens adjacent to the fracture, whereas it occurred throughout the entire gage length of the specimens of the iron in the other conditions (figs. 14 and 15). As twinning occurred in specimens deformed in tension but not extended to fracture at the low temperatures, it is considered that this phenomenon in iron is not primarily associated with the plastic deformation at the instant of fracture or any accompanying shock waves.

A comparison of graphs of work-hardening rates versus temperature (figs. 9 to 13) reveals that the initial condition of the iron influences the rate of total work-hardening at the various strain ranges up to about the strain at maximum load. The amount of carbon initially retained in solid solution and the size of the ferrite grains apparently affected the rate of work-hardening ($\Delta\sigma/\Delta\delta$) in this range of deformation. The curves A, B, C, and D for the quenched and tempered iron (fig. 11) show lower

work-hardening rates at most of the testing temperatures, especially in the range from about +30° to +100° C, than the corresponding curves for the normalized (fig. 10) or hot-rolled (fig. 12) irons. These lower values for the quenched and tempered iron probably are caused mainly by a decrease in the strain-aging as a result of the smaller amount of carbon retained in solid solution. The work-hardening rates were usually higher for the annealed (fig. 9) than for the quenched and tempered iron (fig. 11). As the amount of carbon retained in solid solution was approximately the same for the irons in these two conditions, the higher work-hardening rates of the annealed iron can be attributed to its coarser ferrite grains (ASTM No. 2 and 4, table 2). The rates for the annealed iron, in general, were slightly higher than those of either the normalized or hot-rolled irons, although the amount of carbon initially retained in solid solution of the annealed material was also lower than that of the other two conditions. This change in the positions of the curves may be attributed to the predominant effect of the coarser grain size of the annealed iron. Thus the rise in true stress between yield and maximum load is more rapid for the annealed iron than for the normalized or hot-rolled irons. The work-hardening characteristics of the normalized (fig. 10) and hot-rolled (fig. 12) irons were approximately alike, except in the temperature range of about +30° to +100° C, in which the strain-aging of the normalized iron was appreciably greater. The amount of carbon in solid solution prior to testing was considered to be about the same for the hot-rolled as for the normalized material. The rates of the work-hardening of the iron reduced 14 and 24 percent in area by cold-drawing, are considerably less than those of the iron in the other conditions. The strain-hardening and strain-aging accompanying the 14- and 24-percent reductions in area of the hot-rolled iron were greater when the iron was reduced by cold-drawing and subsequently aged in storage than when the reduction was obtained in an ordinary tension test.

V. Influence of Temperature on the Mechanical Properties

The influence of the testing temperature on yield stress, ultimate stress, true stresses at maximum load and at fracture, and true strains at maximum load and at fracture can be readily determined from the tension tests made at the various temperatures and the true stress-strain curves obtained from these tests. These data, as summarized in figures 16 to 21, show the relationship of some of these properties. It is apparent that the ratio of the values of true stress at maximum load to the ultimate stress for these curves will depend upon the strain at maximum load. The strains at maximum load varied considerably with the test temperature and the initial condition of the iron and usually decreased greatly at the very low temperatures. Thus some of the pairs of curves of ultimate stress, and true stress at maximum load, actually converge at the lowest temperatures. The dependence of the true stress at fracture on the strain at fracture is clearly shown in these figures and will be discussed later.

The combined effects of test temperature and initial condition of the iron on the above-mentioned mechanical properties are depicted in the composite diagrams of figures 22 to 27. The curves for the lower yield stress (fig. 22) depict closely the effect of temperature on the initial strength (initial resistance to flow) of the iron in the various conditions. The effect of strain-aging during the initial yielding on the yield strength was relatively small or negligible at temperatures in the range 0° to −196° C. The lower yield stress, and hence the initial strength of the iron, increased continuously with lowering of the temperature in this range; this increase in yield stress with lowering of the temperature from 0° to −196° C was about 70,000 psi for the iron in each of the initial conditions. At temperatures in the range of 0° to +100° C, however, the strain-aging of the iron during the initial yielding was usually appreciable and is depicted by a leveling off or a slight rise of the curves with increase in temperature in this range. Thus these curves do not necessarily indicate an increase in the initial strength of the irons with increase in temperature from 0° to + 100° C.

The combined effects of the ferrite grain size and the solubility of carbon on the initial strength of the iron are indicated in the relative positions of the yield stress curves (fig. 22). The hot-rolled iron (ASTM grain No. 4 to 5) and the normalized iron, (ASTM grain No. 3 to 4) should have about the same amount of carbon retained in solid solution. At each test temperature throughout the range of −196° to +100° C, however, the yield stress of the hot-rolled material (curve *B*) is higher than the corresponding yield stress of the normalized material (curve *F*). Similarly, curve *E*, for the quenched and tempered iron (ASTM grain No. 4 to 5), is higher throughout this temperature range than curve *A*, for the annealed iron (ASTM grain No. 2 to 3), even though both conditions are considered to have about the same amount of carbon retained in solid solution. These results show a general trend of an increase in yield stress as the ferrite grain size decreases. It is noteworthy, however, that the relatively high yield strengths (curves *C* and *D* of fig. 22) and also the relatively high ultimate stresses and true stresses at maximum load (curves *C* and *D* of figs. 23 and 24) of the cold-drawn irons are due to the strain-hardening and strain-aging during the prior cold-drawing operations and the aging during storage. These high-strength values are not due to a grain size factor, as the average ferrite grain size was the same for the hot-rolled, quenched and tempered, and cold-drawn conditions.

The ultimate stress (fig. 23) and true stress at maximum load (fig. 24) both increased as the test temperature was decreased from about +30° to −196° C; the true stress at maximum load of the annealed specimens did not change appreciably as the temperature was decreased from −154° to −196° C. Both stresses either changed little or

increased slightly as the temperature was raised from about +30° to +60° C, and both increased considerably as the temperature was raised from +60° to +100° C, because of the increase with temperature of the strain-aging accompanying the deformation. The strain-aging varies with the initial condition of the iron and especially with the amount of carbon initially retained in solid solution. Thus, the ultimate stresses and true stresses at maximum load for the hot-rolled iron (curves *B*) are relatively higher at temperatures above −120° C than those for the quenched and tempered iron (curves *E*), even though the average grain size was the same. These values for the normalized iron (curves *F*) are relatively higher at most of the test temperatures above −120° C, than those for the annealed iron (curves *A*). This would be expected, as the normalized iron initially had a smaller ferrite grain size and retained more carbon in solid solution. However, it is believed the effect of the ferrite grain size on the strain-aging was relatively small. The increase in ultimate stress and true stress at maximum load with increase in temperature in the range +60° to +100° C for the cold-drawn iron (curves *C* and *D*) was relatively small, as appreciable strain-aging had occurred during cold-drawing and subsequent storage. At the very low temperatures, −154° to −196° C, the relative positions of the curves of true stress at maximum load (fig. 24) depend greatly upon the strain at maximum load; the greater the strain the greater is the true stress.

The curves representing the influence of test temperature on true strain at maximum load are shown in figure 25. The strains at maximum load for the annealed (curve *A*), hot-rolled (curve *B*), normalized (curve *F*), and quenched and tempered (curve *E*) irons show certain common features. The strains remained approximately constant at test temperatures ranging from +60° to −30° C and, in general, decreased as the temperature was lowered from −30° to −196° C. The curve *B* for the hot-rolled iron however, exhibits a moderate increase in strain as the temperature is lowered from about −125° to −160° C; a smaller increase is also noted in the curve *F* for the normalized iron. At a temperature of −196° C, the strains at maximum load apparently were influenced greatly by the ferrite grain size; the larger the grain size the smaller was the strain. The strain for the annealed iron was considerably smaller than that for the quenched and tempered iron. The iron in both conditions was considered to have about the same amount of carbon initially retained in solid solution. Similarly, the strain at −196° C for the normalized iron was considerably smaller than that of the hot-rolled iron.

The strains at maximum load for the cold-drawn irons (curves *C* and *D*), as a result of the strain-hardening and strain-aging prior to test are very much smaller than those for the iron in the other conditions. It should be pointed out, however, that the temperatures at which the strain begins to decrease rapidly with decrease in temperature are about 100 deg. C lower for the cold-drawn irons than for the other irons.

The curves representing the influence of test temperature on the true strain at fracture are shown in figure 26; the true strain at fracture is a measure of the ductility of a metal. Curves *A*, *E*, *C*, and *D* for the annealed, quenched and tempered, and cold drawn irons are similar in shape. As the temperature is decreased from +100° to −196° C, the ductility first gradually rises to a maximum and then decreases continuously to very low values at −196° C. There is no abrupt change in the slope of these curves (*A*, *E*, *C*, and *D*) and no sharp transition temperature.[4] The ductility at fracture of the hot-rolled and normalized irons varied considerably with the test temperature, and two maxima are exhibited in each curve (curves *B* and *F*). The ductility was greatly reduced as the temperature was lowered from −30° to −78° for curve *F*, and to −120° C for curve *B*. With further decrease in temperature to −154° C, however, the ductility increased slightly and then decreased greatly as the temperature was lowered to −196° C. As mentioned earlier, the curves representing the ductility at maximum load of the iron in these two conditions (fig. 25) exhibit the same trend, although to a smaller extent. This characteristic is probably associated in some way with the greater amount of carbon initially retained in solid solution in these irons than in the other irons.

The temperature at which the maximum ductility is retained depends upon the initial condition of the iron (fig. 26). This temperature is highest for the normalized iron, curve *F*, and lowest for the cold-drawn iron, curves *C* and *D*. The temperature of the maximum ductility of the cold-drawn irons is about 50° C below that of the hot-rolled iron, curve *B*. The reduction in the amount of carbon retained in solid solution by the strain-aging of the iron during the cold-drawing operations and storage resulted in a shift of the temperature of maximum ductility to a lower value.

The fracture stress curves (fig. 27) indicate a general trend of an increase in fracture stress with decrease in temperature between +30° and about −160° C. However, many deviations from this trend are shown in the curves. All of the stress values are decreased as the temperature is lowered from about −160° to −196° C because of the large decrease in ductility. The increase in the fracture stress values accompanying a rise of testing temperature from +60° to +100° C is due to the predominant influence of the strain-aging. The curves *B* and *F* for the hot-rolled and normalized irons exhibit a large decrease in fracture stress values as the temperature is lowered from about −30° to about −80° C, a direct result of the rapid decrease in ductility of the specimens as the temperature is lowered through this range (fig. 26).

The influence of prior cold-drawing of the hot-rolled iron on the fracture stress, as determined in

[4] A transition temperature is generally considered as a narrow temperature range in which the fracture changes from a shear to a cleavage type accompanied by a large decrease in ductility.

subsequent tension tests, is also illustrated in figure 27 by the shape of the curves *B*, *C*, and *D*. The strain-hardening and strain-aging accompanying the cold-drawing of the iron and aging during subsequent storage did not completely remove all of the characteristics specific to the hot-rolled iron. Curve *C* for the iron reduced 14 percent in area by cold-drawing exhibits a smaller dip in the region near −78° C than that in curve *B* for the hot-rolled iron. Cold-drawing of the iron to 24-percent reduction in area was sufficient to eliminate the dip in the fracture stress curve *D* in the region near −78° C.

The reduction of the amount of carbon retained in solid solution by a heat treatment of the initially hot-rolled iron, such as represented by the quenched and tempered, or annealed condition, also influences the fracture stresses as indicated by a nearly continuous rise of the curves *E* and *A* of figure 27 as the temperature is lowered from about +30° to about −160° C.

VI. Summary

True stress-strain curves for ingot iron in various conditions and tested in tension at temperatures ranging from −196° to +100° C, are presented. Derived graphs also are presented showing the effects of the testing temperature and initial condition of the ingot iron on the mechanical properties and work-hardening characteristics.

The true stress-strain curves for tension tests at temperatures ranging from −196° to +100° C with annealed, normalized, quenched and tempered, hot-rolled and cold-drawn ingot iron are not linear between maximum load and fracture; the divergence from a linear relationship generally increases as the testing temperature is lowered.

The logarithmic graphs of the true stress-strain data for ingot iron tested in tension at temperatures ranging from −196° to +100° C are not linear, and thus the true stress-strain relationship cannot be represented accurately by the equation, $\sigma = k\delta^m$.

The plastic deformation of the ingot iron is not uniform during extension. Some local contraction usually occurs at the initial yielding of the iron and during deformation between yield and maximum load. The deformation from maximum load to fracture is frequently nonuniform, as indicated by a cyclic trend in this portion of the true stress-strain curves.

The "rim effect" obtained during the fracture of ingot iron is considerable except at the very low testing temperatures. Accurate values of the fracture stress, therefore, cannot be determined from diameter measurements of the ingot iron specimens after fracture, except possibly for those tested at very low temperatures.

Deformation by twinning (Neumann bands) occurs during the deformation of specimens of ingot iron tested in tension at temperatures below −120° C, and the amount of twinning depends upon the testing temperature and the prior strain history of the specimen; the twinning increases with decrease of temperature below −120° C and decreases with prior cold-working of the iron at room temperature.

The work-hardening of ingot iron during test in tension at temperatures below −120° C is mainly strain-hardening, and the rate of total work-hardening increases with decrease in the testing temperature. As the temperature is increased above −120° C, the influence of strain-aging in increasing the total work-hardening rate appears to be appreciable. Above room temperature strain-aging is the predominating factor, and the total work-hardening rate increases greatly with increase in temperature.

The effect of the ferrite grain size is manifested in the yield stress values; the yield stress decreases with increase in the grain size. The work-hardening rates at very small strains also are influenced by the ferrite grain size; the rate increases with increase in the grain size. The difference in the grain size of the iron in the various initial conditions, however, was not sufficient to greatly affect the other mechanical properties.

The variation of the strains at maximum load and at fracture with temperature, as determined in tension tests, depends upon the initial condition of the iron; it varies with the amount of carbon retained in solid solution and the prior strain history. The transition temperature ranges, as determined by variations in the strains at fracture, in general, are relatively broad.

The fracture stress curves (true stress at initial fracture) show a trend of an increase in the fracture stress values with decrease in testing temperature below room temperature. However, several factors, such as strain-hardening, strain-aging, and strain at fracture greatly influence the fracture stresses and result in many deviations from this trend.

The authors are indebted to C. R. Johnson, R. L. Bloss, Lavaria B. Weinrich, and Fannie A. Wilkinson for assistance in this investigation.

VII. References

[1] P. Ludwik, Elemente der technologischen Mechanik (Julius Springer, Berlin, 1909).

[2] C. W. MacGregor, The true stress-strain tension test—its role in modern materials testing, J. Franklin Inst. **238,** 111, 159 (1944).

[3] E. Voce, True stress-strain curves, Metal Treatment **15,** 53 (summer 1948).

[4] G. W. Geil and N. L. Carwile, A reduction-of-area gage for use at low temperatures, J. Research NBS **43,** 527 (1949) RP2044.

[5] C. W. MacGregor, Relation between stress and reduction in area for tensile tests of metals, Trans. Am. Inst. Min. Met. Engrs. **124,** 208 (1937).

[6] M. Gensamer, E. B. Pearsall, and G. V. Smith, The mechanical properties of the isothermal decomposition products of austenite, Trans. Am. Soc. Metals **28,** 380 (1940).

[7] C. E. Lacy and M. Gensamer, The tensile properties of alloyed ferrites, Trans. Am. Soc. Metals **32,** 88 (1944).

[8] J. H. Hollomon, The effect of heat treatment and carbon content on the work hardening characteristics of several steels, Trans. Am. Soc. Metals **32,** 123 (1944).

[9] C. Zener and J. H. Hollomon, Plastic flow and rupture of metals, Trans. Am. Soc. Metals **33,** 163 (1944).

[10] John H. Hollomon, Tensile deformation, Trans. Am. Inst. Min. Met. Engrs. **162,** 268 (1945).

[11] T. A. Read, H. Markus, and J. M. McCaughey, Plastic flow and rupture of steel at high hardness levels—part of book Fracturing of metals, Am. Soc. Metals (Cleveland, Ohio, 1948).

[12] L. Siegle, Effect of ferritic grain size on the true stress-strain tensile properties and notch impact strength of ingot iron at low temperatures. Thesis presented to the Graduate School, Univ. Pennsylvania (1948).

[13] E. J. Ripling, Tensile properties of a heat treated low alloy steel at subzero temperatures, Am. Soc. Metals Preprint No. 1 (1949).

[14] E. J. Ripling and G. Sachs, The effect of strain-temperature history on the flow and fracture characteristics of an annealed steel, J. Metals **1,** Sec. 3, 205 (1949).

[15] J. E. Dorn, A. Goldberg, and T. E. Tietz, The effect of thermal-mechanical history on the strain hardening of metals, Trans. Am. Inst. Min. Met. Engrs. **180,** 205 (1949).

[16] D. J. McAdam, Jr., G. W. Geil, and W. D. Jenkins, Influence of plastic extension and compression on the fracture stress of metals, Trans. Am. Soc. Testing Materials **47,** 554 (1947).

[17] D. J. McAdam, Jr., G. W. Geil, and R. W. Mebs, Influence of plastic deformation, combined stresses and low temperatures on the breaking stress of ferritic steels, Trans. Am. Inst. Min. Met. Engrs. **172,** 323 (1947).

[18] D. J. McAdam, Jr., G. W. Geil, D. H. Woodard, and W. D. Jenkins, Influence of size and the stress system on the flow stress and fracture stress of metals, Trans. Am. Inst. Min. Met. Engrs. **180,** 363 (1949).

[19] D. J. McAdam, Jr., G. W. Geil, and Frances Jane Cromwell, Flow, fracture and ductility of metals, Trans. Am. Inst. Min. Met. Engrs. **175,** 306 (1948).

[20] D. J. McAdam, Jr., G. W. Geil, D. H. Woodard, and W. D. Jenkins, Influence of strain aging on the fracture stress of low carbon steel, Trans. Am. Inst. Min. Met. Engrs. **176,** 436 (1948).

[21] E. Voce, The relationship between stress and strain for homogeneous deformation, J. Inst. Metals **74,** 537 (1948).

[22] M. Gensamer, E. Saibel, J. T. Ransom, and R. E. Lowrie, The fracture of metals (Am. Weld. Soc., New York, N. Y., 1947).

[23] L. Siegle and R. M. Brick, mechanical properties of metals at low temperatures: A survey, Trans. Am. Soc. Metals **40,** 813 (1948).

[24] J. H. Hollomon, The problem of fracture, Welding J. **25,** Res. Supplement 534s (1946).

[25] H. W. Gillett and F. T. McGuire, Behavior of ferritic steels at low temperatures, Nat. Research Council War Met. Comm. Reports No. W–78 and W–118 (June 1944).

[26] A. E. White and C. A. Siebert, Report on literature survey on low temperature properties of metals (J. W. Edwards, Ann Arbor, Mich., 1947).

[27] E. Orowan, Fracture and strength of solids, Report to Ministry of Supply, United Kingdom (1949).

[28] M. Gensamer, Strength and ductility, Trans. Am. Soc. Metals **36,** 30 (1946)

[29] M. Gensamer, The yield point in metals, Trans. Am. Inst. Min. Met. Engrs. **128,** 104 (1938).

[30] J. R. Low, Jr. and T. A. Prater, Final report on plastic flow of aluminum aircraft sheet under combined loads—II OSRD Report No. 4052 (Aug. 22, 1944).

[31] J. R. Low, Jr. and F. Garofalo, Precision determination of stress-strain curves in the plastic range, Proc. Soc. Exper. Stress Anal. **4,** [2], 16 (1947).

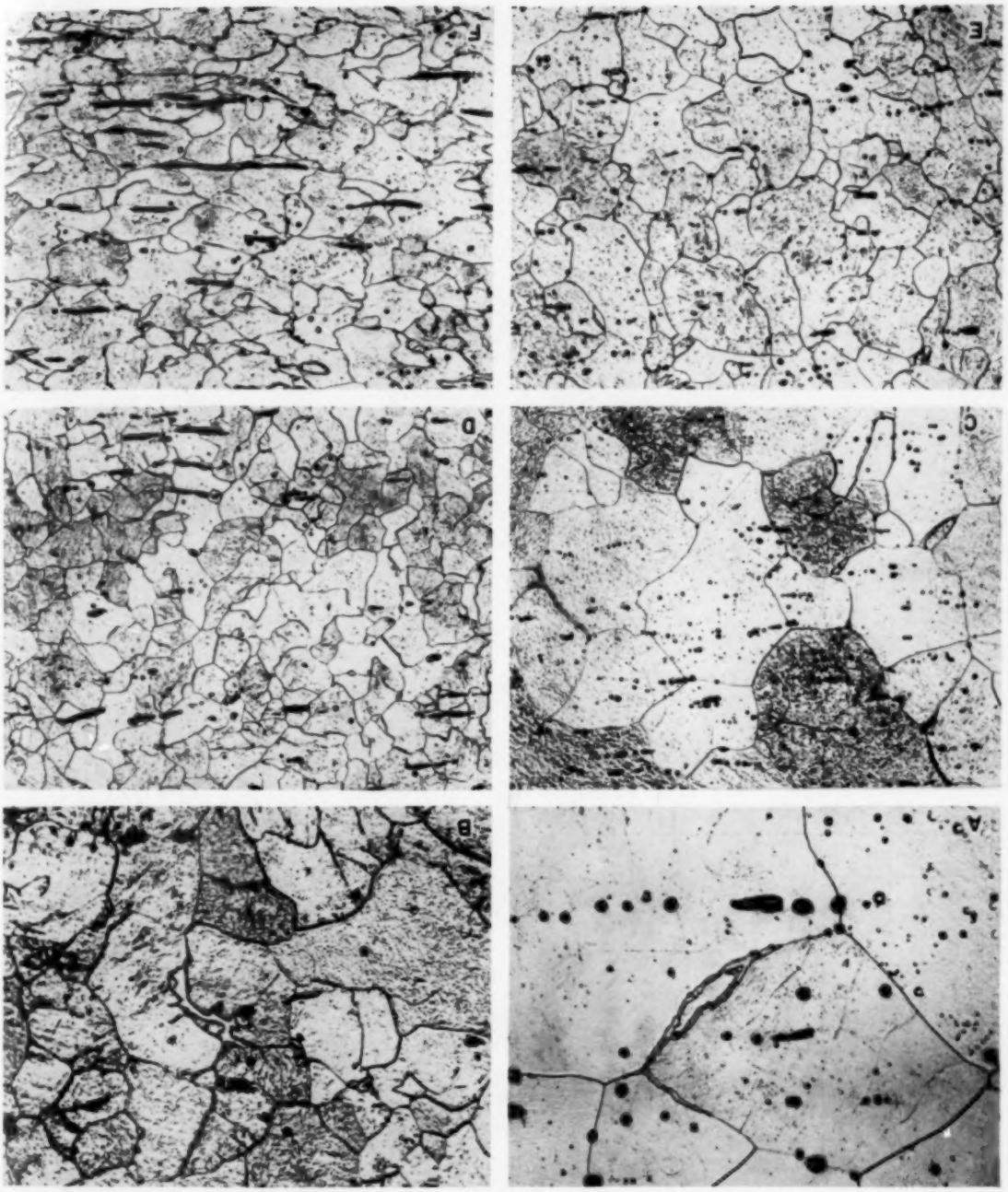

FIGURE 1. *Microstructure of the ingot iron in various initial conditions; etched with 4-percent nital, A and B, ×250, others all ×100.*

A and *C*, annealed; *B*, quenched and tempered; *D*, hot-rolled; *E*, normalized; *F*, cold-drawn to 24-percent reduction of area.

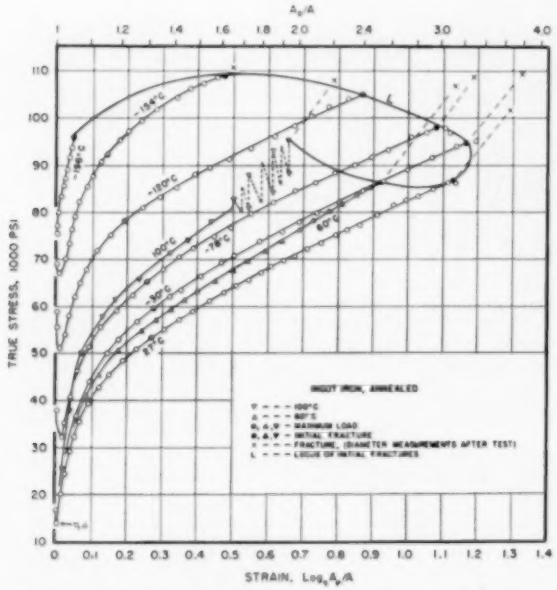

FIGURE 2. *True stress-strain curves obtained in tension tests at various temperatures with annealed ingot iron.*

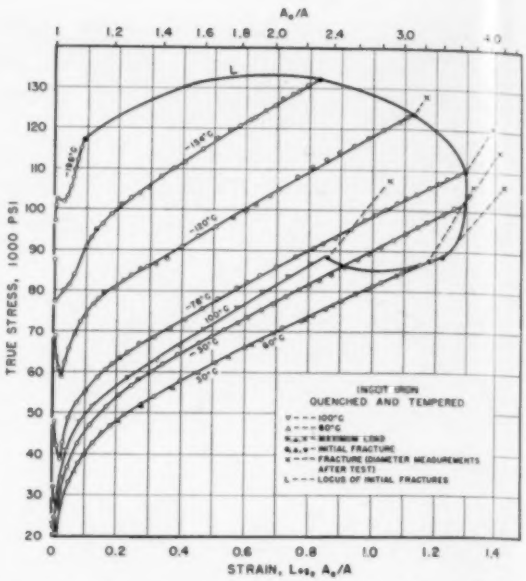

FIGURE 4. *True stress-strain curves obtained in tension tests at various temperatures with quenched and tempered ingot iron.*

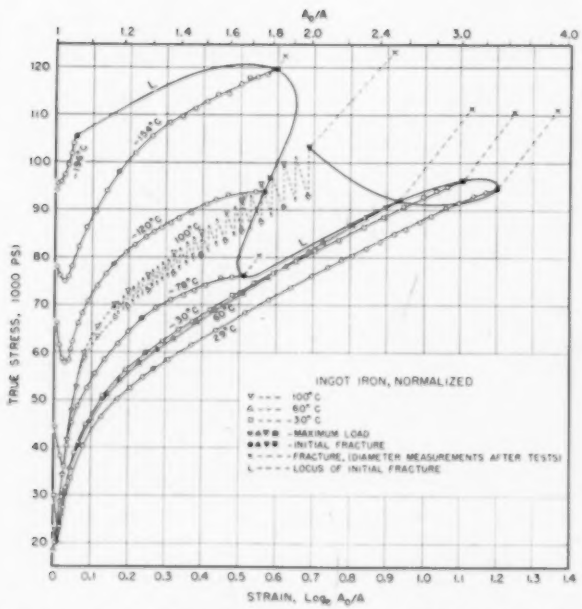

FIGURE 3. *True stress-strain curves obtained in tension tests at various temperatures with normalized ingot iron.*

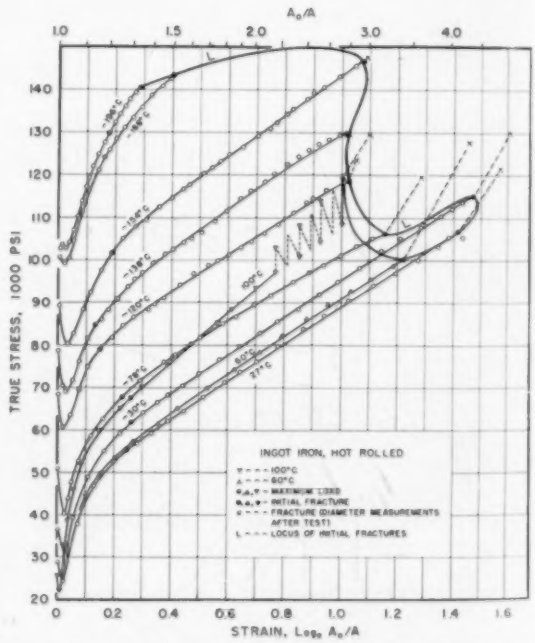

FIGURE 5. *True stress-strain curves obtained in tension tests at various temperatures with hot-rolled ingot iron.*

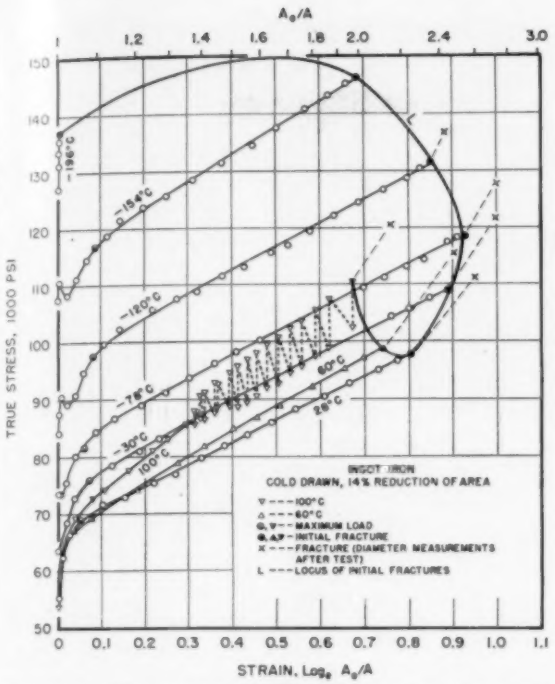

FIGURE 6. *True stress-strain curves obtained in tension tests at various temperatures with ingot iron as cold-drawn, 14-percent reduction of area.*

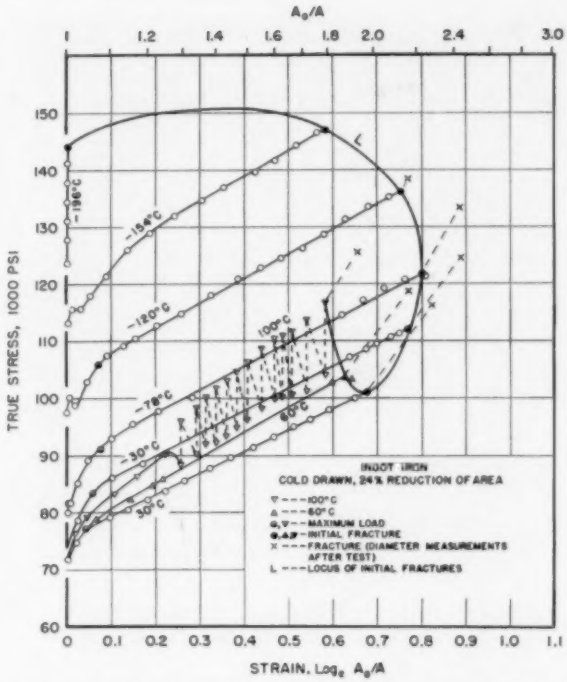

FIGURE 7. *True stress-strain curves obtained in tension tests at various temperatures with ingot iron as cold-drawn, 24-percent reduction of area.*

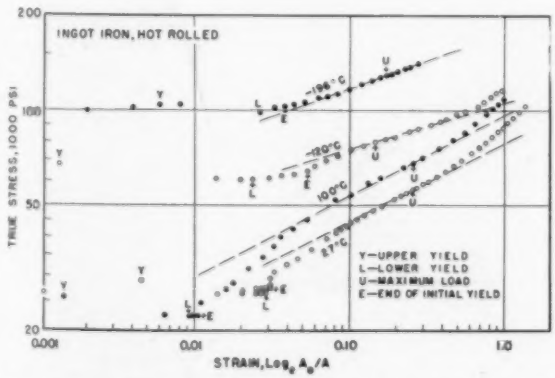

FIGURE 8. *Logarithmic true stress-strain curves obtained in tension tests at various temperatures with hot-rolled ingot iron.*

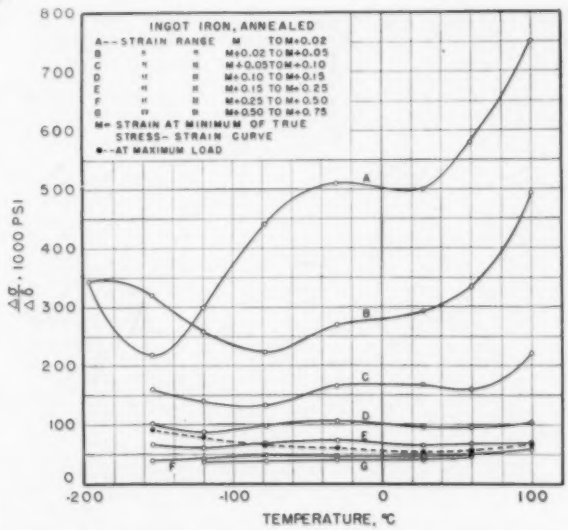
INGOT IRON, ANNEALED
A--STRAIN RANGE M TO M+0.02
B " " M+0.02 TO M+0.05
C " " M+0.05 TO M+0.10
D " " M+0.10 TO M+0.15
E " " M+0.15 TO M+0.25
F " " M+0.25 TO M+0.50
G " " M+0.50 TO M+0.75
M= STRAIN AT MINIMUM OF TRUE STRESS- STRAIN CURVE
●--AT MAXIMUM LOAD
Δσ/Δδ - 1000 PSI
TEMPERATURE, °C

FIGURE 9. *Effect of testing temperature on the rate of work-hardening of annealed ingot iron.*

899983—50——3

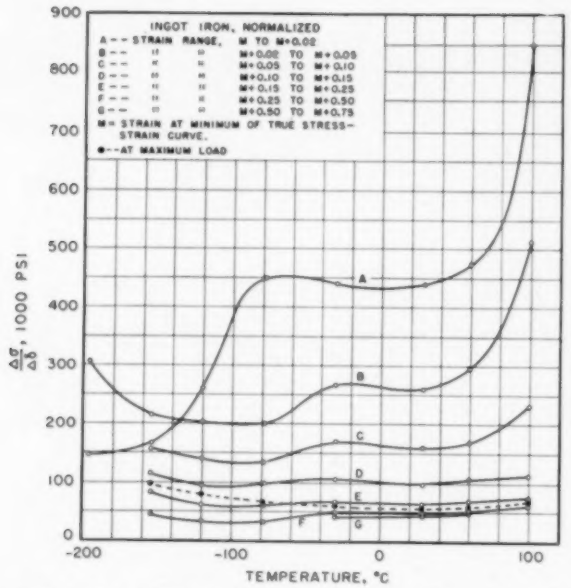
INGOT IRON, NORMALIZED
A -- STRAIN RANGE, M TO M+0.02
B -- " " M+0.02 TO M+0.05
C -- " " M+0.05 TO M+0.10
D -- " " M+0.10 TO M+0.15
E -- " " M+0.15 TO M+0.25
F -- " " M+0.25 TO M+0.50
G -- " " M+0.50 TO M+0.75
M= STRAIN AT MINIMUM OF TRUE STRESS-STRAIN CURVE.
●--AT MAXIMUM LOAD
Δσ/Δδ, 1000 PSI
TEMPERATURE, °C

FIGURE 10. *Effect of testing temperature on the rate of work-hardening of normalized ingot iron.*

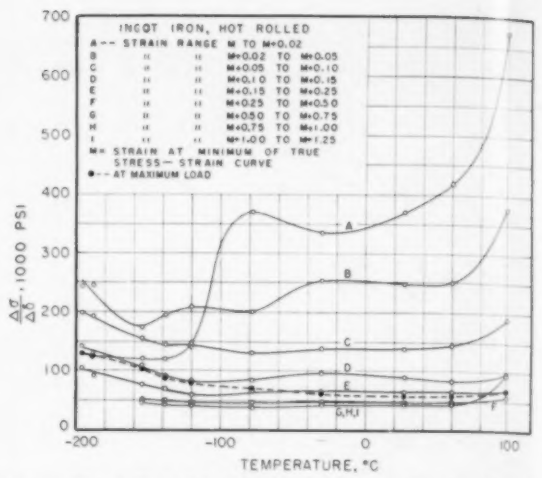
INGOT IRON, HOT ROLLED
A -- STRAIN RANGE M TO M+0.02
B " " M+0.02 TO M+0.05
C " " M+0.05 TO M+0.10
D " " M+0.10 TO M+0.15
E " " M+0.15 TO M+0.25
F " " M+0.25 TO M+0.50
G " " M+0.50 TO M+0.75
H " " M+0.75 TO M+1.00
I " " M+1.00 TO M+1.25
M= STRAIN AT MINIMUM OF TRUE STRESS-STRAIN CURVE
●-- AT MAXIMUM LOAD
Δσ/Δδ, 1000 PSI
TEMPERATURE, °C

FIGURE 12. *Effect of testing temperature on the rate of work-hardening of hot-rolled ingot iron.*

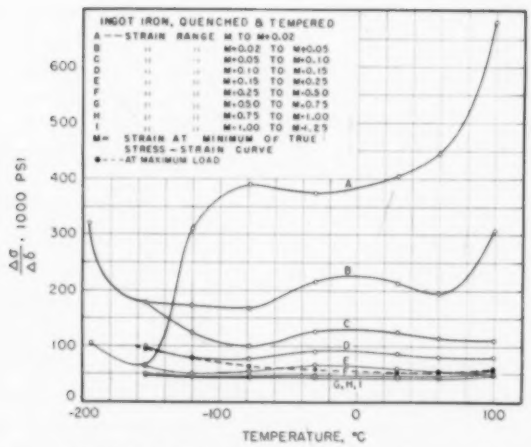
INGOT IRON, QUENCHED & TEMPERED
A -- STRAIN RANGE M TO M+0.02
B " " M+0.02 TO M+0.05
C " " M+0.05 TO M+0.10
D " " M+0.10 TO M+0.15
E " " M+0.15 TO M+0.25
F " " M+0.25 TO M+0.50
G " " M+0.50 TO M+0.75
H " " M+0.75 TO M+1.00
I " " M+1.00 TO M+1.25
M= STRAIN AT MINIMUM OF TRUE STRESS-STRAIN CURVE
●--AT MAXIMUM LOAD
Δσ/Δδ, 1000 PSI
TEMPERATURE, °C

FIGURE 11. *Effect of testing temperature on the rate of work-hardening of quenched and tempered ingot iron.*

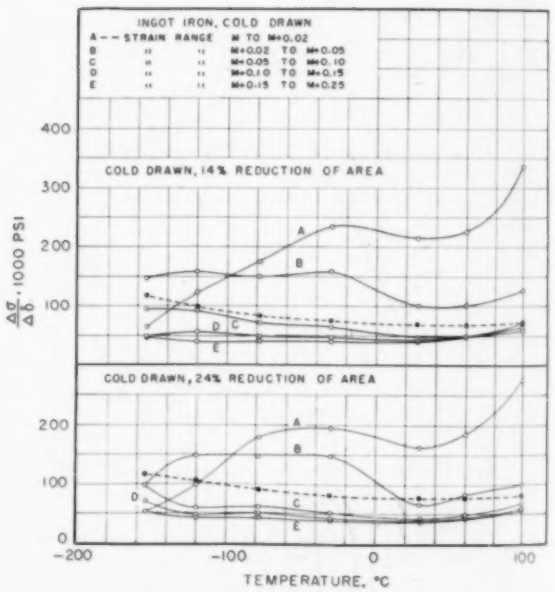
INGOT IRON, COLD DRAWN
A -- STRAIN RANGE M TO M+0.02
B " " M+0.02 TO M+0.05
C " " M+0.05 TO M+0.10
D " " M+0.10 TO M+0.15
E " " M+0.15 TO M+0.25
COLD DRAWN, 14% REDUCTION OF AREA
COLD DRAWN, 24% REDUCTION OF AREA
Δσ/Δδ, 1000 PSI
TEMPERATURE, °C

FIGURE 13. *Effect of testing temperature on the rate of work-hardening of cold-drawn ingot iron.*

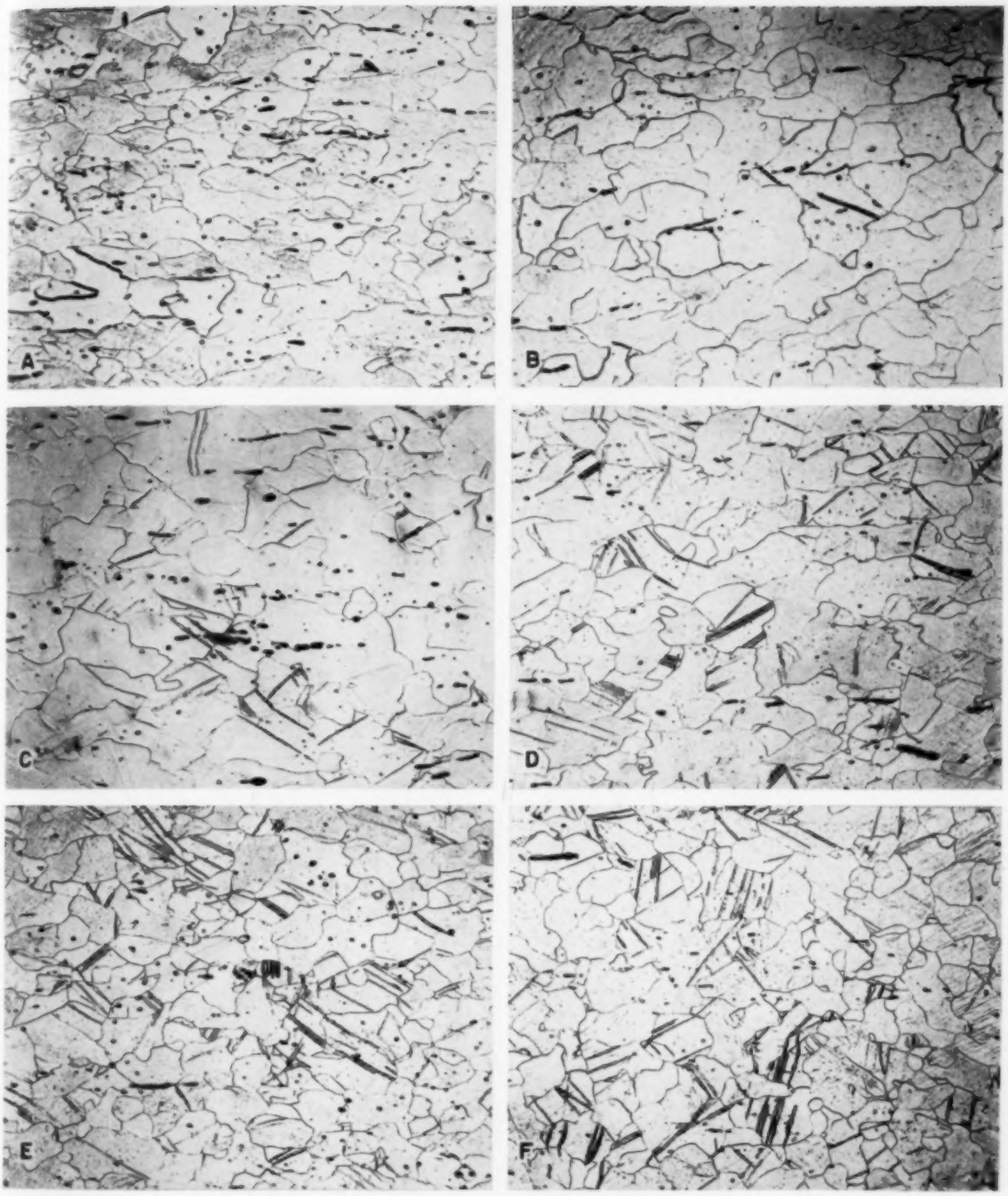

FIGURE 14. *Microstructure of the hot-rolled ingot iron after tests in tension at various temperatures. F, Structure 1 in. from fracture, others all ⅜ in. from fracture; etched with 4-percent nital, ×100.*

A, −120° C; *B*, −138° C; *C*, −154° C; *D*, −188° C; *E* and *F*, −196° C.

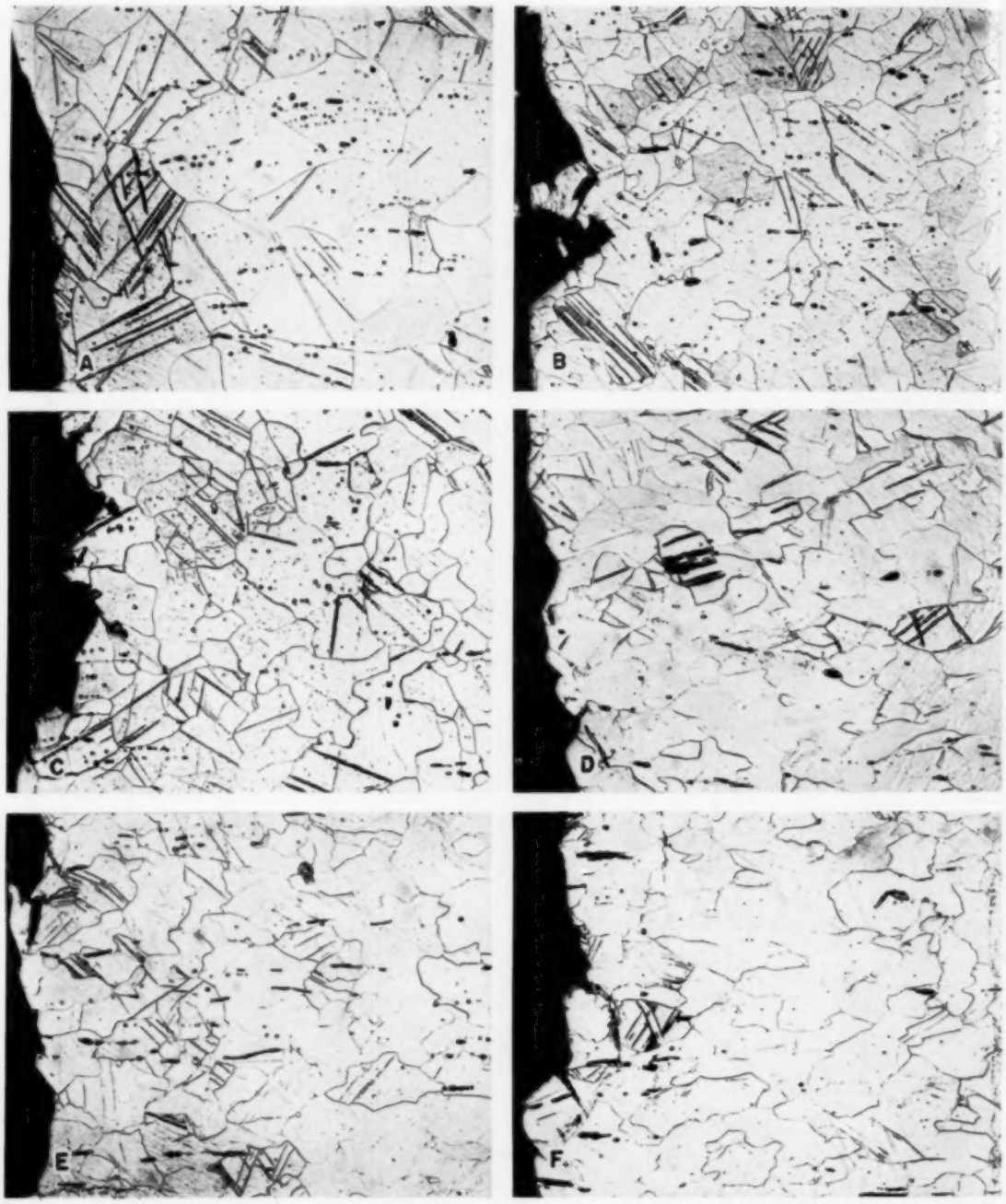

FIGURE 15. *Microstructure of the fracture region, after test in tension at −196° C with ingot iron in various conditions; etched with 4 percent nital, ×100.*

A, annealed; *B*, quenched and tempered; *C*, normalized; *D*, hot-rolled; *E*, cold-drawn, 14-percent reduction of area; *F*, cold-drawn, 24-percent reduction of area.

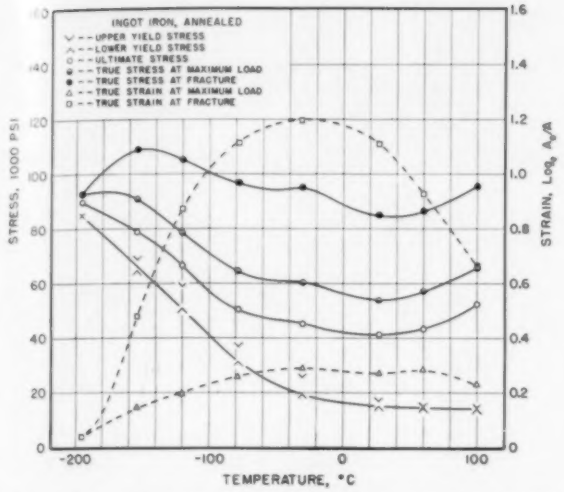

FIGURE 16. *Effect of testing temperature on various mechanical properties of the annealed ingot iron.*

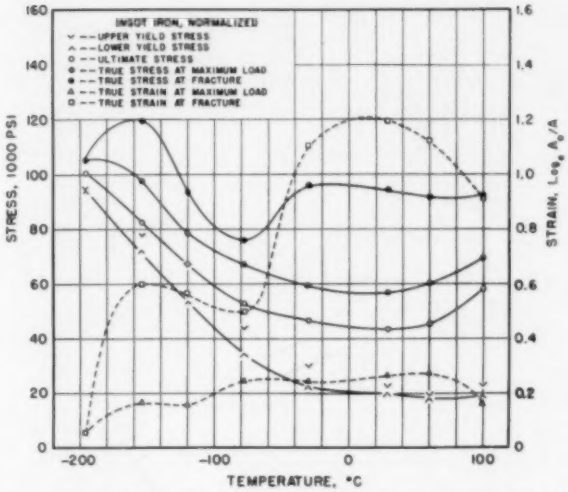

FIGURE 17. *Effect of testing temperature on various mechanical properties of the normalized ingot iron.*

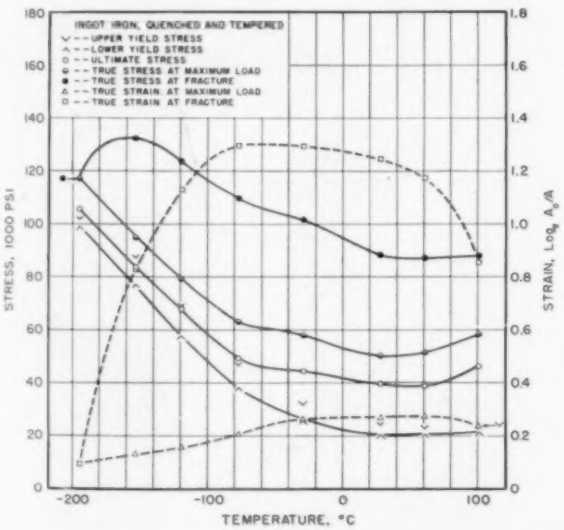

FIGURE 18. *Effect of testing temperature on various mechanical properties of the quenched and tempered ingot iron.*

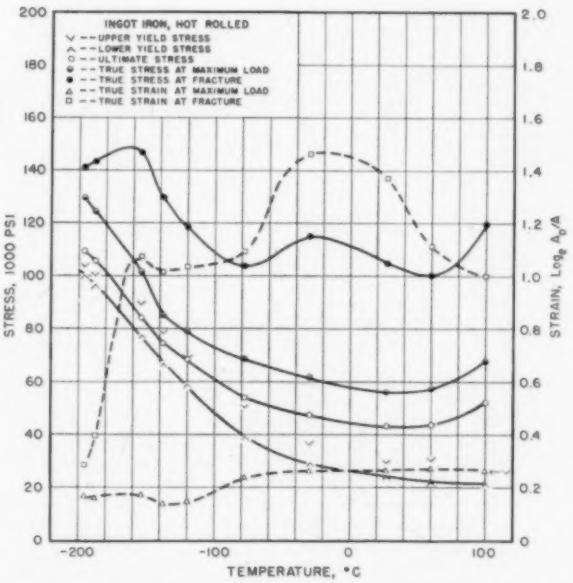

FIGURE 19. *Effect of testing temperature on various mechanical properties of the hot-rolled ingot iron.*

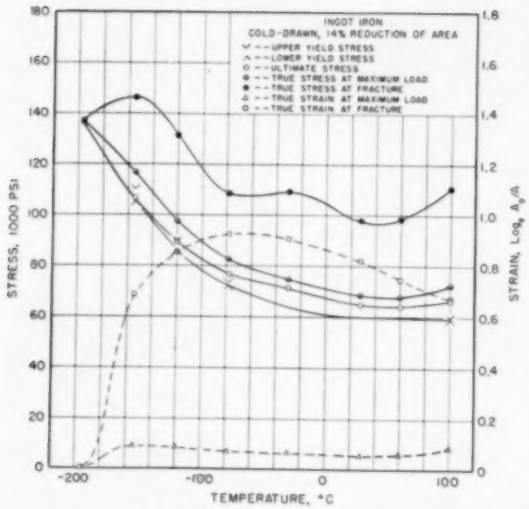

FIGURE 20. *Effect of testing temperature on various mechanical properties of the ingot iron as cold-drawn, 14-percent reduction of area.*

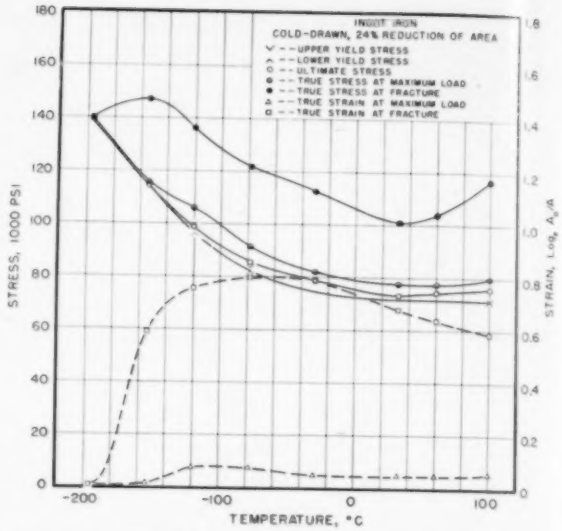

FIGURE 21. *Effect of testing temperature on various mechanical properties of the ingot iron as cold-drawn, 24-percent reduction of area.*

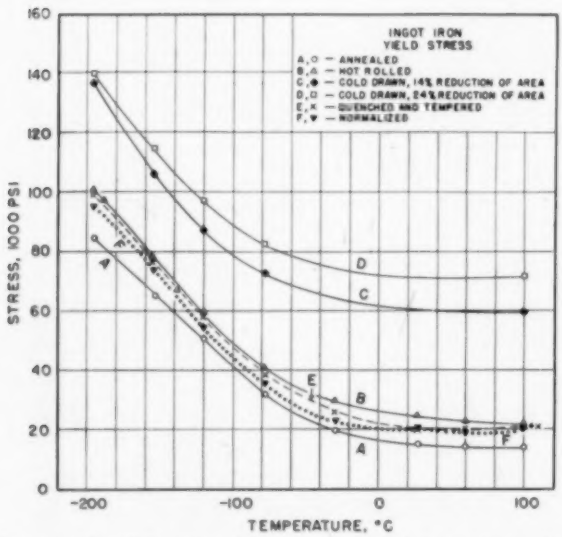
INGOT IRON
YIELD STRESS
A, ○ — ANNEALED
B, △ — HOT ROLLED
C, ◆ — COLD DRAWN, 14% REDUCTION OF AREA
D, □ — COLD DRAWN, 24% REDUCTION OF AREA
E, × — QUENCHED AND TEMPERED
F, ▼ — NORMALIZED
STRESS, 1000 PSI
TEMPERATURE, °C

FIGURE 22. *Effect of testing temperature and the initial condition of the ingot iron on the lower yield stress.*

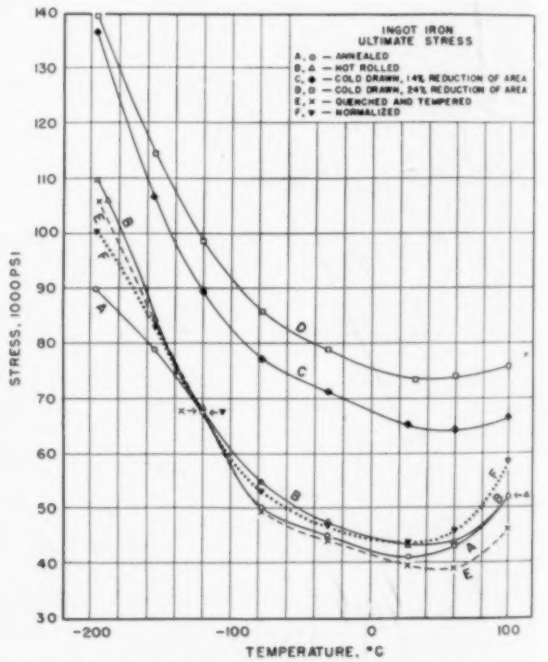
INGOT IRON
ULTIMATE STRESS
A, ○ — ANNEALED
B, △ — HOT ROLLED
C, ◆ — COLD DRAWN, 14% REDUCTION OF AREA
D, □ — COLD DRAWN, 24% REDUCTION OF AREA
E, × — QUENCHED AND TEMPERED
F, ▼ — NORMALIZED
STRESS, 1000 PSI
TEMPERATURE, °C

FIGURE 23. *Effect of testing temperature and the initial condition of the ingot iron on the ultimate stress.*

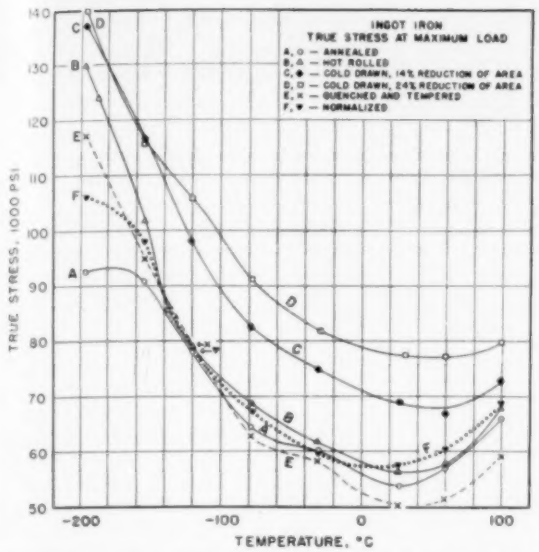
INGOT IRON
TRUE STRESS AT MAXIMUM LOAD
A, ○ — ANNEALED
B, △ — HOT ROLLED
C, ◆ — COLD DRAWN, 14% REDUCTION OF AREA
D, □ — COLD DRAWN, 24% REDUCTION OF AREA
E, × — QUENCHED AND TEMPERED
F, ▼ — NORMALIZED
TRUE STRESS, 1000 PSI
TEMPERATURE, °C

FIGURE 24. *Effect of testing temperature and the initial condition of the ingot iron on the true stress at maximum load.*

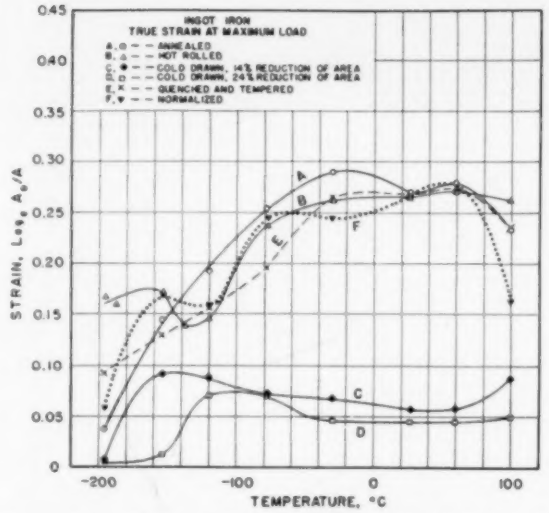
INGOT IRON
TRUE STRAIN AT MAXIMUM LOAD
A, ○ — ANNEALED
B, △ — HOT ROLLED
C, ◆ — COLD DRAWN, 14% REDUCTION OF AREA
D, □ — COLD DRAWN, 24% REDUCTION OF AREA
E, × — QUENCHED AND TEMPERED
F, ▼ — NORMALIZED
STRAIN, Log$_e$ A_o/A
TEMPERATURE, °C

FIGURE 25. *Effect of testing temperature and the initial condition of the ingot iron on the strain at maximum load.*

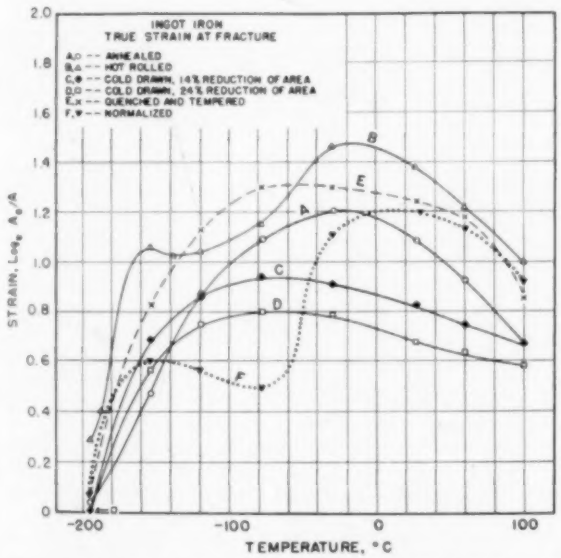
INGOT IRON
TRUE STRAIN AT FRACTURE
A, ○ — ANNEALED
B, △ — HOT ROLLED
C, ◆ — COLD DRAWN, 14% REDUCTION OF AREA
D, □ — COLD DRAWN, 24% REDUCTION OF AREA
E, × — QUENCHED AND TEMPERED
F, ▼ — NORMALIZED
STRAIN, Log$_e$ A_o/A
TEMPERATURE, °C

FIGURE 26. *Effect of testing temperature and the initial condition of the ingot iron on the strain at initial fracture.*

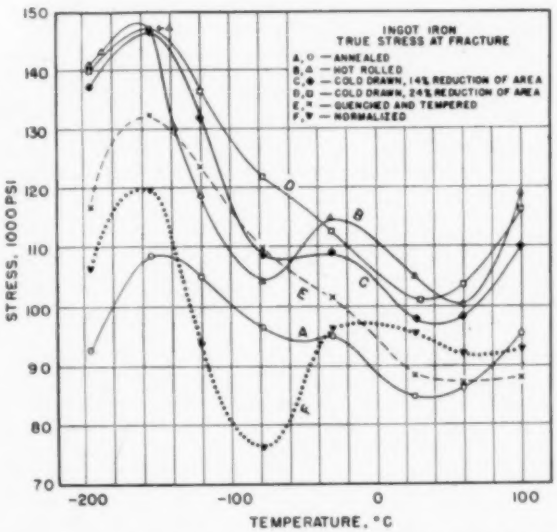
INGOT IRON
TRUE STRESS AT FRACTURE
A, ○ — ANNEALED
B, △ — HOT ROLLED
C, ◆ — COLD DRAWN, 14% REDUCTION OF AREA
D, □ — COLD DRAWN, 24% REDUCTION OF AREA
E, × — QUENCHED AND TEMPERED
F, ▼ — NORMALIZED
STRESS, 1000 PSI
TEMPERATURE, °C

FIGURE 27. *Effect of testing temperature and the initial condition of the ingot iron on the true stress at initial fracture.*

WASHINGTON, April 11, 1950.

Journal of Research of the National Bureau of Standards Vol. 45, No. 2, August 1950 Research Paper 2120

Effects of Pressure and Other Variables on Determinations of Octane Number [1]

By William J. Levedahl

Knock ratings made at altitude differ significantly from those made at sea level by both the ASTM Motor and Research Methods. Experiments were made in an altitude chamber to determine the effect on measured values of octane number of ambient pressure, engine speed, inlet mixture temperature, spark advance, knock intensity, exhaust back pressure, and diameter of carburetor venturi. The results indicate that no changes short of supercharging the engines will give ratings identical with those determined at sea level.

I. Introduction

After the adoption in 1933 of the ASTM Motor Method for determining the octane numbers of fuels, it was found that the ratings obtained by various laboratories differed somewhat, and that the differences increased with the altitudes of the test laboratories. In 1937, by throttling the intake and pumping down on the exhaust, Holaday and Moore [1] [2] showed that ratings decreased with decreasing charge density. They found that, at constant compression ratio, the knock intensity at 25 in. Hg with a ¾-in. venturi was equal to that at sea level with a 7/16-in. venturi and throttle plate. The subsequent use of larger venturis resulted in better agreement among ratings made at altitudes up to 5,000 ft.

The problem became more serious in 1939, when the Research Method was adopted by the Cooperative Fuel Research Committee as a supplementary method of rating fuels. Tests showed that neither changing the size of venturis nor varying the spark advance would compensate satisfactorily for altitude.

In 1941 this Bureau, in cooperation with the CFR Motor Fuels Division, conducted tests which indicated [2] that, with the fuels available at that time, the effect of altitude on knock ratings could be eliminated by operating at constant knock intensity. Blends of secondary reference fuels (A–6 and C–12) were used in this work.

A series of "guide curves" was established to indicate the proper compression ratios for maintaining standard knock intensity at all barometric pressures and octane numbers. These curves (one curve for each octane level) are parallel straight lines, one for each octane number, the slopes of which are 0.030 and 0.020 in./in. Hg for the Motor Method and for the Research Method, respectively. Application of this method in various laboratories gave ratings that were essentially independent of the altitude of the test engine.

With the development of the Detonation Meter, Model 501, as an alternate to the bouncing pin, a second set of guide curves was established at this Bureau in 1948 for use with the 7/16-in. venturi.

More recently, two developments have led to the belief that the empirical method outlined above is not wholly satisfactory in insuring uniformity of ratings. These are changes in the composition of motor gasoline due to the method of manufacture and the more general use of the primary reference fuels, *n*-heptane and isooctane, instead of secondary reference fuels. Current gasolines are more sensitive to engine operating conditions than earlier fuels, and hence show greater differences in ratings by the Motor and Research Methods. The secondary reference fuels behave similarly with respect to the primary reference fuels.

Hence the American Petroleum Institute and the National Bureau of Standards undertook a further investigation of the problem of altitude ratings in 1949. The objectives of the program were to establish the magnitudes of rating variation with pressure for several typical fuels, to check the guide curves, and to investigate the individual effects of certain operating variables.

II. Test Equipment

The engine used in this project was a standard ASTM-CFR knock rating engine [3], with a single cylinder of 3¼-in. bore and 4½-in. stroke. The compression ratio could be varied between 4:1 and 10:1 by raising or lowering the cylinder, and determined by means of a micrometer. All settings and operating conditions specified in reference [3] were followed, excepting only the cases for which deviations are specified herein. Both the bouncing pin and the alternate Model 501 Detonation Meter were used in the present work.

The air-consumption tests were made with a multiple-orifice air meter developed by the Ethyl Corporation. The test engine was installed in a conventional altitude chamber large enough to accommodate all equipment and two operators. A gate valve in the exhaust line was used to control exhaust back pressure in some tests. The coolant condenser was vented outside the chamber, so that the same boiling point prevailed at all altitudes. Chamber pressure was determined by subtracting the reading of a U-tube mercury manometer connected between the chamber and the atmosphere from the barometric

[1] This project was a joint undertaking of the American Petroleum Institute and the National Bureau of Standards.
[2] Figures in brackets indicate the literature references at the end of this paper.

pressure. A sensitive aircraft altimeter was then referred to as an aid in maintaining constant pressure.

III. Altitude Chamber Tests

1. Effect of Pressure on Octane Number Ratings

Standard procedures [3] were used throughout the tests unless otherwise noted. Prior to each series of runs at reduced pressure, the engine and knock detection apparatus were "standardized" with the chamber open. Subsequent tests were made at progressively lower pressures, keeping standard knock intensity by changing the compression ratio without further adjustment of the Detonation Meter or bouncing pin.

The ten fuels used were carefully selected so that the results would cover a wide range of fuel types and octane numbers. These are listed and numbered in table 1.

TABLE 1. *Fuels used in test program*

Fuel	Fuel composition	Nominal octane number	
		Motor Method	Research Method
1	60% X-6, 40% *n*-heptane	69.6	80.3
2	86% X-6, 14% *n*-heptane	90.0	>100
3	52% isooctane, 48% *n*-heptane, 2 ml TEL blend/gallon	75.6	74.7
4	74% isooctane, 26% *n*-heptane, 2 ml TEL blend/gallon	90.8	89.9
5	80 octane number commercial gasoline: catalytic cracked, thermal cracked, and straight-run components without lead	----	----
6	80 octane number commercial gasoline: catalytic cracked, thermal cracked, and straight-run components with lead	----	----
7	80% diisobutylene, 20% *n*-heptane	----	----
8	51% X-6, 49% *n*-heptane	60.8	69.9
9	70% X-6, 30% *n*-heptane	77.9	89.9
10	C-14 secondary reference fuel	70.0	72.4

The results obtained by the Motor Method, using test fuels 1 through 7 and both the bouncing pin and the Detonation Meter, are given in table 2 and shown graphically in figure 1. A carburetor venturi, 9/16 in. in diameter, was used at ambient pressures of 27 in. Hg and above, and a 3/4-in. venturi was used at lower pressures. Filled circles indicate results with the bouncing pin, and the open circles are for the Detonation Meter.

TABLE 2. *Variation of Motor Method ratings with pressure*

Chamber pressure	Venturi diameter	501 Detonation Meter		Bouncing pin	
		Rating octane No.	Micrometer	Rating octane No.	Micrometer
FUEL 1					
in. Hg	*in.*		*in.*		*in.*
29.68	9/16	70.1	0.510	----	----
29.64	9/16	----	----	69.4	0.527
29.0	9/16	70.8	.484	69.4	.509
28.0	9/16	70.0	.450	68.5	.479
27.0	9/16	69.2	.420	68.2	.449
26.0	3/4	68.9	.506	69.3	.499
25.0	3/4	68.6	.462	68.9	.472
23.0	3/4	68.0	.391	68.2	.398
21.0	3/4	----	----	67.8	.314

TABLE 2. *Variation of Motor Method ratings with pressure*—Continued

Chamber pressure	Venturi diameter	501 Detonation Meter		Bouncing pin	
		Rating octane No.	Micrometer	Rating octane No.	Micrometer
FUEL 2					
29.67	9/16	90.1	0.278	----	----
29.64	9/16	----	----	90.1	0.271
29.0	9/16	89.9	.260	89.7	.253
28.0	9/16	89.3	.220	89.3	.223
27.0	9/16	88.9	.200	88.4	.193
26.0	3/4	89.0	.275	89.4	.236
25.0	3/4	88.6	.250	89.2	.205
23.0	3/4	87.7	.191	88.1	.165
21.0	3/4	87.5	.137	86.6	.122
FUEL 3					
29.68	9/16	76.5	0.455	----	----
29.60	9/16	----	----	76.0	0.462
29.0	9/16	76.7	.437	75.8	.444
28.0	9/16	76.9	.407	76.4	.414
27.0	9/16	77.0	.357	76.7	.376
26.0	3/4	77.3	.442	77.1	.415
25.0	3/4	77.1	.402	77.1	.404
23.0	3/4	77.1	.324	77.5	.330
21.0	3/4	77.8	.228	77.5	.245
FUEL 4					
29.79	9/16	91.1	0.265	----	----
29.64	9/16	----	----	90.9	0.271
29.0	9/16	91.0	.244	90.7	.253
28.0	9/16	91.4	.214	90.9	.223
27.0	9/16	91.8	.184	91.7	.193
26.0	3/4	91.5	.233	91.0	.232
25.0	3/4	91.6	.214	91.0	.180
23.0	3/4	92.7	.140	92.1	.109
21.0	3/4	92.8	.080	92.8	.014
FUEL 5					
29.74	9/16	80.8	0.408	----	----
29.67	9/16	----	----	81.0	0.407
29.0	9/16	80.6	.387	81.2	.378
28.0	9/16	80.5	.350	80.6	.357
27.0	9/16	79.8	.314	80.1	.322
26.0	3/4	80.8	.375	81.4	.357
25.0	3/4	81.3	.329	80.9	.322
23.0	3/4	79.4	.264	80.3	.253
21.0	3/4	79.1	.194	78.7	.202
FUEL 6					
29.74	9/16	80.3	0.408	----	----
29.67	9/16	----	----	80.1	0.407
29.0	9/16	80.0	.387	79.9	.391
28.0	9/16	79.7	.350	79.7	.356
27.0	9/16	79.2	.314	79.3	.329
26.0	3/4	80.0	.377	80.7	.358
25.0	3/4	79.8	.336	80.6	.323
23.0	3/4	79.4	.250	80.0	.257
21.0	3/4	78.7	.194	78.7	.197
FUEL 7					
29.74	9/16	83.6	0.377	----	----
29.60	9/16	----	----	83.8	0.363
29.0	9/16	83.3	.356	83.6	.357
28.0	9/15	83.0	.317	83.4	.328
27.0	9/16	82.5	.285	83.2	.283
26.0	3/4	83.8	.329	85.1	.330
25.0	3/4	83.4	.300	84.2	.308
23.0	3/4	82.9	.228	83.5	.245
21.0	3/4	81.5	.175	81.6	.188

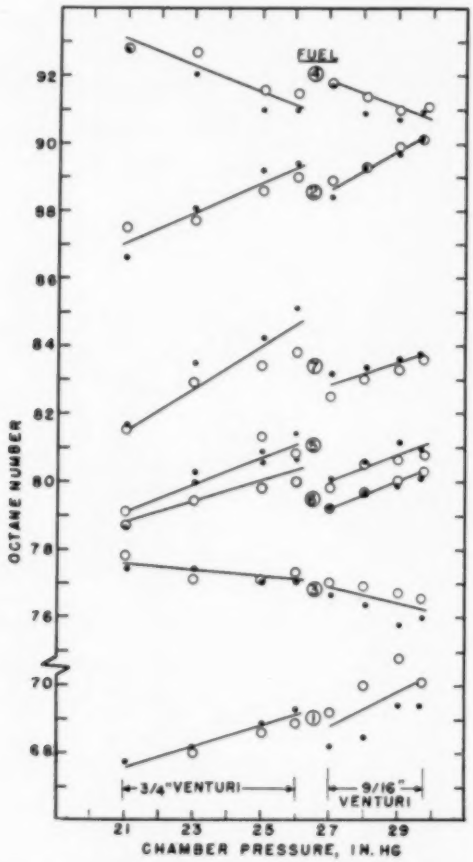

FIGURE 1. *Variation of octane rating with altitude by the ASTM D 357 Motor Method.*

For composition of the seven fuels, see table 1.
○, Rated with Detonation Meter, Model 501; ●, rated with bouncing pin.

As can be seen in figure 1, the octane number ratings of the leaded primary reference fuels (3 and 4) decrease with increasing pressure, whereas those of the other five fuels increase with the pressure. In most cases the rating at 26 in. Hg with the 3/4-in. venturi is approximately equal to the rating at one atmosphere with the 9/16-in. venturi.

Only the 9/16-in. venturi was used in the Research Method tests, and runs were made at sea level, 27, 24, and 21-in. Hg pressure. Fuels 3 and 5 were run only at sea level and 21-in. Hg. All fuel types tested by both methods showed the same trends by the Research Method as by the Motor Method. Secondary reference fuel C–14 increased in rating about 0.1 octane unit per inch of mercury pressure drop. Table 3 and figure 2 give the Research Method ratings at the various pressures for the fuels tested.

Constant knock intensity "guide curves" of micrometer setting versus barometric pressure were then determined for the Detonation Meter by both

TABLE 3. *Variation of Research Method ratings with pressure*

Chamber pressure	Rated with primary reference fuels				Rated with secondary reference fuels	
	501 Detonation Meter		Bouncing pin		501 Detonation Meter	
	Rating octane no.	Micrometer	Rating octane no.	Micrometer	Rating octane no.	Micrometer
	FUEL 3					
in. Hg		*in.*		*in.*		*in.*
29.64	74.5	0.415	------	------	------	------
21.0	76.6	.228	------	------	------	------
	FUEL 4					
29.67	91.1	0.282	------	------	------	------
29.62	------	------	91.2	0.270	------	------
29.74	------	------	------	------	91.3	0.288
27.0	91.6	.221	91.5	.238	91.6	.219
24.0	92.2	.144	91.8	.164	92.1	.145
21.0	92.3	.070	91.9	.096	92.3	.067
	FUEL 5					
29.64	91.5	0.274	------	------	------	------
21.0	89.9	.101	------	------	------	------
	FUEL 6					
29.66	89.9	0.292	90.7	0.290	89.9	0.300
27.0	89.5	.232	90.0	.235	89.7	.245
24.0	89.3	.168	89.2	.185	89.1	.175
21.0	88.5	.136	88.8	.115	88.7	.106
	FUEL 8					
29.72	70.2	0.434	------	------	------	------
29.63	------	------	------	------	70.7	0.426
29.62	------	------	70.4	0.442	------	------
27.0	69.4	.377	69.4	.392	70.4	.381
24.0	68.0	.283	68.8	.328	69.8	.324
21.0	67.6	.192	67.8	.256	69.1	.268
	FUEL 9					
29.67	90.2	0.292	------	------	------	------
29.66	------	------	90.4	0.290	------	------
29.74	------	------	------	------	90.7	0.294
27.0	89.9	.239	89.7	.235	90.2	.238
24.0	88.9	.172	88.6	.180	88.8	.178
21.0	87.4	.070	87.3	.129	87.6	.110
	FUEL 10					
29.64	72.3	0.424	------	------	------	------
27.0	72.5	.362	------	------	------	------
24.0	71.7	.308	------	------	------	------
21.0	71.4	.258	------	------	------	------

the Motor and Research Methods (figs. 3 and 4, tables 4 and 5). These curves show the cylinder height necessary to maintain standard knock intensity (a reading of 55 on the knockmeter) with primary reference fuel blends of 40 to 100 octane number.

The solid lines on the figures show the values obtained in these tests, while the dotted lines are those defined in reference [3]. Since no Detonation Meter guide curves have been adopted for use with the ¾-in. venturi, the dotted lines here show the bouncing pin curves.

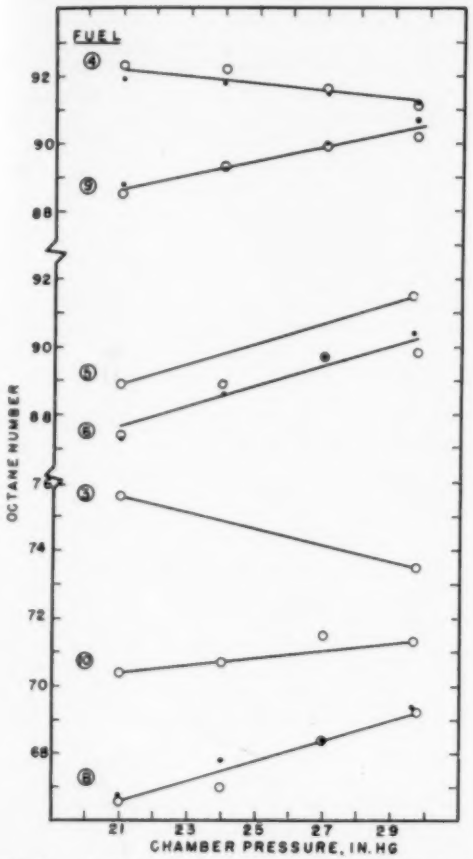

FIGURE 2. *Variation of octane rating with altitude by the ASTM D 908 Research Method.*

For composition of the seven fuels, see table 1.
○, Rated with Detonation Meter, Model 501; ●, rated with bouncing pin.

TABLE 4. *Motor Method guide curves for various pressures with the Detonation Meter, Model 501*

Octane number	Chamber pressure, in. Hg					
	9/16-in. venturi			3/4-in. venturi		
	29.68	28.5	27.5	27.0	24.0	21.0
	Micrometer setting					
	in.	*in.*	*in.*	*in.*	*in.*	*in.*
40	0.669	0.632	0.604	0.708	0.592	0.457
50	.625	.595	.569	.666	.550	.432
60	.578	.545	.512	.613	.503	.390
70	.518	.488	.453	.552	.447	.326
80	.425	.390	.350	.467	.361	.240
90	.299	.273	.235	.365	.251	.156
100	.202	.184	.157	.272	.173	.083

These results indicate that standard guide curves do not have sufficient slope, particularly at the lower octane levels. No conclusions should be drawn relative to the guide curve spacing for the Motor Method, as the customary practice of changing the Detonation Meter setting at the higher octane levels was not adhered to in these tests.

TABLE 5. *Research Method guide curves for various pressures with Detonation Meter, Model 501*

Octane number	Chamber pressure, in. Hg (9/16-in. venturi)			
	•29.66	27.0	24.0	21.0
	Micrometer setting			
	in.	*in.*	*in.*	*in.*
40	0.554	0.480	0.395	0.315
50	.522	.445	.367	.290
60	.483	.411	.337	.258
70	.436	.367	.295	.219
80	.375	.315	.239	.164
90	.292	.233	.164	.080
100	.155	.094	.026	−.049

•Pressure for fuels of 80, 90, and 100 octane number was 29.64 in. Hg.

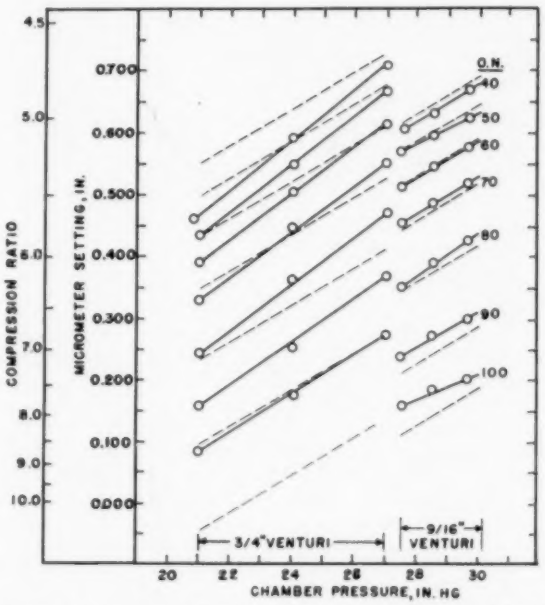

FIGURE 3. *Motor Method guide curves for various altitudes with Detonation Meter, Model 501.*

The solid lines represent data obtained in this research; the broken lines are the guide curves currently in use [3].

2. Effects of Pressure on Air Consumption (Motoring [3] Only)

It was thought that failure to obtain the same ratings at all altitudes might result primarily from the differences in air consumption. Therefore, air consumption while motoring was measured under both Motor and Research Method conditions at pressures down to 21 in. Hg. The effects of oversized ... 'uris, a high-lift camshaft, and change in exhau... back pressure were also determined. The high-lift camshaft used had an inlet cam that increased the

[3] "Motoring" designates nonfiring operation of the engine.

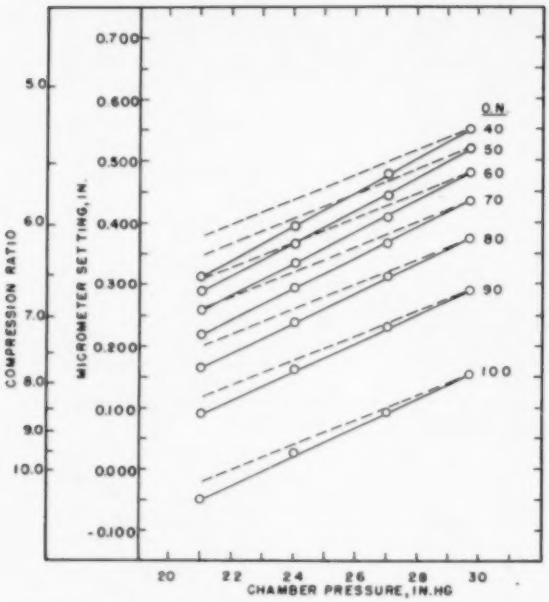

FIGURE 4. *Research Method guide curves for various altitudes with Detonation Meter, Model 501.*

The solid lines represent data obtained in this research; the broken lines are the guide curves currently in use [3].

maximum travel of the valve and caused it to remain open for 45° instead of 34° of the compression stroke. Compression pressures were also recorded.

Under both standard conditions, air consumption decreased slightly faster than the chamber pressure. Increasing the venturi diameter from $\frac{5}{16}$ in. to $\frac{3}{4}$ in. produced a 10-percent increase in volumetric efficiency for the Motor Method, but only about 3 percent for the Research Method. This was the equivalent of restoring sea-level air consumption at 27 in. and 29 in. Hg in the two methods, respectively. The high-lift camshaft made no improvement under Motor Method conditions and caused a slight decrease in Research Method volumetric efficiency. An Aviation Method curved inlet elbow also proved to be of no value for this purpose. An increase in exhaust back pressure decreased air consumption. Compression pressure was always proportional to air consumption when no excess back pressure was used.

3. Individual Effects of Engine Operating Variables

In these experiments the engine was run with all operating conditions standard except that being investigated.

(a) Exhaust Back Pressure

An increase of 9-in.-Hg exhaust back pressure caused an apparent increase of about one octane unit in the Motor Method rating, while in the Research Method, rating was decreased approximately the same amount. Engine operation was extremely rough and erratic.

(b) Engine Speed

In order to determine the effect of engine speed on octane number ratings, the engine was run under standard Motor Method conditions, except that its speed was reduced from 900 to 600 rpm. Fuels 1, 4, 5, 6, and 7 were rated at 21 in. Hg, and in all cases it was necessary to decrease the compression ratio below that specified in the Motor Method guide curves in order to keep the detonation down to standard knock intensity.

All fuels except No. 4 showed an average increase in rating of about 6 octane units. Fuel 4 showed a decrease in rating of 2.4 octane units. Reducing the engine speed by 300 rpm has a greater effect on the rating than does a decrease in pressure of 9 in. Hg. However, the magnitude of the effect of speed varies greatly from fuel to fuel so that no single change in speed could be expected to have the same compensating effects for all fuels.

(c) Inlet Temperature

The effect of lowering intake gas temperature in 25° F increments was measured for the Motor Method. Fuels 2, 4, and 6 were run with the ¾-in. venturi at 21 in. Hg. Fuels 2 and 6 rated about one octane unit higher for every 25-deg drop in manifold temperature. The rating of fuel 4 changed in the opposite direction by about one octane unit for every 50-deg drop in temperature.

No experiments were made with lower inlet temperature for the Research Method because the standard temperature of 125° F is considered to be just adequate for vaporization of a 400° F end-point gasoline [4].

(d) Ignition Timing

The effect of spark advance on Research Method ratings was determined at 21 in. Hg for fuels 4, 8, and 9. Results indicate that a change in timing cannot cause any significant increase in ratings at low pressures.

(e) Knock Intensity

The next independent variable to be tried was knock intensity. At 21 in. Hg, fuels 4 and 8 were rated by the Research Method at standard micrometer settings and at setting 0.045 in. and 0.090 in. below the guide curve. The higher compression ratios gave much higher knock intensities, which lowered the rating of fuel 4 by about one octane unit and increased that of fuel 8 by about 0.2 unit.

(f) Bouncing Pin Setting Adjustment

Attempts were made to restore Research Method octane number ratings at 24 in. Hg of fuels 4, 5, 6, 7, and 8 to their sea-level values by adjusting the bouncing pin. No consistent improvement seems possible by use of this technique.

IV. Conclusions

All of the fuels tested in this program changed in octane rating as the pressure of the altitude chamber was decreased. In general, the fuels that were the most sensitive to altitude changes were those with the highest sensitivity to engine severity, as defined by the differences between their Motor Method and Research Method ratings. This is to be expected, as the higher compression ratios used at lower chamber pressures increase the engine severity by raising the compression temperatures.

It has been shown that decreased inlet temperature and decreased speed shift altitude ratings by the Motor Method toward their sea-level values, but at different rates for various fuels. Although the effects of spark advance on this method were not investigated, a change in this factor might prove advantageous. Larger carburetor venturis have proved useful, and permit ratings to be maintained at about their sea-level values up to altitudes to 3,000 to 4,000 ft. It is possible that the Motor Method ratings are capable of being equalized throughout the altitude range by use of a suitable combination of changed conditions.

The Research Method, on the other hand, does not lend itself well to modifications of this type. The spark advance is already nearly the optimum, inlet temperature is at about the minimum that will assure adequate vaporization of the fuel, the volumetric efficiency is improved very little by use of a larger venturi, and the engine speed is already very low.

It appears, therefore, that the surest way of making the engine severity equal to that at sea level, regardless of the altitude, is to supercharge the inlet and throttle the exhaust, thereby simulating sea-level conditions. For this purpose, a small single-stage centrifugal compressor would probably suffice. The air would enter the blower through a standard humidity-controlling ice tower, and thence through the standard air heater to a pressurized carburetor. It is possible that an after-cooler may also be necessary to keep the inlet temperature below 125° F in the Research Method at the lower chamber pressures.

This investigation was carried out in cooperation with the Octane Correlation Advisory Committee of the Division of Refining of the American Petroleum Institute. Members of this committee are: Bruno R. Siegel, chairman, Frank C. Burk, Carl E. Habermann, J. E. Taylor; associate members are Harold M. Trimble, H. R. Stacey, John M. Snell, Afton D. Puckett, and Hudson W. Kellogg. Appreciation is expressed to the committee members for planning the scope of the work and their expert advice in carrying it out. Credit is also due the following for their work in operating the engines and altitude equipment: W. C. Lacey, Myron C. Wolfe, James O. Chase, H. B. Dickerson, J. M. Mealing, L. J. Wilson, H. S. Simmons, Fred W. Ramin, George J. Miner, Edwin H. Rich, Richard M. David, James A. Walker, Milford Barnes, Thomas W. Mears, and Mrs. Cecil S. Dussinger.

V. References

[1] W. M. Holaday and G. T. Moore, Effect of altitude on octane number determination, presented at SAE Annual Meeting, January 1937.

[2] D. B. Brooks, Effect of altitude on knock rating in CFR engines, J. Research NBS **28,** 713 (1942) RP1475.

[3] ASTM manual of engine test methods for rating fuels and 1948 appendix (American Society for Testing Materials, 1916 Race Street, Philadelphia 3, Pa.).

[4] O. C. Bridgeman, Equilibrium volatility of motor fuels from the standpoint of their use in internal combustion engines, J. Research NBS **13,** 53 (1934) RP694.

WASHINGTON, April 10, 1950.

Journal of Research of the National Bureau of Standards Vol. 45, No. 2, August 1950 Research Paper 2121

Creep of High-Purity Copper

By William D. Jenkins and Thomas G. Digges

Creep tests were made at 110°, 250°, and 300° F on annealed oxygen-free high-conductivity copper. The rate of loading to the ultimate had a significant effect on the amount of plastic extension and thereby affected the creep behavior. The strain rate during the so-called second stage of approximately constant rate was not constant but varied in a cyclic manner. A less-pronounced cyclic variation was also evident in both the first and third stages. The beginning of the third stage was often accompanied by microcracking, but in other tests this stage was initiated without the presence of such cracks. The parent grains were fragmented during creep, and strain markings were observed in all specimens carried to complete fracture.

I. Introduction

Creep tests in tension were made on annealed oxygen-free high-conductivity copper as a part of a continuing investigation at this Bureau on the creep of metals and alloys. Additional tests at elevated and subzero temperatures on this copper and other materials are in progress. In a previous paper [1][1] it was shown that the flow, ultimate and fracture

[1] Figures in brackets indicate the literature references at the end of this paper.

stresses, and ductility increased with a decrease in test temperature and with an increase in strain rate of another lot of oxygen-free high-conductivity copper initially cold-rolled 75-percent reduction in area.

Parker and Riisness [2] reported that the creep strength at 200° C of annealed oxygen-free high-conductivity copper was independent of the grain size. Parker [3] also determined the stress-rupture properties at 200° C of this type of copper initially in the conditions as (1) annealed, (2) cooled in air, and (3) quenched in water from 850° C. The strength and ductility of the quenched specimens were appreciably lower than those of the specimens as annealed or as cooled in air. A linear relation was shown in a log-log plot of the experimental values of the stress versus the time to rupture for both the annealed and air-cooled conditions, but there were points at which changes occurred in the slope of the curve for the initially quenched specimens. Some recrystallization occurred in specimens, which were cold-rolled from 1.0 to 0.1 in. in thickness, after heating at 200° C for 20 hr.

Davis [4] made a study of the creep and relaxation (constant deformation) at temperatures up to 235° C of oxygen-free copper initially extended 8 percent in tension, and he attempted to correlate the results of the two different types of tests by using various theories of plastic deformation. At 235° C, the creep (extension-time) curves tended to become straight after about 400 hr, but at 165° C they did not become straight until after about 1,200 hr; at 30° C, the curves had not reached a constant slope after 3,500 hr. The stresses used in these creep tests ranged from 12,000 to 16,000 psi at 30° C, 4,000 to 10,000 psi at 165° C, and 2,500 to 7,000 psi at 235° C. The logarithms of minimum creep rates for all the tests, except those at 30° C, were plotted against the stress, and straight lines were drawn to fit these data (semilog plot). He concluded that the hyperbolic-sine relation between the minimum creep rate and stress fitted the test data very well. No accurate theory existed by which the shape of the relaxation curve could be predicted from data observed in creep tests when the temperatures were within the range covered in these tests. The strain rate in the latter stages of a relaxation test was slower than the minimum creep rate for the corresponding stress.

Burghoff and Blank [5] presented data on creep at 300°, 400°, and 500° F of four types of wrought copper and several copper alloys initially as annealed and as cold-drawn. Usually, their creep tests did not progress beyond the first stage (that of decreasing rate under constant load) within a period of about 6,000 hr; the values reported for creep rate were those obtained in the latter part of the test. A linear relationship was shown in a log-log plot of the experimental values of stress versus strain rate for oxygen-free copper (99.98 percent copper) initially both as annealed (0.025-mm grain diameter) and as cold-drawn 84 percent. The cold-drawn specimens became about half recrystallized during the course of the tests at 300° F and completely recrystallized at 400° F shortly after the creep load was applied.

Schwope, Smith, and Jackson [6] recently investigated the effect of cold work on the short-time creep strength in tension and compression at 570° F and on the long-time creep strength in tension at lower temperatures (200° to 300° F) of several types of commercial copper, including the oxygen-free high-conductivity grade. They reported that cold work increases the creep strength of copper, but its beneficial effect is lost at temperatures where recrystallization was rapid. The trends in the short-time creep tests were also evident in the longer time creep tests. A linear relation was shown in plots of stress versus log of strain rate of the experimental values for both the short- and long-time tests.

II. Material and Testing Procedures

All specimens were cut from a bright annealed $1\frac{3}{16}$-in. round bar of oxygen-free high-conductivity copper (OFHC) containing 99.99+ percent of copper as determined by chemical analysis. The arc spectrum of the copper was examined for the sensitive lines of Ag, Al, B, Be, Co, Fe, In, Ir, Mg, Mo, Na, Ni, Pb, Sb, Si, Sn, Ti, V, and Zn. The lines for Ag, Al, Mg, and Si were identified, and there was some indication of the presence of Fe, Ni, and Pb.

Some properties at room temperature of the annealed copper were as follows:

Average grain diameter, mm	0.025
Average hardness, Rockwell F	34
Tensile strength, 1,000 psi	31.9
Yield strength, (0.2 percent offset) 1,000 psi	12.2
Elongation in 2 in., percent at maximum load	39
Elongation in 2 in., percent at fracture	51
Reduction of area, percent at maximum load	28
Reduction of area, percent at fracture	88

The creep tests were made on specimens having a 0.505-in. gage diameter and a gage length of 2 in.; all specimens were prepared from the same bar. The tests were carried out in a noncontrolled atmosphere (air) at temperatures of 110°, 250°, and 300° F. The temperatures of the creep furnaces were controlled within the range of about ±1 deg F of the desired temperature (temperature differences within the gage length of the test specimen were less than 3 deg F), and the probable error of extension measurements was less than 0.00002 in. The specimens were held for a minimum of 48 hr at temperature before loading, and the rate of loading of each specimen to the selected ultimate[2] stress was accurately controlled. Each creep test was made at a constant load, which was maintained for the complete test. A rate of loading of 3,200 psi/hr (3,200 psi applied at 1-hr intervals) was selected as a

[2] The terms "ultimate stress" are used to designate the selected stress applied to a specimen for testing in creep at a constant load. The value for ultimate stress is obtained by dividing the load by the original area of the specimen.

"standard," and this rate was used in all tests except those in which the rate of loading was varied to determine its effect on creep behavior. When the ultimate stress (nominal) [3] was not divisible by 3,200, the remainder was added as the final step.

The equipment used for creep testing is essentially the same as that used and described in previous investigations [7]; some improvements have been made, especially in temperature controllers, measuring microscopes, and method of attaching the strips to specimens for measuring the extension.

Rockwell F hardness (60-kg load, 1/16-in.-diameter ball) measurements were made on the bar as annealed and on selected specimens after testing either in creep or in normal tension at room temperature. Two flats 180° apart were prepared parallel to the longitudinal axis of the specimens tested to fracture in tension, and the Rockwell readings were made at room temperature on various points along the center line of these flats. The diameters of the specimens at the points of indentation were accurately determined by means of a measuring microscope. Thus, the hardness values could be correlated with the degree of plastic deformation.

Usual procedures were followed in preparing specimens by mechanical methods for metallography and in carrying out the metallographic examinations.

[3] The nominal stress is defined as the stress obtained by dividing the current load by the original area of the specimen. The true stress is defined as the stress obtained by dividing the current load by the current minimum area of the specimen.

TABLE 1. *Summary of conditions used and results of creep and tension tests on high-purity copper initially as bright annealed*

Thermal mechanical history	Temperature	Ultimate stress	Loading schedule	Creep rate	Time	Plastic extension	Beginning of third stage			End of test				Remarks
							Time	Plastic extension	True stress	Time	Plastic extension	Reduction of area	True stress	
	°F	1,000 lb/in.²		%/1,000 hr	hr	% in 2 in.	hr	% in 2 in.	1,000 lb/in.²	hr	% in 2 in.	%	1,000 lb/in.²	
Initially as annealed	80	31.9		60,000			0.7	39.	44.0	1.25	51.0	88	140.0	Tested to fracture.
Do	70	31.8		60,000			.7	38.5	44.0	1.20	62.0	78	80	Test stopped before complete fracture.
Average		31.8		60,000			.7	38.8	44.0					
Initially as annealed	110	25.6	3,200 psi/hr.	1.08	500 to 900	18.57 to 19.0				943	19.0	16.0	30.5	Test stopped in second stage.
Extended 9.5% at 250° F. with ultimate of 16,000 psi. Temperature changed to 110° F. at 4,062 hr.	110	25.6	Load added in increments of 1,600 or 3,200 psi Loading time at 110° F., 1,076 hr.	1.88	500 to 900	23.65 to 24.4				1,680	25.6	20.4	32.2	Do.
Initially as annealed	110	28.8	3,200 psi/hr.	165	24.5 to 105	28.8 to 42.2	105	42.2	40.9	123	62.5	90	278.6	Tested to complete fracture.
Extended 9.5% at 250° F. with ultimate of 16,000 psi. Temperature changed to 110° F. at 4,062 hr.	110	28.8	Load added in increments of 1,600 or 3,200 psi. Loading time at 110° F., 2,756 hr.	2,100	1.2 to 3.03	37.7 to 41.9	3.03	41.9	40.7	5	68.5	86.2	208.6	Do.
Initially as annealed	250	16.0	3,200 psi/hr.	0.44	1103 to 2472	8.34 to 8.94				2,472	8.94	8.19	17.4	Test stopped in second stage.
Do	250	16.0	Applied instantaneously.	0.43	1103 to 2472	8.43 to 9.01				2,472	9.01	8.34	17.5	Do.
Do	250	19.2	3,200 psi/hr.	14.3 1.6 1.51 1.43 1.04	23 to 123 791 to 1679 700 to 2200 1679 to 2541 2500 to 5000	10.9 to 12.6 15.1 to 16.5 14.9 to 17.2 16.5 to 17.7 17.6 to 20.2								Test still in progress.
Do	250	19.2	3,200 psi/wk.	1.77 1.55	774 to 1677 1677 to 2541	15.1 to 16.7 16.7 to 18.0				2,541	18.0	15.3	22.7	Test stopped in second stage.
Extended 8.94% at 250° F. with ultimate of 16,000 psi for 2,472 hr.	250	19.2	3,200 psi applied instantaneously.	1.67	789 to 1679	15.05 to 16.54				1,679	16.54	14.2	22.4	Do.
Extended 9% in tensile test at 80° F.	250	19.2	3,200 psi/hr.	1.15	700 to 2200	10.9 to 12.6				2,700	16.0	11.5	21.7	Do.
Initially as annealed	250	22.4	3,200 psi/hr.	10.1	312 to 1248	25.5 to 35.7	1,248	35.7	30.0	1,824	48.9	34.3	34.1	Test stopped in 3d stage before complete fracture.
Extended 18% at 250° F. in 3,381 hr. with ultimate of 19,200 psi.	250	22.4	3,200 psi added instantaneously.	37.8	170 to 369	32.1 to 39.6	369	39.6	31.4	483	47.3	40.5	37.6	Do.
Initially as annealed	250	24.0	3,200 psi/hr.	130	31 to 134	27.9 to 41.2	134	41.2	33.9	168	59.4	78.7	112.4	Tested to complete fracture.
Do	300	19.2	3,200 psi/hr.	8.3	200 to 990	18.9 to 25.4	990	25.4	24.1	1,522	36.5	33	28.8	Do.
Extended 16.5% at 250° F. in 4,050 hr. with ultimates of 16,000 and 19,200 psi.	300	19.2	Temperature change only, with load on specimen.	8.3	330 to 835	21.2 to 25.4	835	25.4	24.1	1,332	36.5	33	28.8	Do.
Initially as annealed	300	20.8	3,200 psi/hr.	36.4	80 to 335	22.1 to 31.4	335	31.4	27.5	439	46	46.7	39	Do.

III. Results and Discussion

1. Influence of Temperature, Stress, and Rate of Loading on Plastic Extension in First Stage of Creep

The experimental results are summarized in table 1 and figures 1 to 27. The influence of temperature on the stress-strain relationship of the initially annealed copper is shown by a comparison of the relative positions of the curves in figure 1. Except for the specimen extended at 80° F (room temperature) at a rate of 6×10^4 percent/1,000 hr, each specimen was loaded in increments of 3,200 psi applied hourly (hereafter designated as "standard" rate of loading), and the values plotted for extension are those obtained after the application of the loads for a period of 1 hr. Obviously, the resistance to flow decreased as the test temperature was increased. The relatively high resistance to flow of the specimen at 80° F was due partially to the higher strain rate used; an increase in strain rate and decrease in test temperature both tend to increase the rate of work hardening.

Stresses of 3,200 and 6,400 psi produced only small amounts of plastic extension in 1 hr in specimens at 110°, 250°, or 300° F. With the application of higher stresses at each of these temperatures, however, the specimens continued to extend during the 1 hr they were subjected to the constant stress (creep usually occurred at a decreasing rate), as is illustrated by the typical curves given in figure 2 for a specimen tested at 300° F.

The stress-strain curve, for a specimen initially extended 9 percent in tension at room temperature before heating at 250° F for 48 hr and then loaded at the standard rate to an ultimate of 19,200 psi, is given in figure 3. The resistance to plastic deformation at 250° F was materially increased by the cold-working at room temperature. Although the increase in plastic extension at 250° F was less than 0.3 percent after the application of the stress of 19,200 psi for 1 hr, the shape of the curve shows that relatively rapid increases in extension occurred with the application both of the initial and final stresses. The rapid increase in deformation with the application of only 3,200 psi indicates that the internal stress induced by cold-working was considerably relieved during the period of heating at 250° F before applying this stress; the rapid increase in extension with the application of a stress of 19,200 psi may be attributed to a change in grain orientation.

The effect of variations in the rate of loading on the plastic extension at 250° F is shown by the results summarized in figure 4. The experimental points as plotted in this figure are based on the extension produced after the different loads were applied for a period of 1 hr and also at the end of the period of creep when the specimens were allowed to remain under constant loads for periods in excess of 1 hr. At a stress of 16,000 psi, the plastic extension increased somewhat with change in rate of loading from instantaneous [4] to increments of 3,200 psi/hr (standard), but the elongation obtained with the standard rate was the same as that of a specimen loaded at a considerably slower rate in increments of 3,200 psi/week. However, the paths of the stress-strain curves of the specimens loaded at the standard (3,200 psi/hr) and slow rates (3,200 psi/week) were not alike. In the early stages of loading, the curve for the specimen loaded relatively slowly was at a higher level (value for extension after load was applied for 1 hr) than that of the curve of the specimens loaded at the standard rate; the stress-strain curves as reproduced for these two specimens either coincide or cross at several points due to the change in plastic extension with increase in time from 1 hr to 1 week at a constant load. At a stress of 19,200 psi, the plastic extension (after 1 hr) of the specimen loaded at the relatively slow rate was greater than that of the specimens loaded at the standard rate, and it was less than that of a specimen loaded at the standard rate to 16,000 psi, allowed to creep at this load for an appreciable time (2,472 hrs) before increasing the stress to 19,200 psi.

The stress-strain curve for a specimen at 110° F, which was loaded at the standard rate, and the curve for another specimen at 250° F on which a stress of 16,000 psi was applied instantaneously are given in figure 5. The stress of 16,000 psi remained on the specimen at 250° F for 4,062 hr (extension of 9.5 percent) before reducing the test temperature to 110° F (load not changed); the test was then continued for 236 hr at 110° F (less than 0.1-percent increase in extension) before increasing the stress to 28,800 psi in increments of either 1,600 or 3,200 psi and allowing to creep at each load for the time as given on the curve. The latter curve falls appreciably below the former curve, especially in the region corresponding to the higher range in stress. Thus the rate of loading to the ultimate and the thermal history had a marked effect on the amount of plastic extension, and this in turn affected the creep rates in the first, second, and third stages, the duration of these stages, and ductility at fracture (table 1).

The results presented in a previous investigation [8] also showed that the creep behavior of initially cold-drawn ingot iron was affected by the rate of loading to the ultimate. The creep rate in the second stage and elongation at fracture both decreased with a decrease in rate of loading in the first stage.

2. Influence of Prior Thermal-Mechanical History on Creep Behavior

A summary of the extension-time curves for the various conditions investigated is given in figure 6, and the influence of prior strain history on creep behavior is shown by a comparison of these curves and those reproduced in figures 7, 8, 9, and 10.

At an ultimate stress of 19,200 psi (fig. 7), the

[4] The term "instantaneous" is used to designate the rate of loading in which the load was applied gradually over a period of about 30 sec.

general trend was for the creep rate at 250° F to decrease as the rate of attaining the initial extension of about 9 percent was increased. That is, for the same time or strain interval (table 1), the slowest average creep rate during the second stage occurred in the specimen initially extended about 9 percent at room temperature, intermediate in the specimen loaded at the standard rate and extended at 250° F, and next fastest in the specimen allowed to creep 8.9 percent at 250° F (stress of 16,000 psi) before applying a stress of 19,200 psi. The fastest creep rate occurred in the specimen loaded 3,200 psi/week. At 300° F, the average creep rates in the second stage and the extensions both at the beginning of the third stage and at complete fracture were alike for specimens either loaded slowly (allowed to creep at 250° F before increasing the test temperature) or at the standard rate, but the total time required to reach the third stage and fracture was greater for the specimen loaded at the standard (faster) rate.

At an ultimate stress of 22,400 psi (fig. 8), the average creep rate in the second stage at 250° F of the specimen loaded at the standard rate was only about one-quarter of that of another specimen allowed to extend approximately 18 percent at 250° F before applying the ultimate load; the difference in plastic extension at the start of the third stage in the two specimens is partly due to the difference in strain rates in the second stage.

At an ultimate stress of 25,600 psi (fig. 9), the average creep rate in the second stage at 110° F of the specimen loaded at the standard rate was considerably slower than that of the specimen loaded relatively slowly (extended about 9.5 percent in 4,062 hr at 250° F with load of 16,000 psi before decreasing temperature to 110° F and then increasing the load to 25,600 psi in 1,076 hr).

At an ultimate stress of 28,800 psi (fig. 10) the average creep rate in the second stage at 110° F of the specimen loaded at the standard rate (relatively fast) was considerably less than that of another specimen allowed to creep at 250° F and at 110° F with lower stresses before applying the ultimate.

The extension-time curve for a specimen tested at 250° F with an ultimate stress of 22,400 psi into the third stage of creep is reproduced in figure 11. The curve as plotted is typical of the idealized creep in tension (constant load and temperature) in that it consists of an initial extension (about 15 percent) and stages of primary, secondary, and tertiary creep, respectively; the test was discontinued before complete fracture. However, the strain rate during the so-called second stage of approximately constant rate was not constant but varied in a cyclic manner over an appreciable range as is illustrated by the course of the creep rate-time curve given in the upper part of the figure. Even in the primary (creep at a decelerating rate) and tertiary stages (creep at accelerating rate leading to fracture) the change in strain rate with time did not always occur uniformly (continuous decrease or increase, respectively) but often varied in cycles or showed discontinuities in each of these two stages.

Although some irregularities were observed in the creep rate-time relation in each specimen of high-purity copper as tested in tension in creep, the test conditions and prior mechanical history affected the amplitude and frequency of the cycles or discontinuities. For example, the cycles are quite prominent in both the first and second stages for the test conditions as given in figure 9. Cycling is not evident in the first stage in the creep rate-time curve for the specimen tested at an average creep rate of 165 percent per 1,000 hr (fig. 10), or in the third stage of another specimen tested at a creep rate of 2,100 percent per 1,000 hr. The two specimens differed in strain history, which affected the creep rates. It should be pointed out that some cycling or irregularity did occur for each of these conditions, however, the cycling trend is not manifested in the curves until the time coordinate is expanded considerably over that used in figure 10. The phenomenon as observed in the first, second, and third stages is not a direct result of the increase in true stress with increase in plastic deformation during the course of the test as is illustrated for the first and second stages in figure 9.

The effects of test temperature and stress on the cycling of strain rate in the first stage of creep of initially annealed specimens are shown by a comparison of the curves in figure 12. The trend was for the cycling in this stage to decrease in amplitude with increase in both stress and temperature.

As is illustrated in figure 13, the observed trend was for the amplitude of the creep rate-plastic extension cycles in the second stage to decrease with an increase in both the strain rate (constant temperature) and the temperature (constant strain rate). A significant feature is that at a constant temperature, the beginning of this prominent cycling effect was shifted to lower strain values as the ultimate stress was decreased. Furthermore, the amount of plastic extension at the beginning of the second stage of creep decreased with a decrease in ultimate stress. Irregularities are also shown in the creep rate during the first and third stages. However, these irregularities were less prominent in the third than in the first stage and considerably less prominent in both than in the second stage of creep.

The described discontinuities and cycling conditions in the creep rate-time curves are believed to be due to changes in the degrees of slip and the accompanying work hardening and recovery.

Cycling in extension-time curves was also observed and reported in a previous study of the creep characteristics of cold-drawn ingot iron [8].

Any adequate physical theory of the mechanism of the deformation of high-purity copper by creep in tension must account for this variation in strain rate with time or plastic extension.

3. Influence of Prior Strain History on Recovery Characteristics

Carreker, Leschen, and Lubahn [9] investigated the effect of changing stress on strain rate at room temperature of annealed specimens of oxygen-free

high-conductivity copper and high-purity lead wires. A discontinuous change in the strain rate followed by a gradual approach to a steady state value was produced in polycrystalline aggregates of each material when the applied stress was suddenly changed from one to another constant value.

Part of an extension-time curve for a specimen tested at 250° F with an ultimate stress of 16,000 psi is given in figure 14. After the specimen was allowed to extend to about 9.0 percent, the load was removed in increments of 3,200 psi/hr, and when completely unloaded (temperature not changed), it was allowed to rest for 33 hr before starting reloading at the standard rate to an ultimate of 16,000 psi. The specimen was allowed to creep under this stress for an additional period of about 600 hr when the stress was momentarily increased (position *D* on curve); thereafter the specimen continued to creep under the original load. Although the specimen contracted plastically about 0.07 percent during the cycle of unloading and reloading, and extended plastically about 0.06 percent as a result of the momentary increase in stress, the average creep rate in the second stage was not significantly affected by these changes. However, as illustrated by the course of the creep rate-time curve, the amplitude of the cycles increased with these two changes in the testing procedure.

The change in total extension (elastic and plastic) with time as the above specimen was unloaded in steps of 3,200 psi at an interval of 1 hr is shown in figure 15. Although the frequency of the measurements of extension was necessarily decreased in the late stage of each period of 1 hr, the curves as constructed to represent the experimental values show definite trends that are believed to be characteristic. Cycling is evident in each curve except for the condition of zero stress. These cycles are more prominent in the early than in the latter part of the periods after the application of stresses of 12,800 psi, 9,600 psi, or 3,200 psi, and their magnitude appears to decrease with a decrease in stress. Although the specimen contracted after the removal of the loads to attain the stresses of 12,800, 9,600, and 6,400 psi, a noteworthy feature is that the extension increased (not decreased) immediately after the time required to make the initial readings. However, no change in extension was detected immediately after making the initial reading on reducing the stress to 3,200 psi, and at zero load the specimen contracted rapidly for about one-quarter hour, and thereafter, even for a period of 33 hr, its extension was practically unchanged.

The change in total extension of the above specimen after 1 hr under each constant load during unloading and reloading is shown in figure 16. Similar curves are also reproduced for unloading two other specimens at 250° F at the same rate (3,200 psi/hr) from an ultimate of 19,200 psi. As is shown by the difference in slope of the curves, the prior strain history of the specimens affected the degree of recovery at 250° F during unloading; the decrease in total extension for the three specimens at zero load ranged from about 0.2 percent for the specimen unloaded from 16,000 psi to about 0.3 percent for the two specimens unloaded from 19,200 psi.

4. Influence of Temperature and Stress on the Average Creep Rate in the Second Stage

The relation between nominal stress and average creep rate in the second stage of specimens tested at different temperatures is shown in figure 17. At 250° F, the experimental values do not fall on a straight line in either a semilog or log-log plot. The course of the stress-strain rate curve was not definitely established at 110° or 300° F as only two creep tests were made at each of these temperatures. However, these results show that the resistance to creep of the initially annealed copper increased with a decrease in test temperature.

5. Variation of Ductility with Temperature and Creep Rate

In the creep tests in which the specimens were loaded at the standard rate the initial extension, intercept, extension at the start of the third stage, extension at fracture, and reduction of area at fracture (fig. 18) each increased with an increase in strain rate (constant temperature) and tended to decrease with an increase in temperature (constant strain rate). It should be pointed out, however, the extension at fracture of the specimen tested in creep at 110° and 250° F was greater than that of the specimens fractured at room temperature in the ordinary tension test (table 1). The true stress at complete fracture of the specimen tested at 110° F (strain rate of 165 percent per 1,000 hr) was also considerably greater than that of the specimens fractured at room temperature. This increase is believed to be due in part to the higher strain rate just prior to complete fracture of the specimen tested in creep.

6. Influence of Prior Thermal Mechanical History on Room Temperature Tensile and Hardness Values

The effect of plastic extension in creep at 110° and 250° F on the flow characteristics at 80° F (room temperature) is shown in figure 19. The true stress-strain curves at 80° F (based on total deformation) for the specimens initially as annealed or extended into the second stage of creep at rates of about 1.1 percent per 1,000 hr are nearly alike over the range in true stress of 40,000 to 70,000 psi. That is, the combined effect of creep, work-hardening, and recovery at 110° or 250° F is not manifested in the shape of the flow curves in this range of stress. The true stress-strain curve at 80° F of the specimen extends into the third stage of creep at 250° F (49% extension at a rate of 10%/1,000 hr) falls appreciably below the corresponding curve of the annealed material. The lowering of the flow curve for this specimen previously extended in creep can be attributed to its relatively high degree of recovery and

possibly to the presence of cracks of submicroscopic dimensions at the completion of the creep test (fig. 23, D and E).

In all cases, the values at maximum load for plastic extension, reduction of area, and true stress were less in the annealed specimen than the corresponding values of the specimens previously extended in creep. However, the values for reduction of area and true stress at both the beginning of and at complete fracture were less for each of the specimens previously extended in creep at 250° F than those of the annealed specimens or the specimens extended in creep at 110° F.

The change in hardness at room temperature with plastic extension (reduction of area) of specimens tested to complete fracture in creep at different temperatures and rates, and in tension at room temperature, is given in figure 20. The hardness of the initially annealed specimens (R_f=34) increased markedly with increase in plastic deformation to the third stage of creep (20 to 30 percent reduction of area, table 1); thereafter the induced hardness varied with the amount of deformation, temperature of deformation, and strain rate. Of the two specimens tested at 300° F, the induced hardness was somewhat greater and the peak in the hardness-reduction of area curve occurred at a greater amount of extension in the specimen tested at the higher strain rate in the second stage. In both specimens, the value for hardness in the vicinity of the fracture was less than that at some lower value of extension. The curves for the specimen tested in ordinary tension at 70°, and in creep at 110° and 250° F, were quite similar in that none showed a definite break or peak (that is, the maximum hardness is in vicinity of fracture), and the maximum hardness value attained in each was greater than that of the specimens tested in creep at 300° F. In the plastic range beyond the beginning of the third stage, however, the curve for the specimen tested at 250° F is below the curves of the specimens at 80° and 110° F.

7. Changes in Microstructure and Fracture Characteristics as Affected by Temperature and Strain Rate

For the specimens tested to complete fracture in creep, the propensity to necking (fig. 21) and to transcrystalline fracture (fig. 22) increased with increase in strain rate and decrease in temperature. At sufficiently high strain rates and low temperatures, considerable necking occurred (fig. 21, *A*, *B*, and *C*) and the fractures were essentially transcrystalline (fig. 22, *B*, *C*, and *D*), but with relatively slow strain rates and high temperatures no appreciable necking occurred (fig. 21, D, E, and F) and the fractures were predominantly intercrystalline (fig. 22, *E* and *F*). In the specimens that fractured in a transcrystalline manner (fig. 22, *B* and *C*), cracking was confined principally to the region of complete fracture, whereas in the specimens that fractured in an intercrystalline manner (fig. 22, *E* and *F*) numerous cracks (general disintegration) were observed in regions remote from complete fracture; some cracks of microscopic dimensions were observed about 0.05 in. from the position of complete fracture of a specimen in which the fracture appeared to be partly intercrystalline but predominantly transcrystalline (fig. 22, *D*).

The tendency for a specimen to disintegrate as plastic deformation by creep proceeds to intercrystalline rupture is illustrated by a comparison of typical photomicrographs of figures 22, *F*, and 23, *A* and *B*. Appreciable cracking is evident even at a deformation corresponding to the beginning of the third stage of creep (fig. 23, *B*) in a specimen tested at 300° F to complete rupture. Similar conditions were observed in another specimen fractured in creep at the same temperature (300° F) and strain rate (8.3%/1,000 hr) but with an entirely different strain history. Furthermore, cracking at deformations corresponding to the beginning of the third stage of creep was detected in two other specimens tested at a lower temperature (250° F) and different strain rates (fig. 23, *C* and *D*). The creep tests of the latter two specimens were terminated during the third stage before complete fracture, but one specimen was subsequently fractured at 80° F.

Only a few cracks of microscopic size were observed at a deformation corresponding to the beginning of the third stage in the specimen extended in creep at 250° F and finally fractured at 80° F (fig. 23, *D*). Although these cracks were located principally in the interior of the specimen in the vicinity of its axis, a few cracks were also located at the surface (fig. 23, *E*). The surface cracks (not detected at a magnification of about 25 diameters) were invisible at the end of the creep test. As previously shown (fig. 19), the true stress-strain curve at 80° F of this specimen was materially lowered by extending in creep, and this decrease in resistance to flow might be partly due to the presence of submicroscopic cracks at the termination of the creep test.

It is evident, therefore, that under certain conditions the third stage of creep can be accompanied by cracking, but other evidence (fig. 22, *C*) shows that cracks of microscopic dimensions are not a prerequisite for the initiation of the third stage of creep in high-purity copper.

Baeyertz, Craig, and Bumps [10] reported the presence of discontinuous cracks in steel fractured by impact, and Jaffee, Reed, and Mann [11] also found discontinuous cracks adjacent to the path of final brittle failure in both fatigue and impact specimens made from steel forgings and castings. Tipper [12] observed microcracks near the fracture of mild steel plates. Jaffee and coauthors [11] were of the opinion that brittle transgranular fracture of polycrystalline metal does not originate at one point and propagate continuously across the material, but rather nucleate at numerous related points, leading to a series of microcracks that link up subsequently.

In some cases, cracking leading eventually to complete fracture was initiated at the axis of specimens tested in tension, whereas in other specimens cracking was initiated at the surface. As is illustrated in figure 24 and 25, the position (interior or exterior of the specimen) where cracking was initiated and the

course of the propagation of these cracks depended upon the test conditions, such as strain rate and temperature. In a specimen extended in ordinary tension at 80° F until the true stress-strain curve indicated the beginning of fracture (fig. 24, *A*), cracking started at or near the axis of the necked section (fig. 24, *B*), and had the specimen been carried to complete rupture these discontinuous cracks (fig. 25, *A*) would have linked up as they propagated transcrystallinely outward to the surface (fig. 22, *B*); no cracking was visible at the surface of the neck section of this specimen (fig. 25, *B*). In such failures, appreciable necking occurs and the "so-called breaking or fracture stress" is usually considerably higher than the true-fracture stress (fig. 19) due to the "rim effect."

Microcracking was confined to the immediate vicinity of complete fracture of another specimen, which was extended 9 percent in tension at 80° F prior to testing into the second stage of creep at 250° F (additional extension of 7%) and finally fracturing at 80° F (fig. 23, *F*). As considerable necking with its accompanying rim occurred and the fracture was transcrystalline, it is believed that cracking was initiated near the axis of the specimen and not at its surface. That is, the creep test was carried out under conditions that did not nucleate at the surface a crack that subsequently propagated across the entire specimen. However, in a specimen extended at 250° F at creep rates of about 1.5 and 37.8 percent per 1,000 hr (to extension of 18 and 47%, respectively), cracking was initiated at the surface (figs. 24, *C, D;* 25, *C, D, E*), but evidently cracking subsequently commenced in the interior (fig. 25, *F*); the numerous small cracks observed in the interior after a light etch (not clearly shown in fig. 25, *F*) appear to have originated principally at the grain boundaries. In such failures, only a small amount of necking occurs, and the path of the fracture is predominantly intercrystalline.

Wilms and Wood [13] described a mechanism by which metals deform at normal and elevated temperatures. At normal temperatures, deformation occurs mainly by the mechanism of slip and the break-down of the grains to crystallites of submicroscopic size. As the temperature is raised and the rate of deformation is diminished, this mechanism is increasingly replaced by one in which the grains dissociate into comparatively coarse units and permit flow by the relative movement of these units within the parent grain. The units, which are termed "cells", can be observed and measured. They are considered to be responsible for the continuous deformation under stress, which characterizes the phenomenon of creep.

Some changes in structural features accompanying plastic deformation of high-purity copper in ordinary tension and in creep at different temperatures are shown in figures 26 and 27. A lineage structure is evident in the equiaxed grains in the initially annealed specimen (fig. 26, *A*). These grains were elongated in the direction of the applied stress during the process of deforming in tension, and the degree of distortion in this direction depended upon the amount of plastic extension, strain rate, and temperature. Relatively high strain rates and low temperatures both favored this condition, and the elongation of the grains usually attained a maximum at or in the vicinity of complete fracture. The breakdown of the original grains as plastic deformation proceeds is also evident by the presence of a substructure that appears to be numerous crystals of microscopic dimensions within certain of the parent grains. Although the number and size of these subcrystals appear to be affected by the amount of plastic extension and test conditions, they were observed in specimens tested under a wide range of conditions (compare fig. 26, *B*, and fig. 27, *B*). The general trend was for the size of the subcrystals to increase with increase in test temperature and decrease in strain rate.

In a study of the changes in microstructure of single and polycrystalline aluminum plastically deformed at different temperatures and strain rates, Hanson and Wheeler [14] observed slip bands (specimen polished prior to deforming) on the surface of single crystals at all temperatures and strain rates used. With polycrystalline specimens, the slip bands without marked changes at the grain boundaries, were observed when the specimens were strained at relatively high rates and low temperature (ordinary tension at room temperature) but were not visible in the specimens tested in creep at relatively slow rates and high temperature. In the latter specimens that did not exhibit slip bands, marked localized deformation occurred at or near the grain boundaries, and fracture was intercrystalline without necking.

Strain markings were quite prominent in all of the copper specimens carried to complete fracture, regardless of the testing conditions used (figs. 26 and 27). The markings in some of the parent grains have the appearance of twins, even in the vicinity of incipient cracking, as is illustrated in figure 27, *A*, for a specimen extended at the highest temperature used (300° F) with a strain rate of only 36.4 percent per 1,000 hr.

IV. Summary

Creep tests in tension were made at various temperatures and strain rates on initially bright annealed oxygen-free high-conductivity (OFHC) copper. The testing program included a study of the influence of thermal and strain history, rate of loading to the ultimate, sudden change in stress from one to another constant value, and change in test temperature on creep behavior and plastic deformation. Metallographic examinations and hardness measurements were carried out at room temperature on specimens representative of the copper before and after testing in creep. In addition, tensile tests provided data on true-stress-strain relations at room temperature on specimens as annealed or as previously extended at elevated temperatures into the second or third stage of creep.

The prior thermal and strain history and rate of loading to the ultimate affected markedly the amount

of plastic deformation and creep behavior. The general trend was for the degree of plastic deformation and creep rate in the second stage to decrease as the rate of loading was increased.

The strain rate during the second stage of creep was not constant but varied with time in a cyclic manner. The trend was for the amplitude of these cycles to decrease with increase in both stress and temperature.

In some cases, the beginning of the third stage of creep was accompanied by cracks of microscopic dimensions, but the presence of such cracks are not a prerequisite for the initiation of the third stage of creep in high-purity copper.

The positions at which cracks were nucleated and the course of their propagation were affected by the test conditions. Cracking started at or near the axis of the specimen tested in ordinary tension at room temperature. These discontinuous cracks united as they propagated transcrystallinely outward toward the surface, and appreciable necking occurred in the specimen before complete rupture. Cracking started at the surface of a specimen tested into the third stage of creep at 250° F, but at a later stage numerous small cracks were also nucleated in its interior, principally in the parent grain boundaries. Complete rupture occurred in this specimen without appreciable necking and the fracture was predominantly intercrystalline.

The degree of necking, ductility at the beginning of the third stage and at complete rupture, and the propensity to transcrystalline fracture of the specimens tested in creep increased with an increase in strain rate (temperature constant) and with a decrease in temperature (strain rate constant).

Metallographic examination showed the breakdown of the original grains of the copper that occurred with plastic deformation under a wide range of test conditions. Strain markings were also observed in all specimens that were carried to complete rupture. Some of these markings had the appearance of twins.

The authors are indebted to J. H. Darr, C. R. Johnson, and F. A. Wilkinson for assistance in making many of the measurements of creep.

V. References

[1] D. J. McAdam, Jr., G. W. Geil, and D. H. Woodard, Influence of strain rate and temperature on the mechanical properties of Monel metal and copper, Proc. Am. Soc. Testing Materials **46,** 902 (1946).

[2] E. R. Parker and C. F. Riisness, Effect of grain size and bar diameter on creep rate of copper at 200° C, Metals Tech. **11,** TP 1690 (Feb. 1944); Trans. Am Inst. Mining Met. Engrs. (Inst. of Metals Div.) **156,** 117 (1944).

[3] E. R. Parker, The effect of impurities on some high temperature properties of copper, Trans. Am. Soc. Metals **29,** 269 (1941).

[4] E. A. Davis, Creep and relaxation of oxygen-free copper, Trans. Am. Soc. Mech. Engrs. **65,** [A] 101 (1943).

[5] H. L. Burghoff and A. I. Blank, The creep characteristics of copper and some copper alloys at 300, 400, and 500° F, Proc. Am. Soc. Testing Materials **47,** 725 (1947)

[6] A. D. Schwope, K. F. Smith, and L. R. Jackson, The comparative creep properties of several types of commercial coppers, J. Metals **1,** (July 1949); Metals Trans. **185,** 409 (1950).

[7] J. A. Bennett and D. J. McAdam, Jr., Creep rates of cold-drawn nickel-copper alloy (Monel metal), J. Research NBS **28,** 417 (1942) RP1462.

[8] W. D. Jenkins and T. G. Digges, Influence of strain rate and temperature on the creep of cold-drawn ingot iron, J. Research NBS **43,** 117 (1949) RP2013.

[9] R. P. Carreker, J. G. Leschen and J. D. Lubahn, Transient plastic deformation, Trans. AIME (Inst. of Met. Div.) **180,** 139 (1949); Metals Tech. **15** (Sept. 1948) TP2477.

[10] M. Baeyertz, W. F. Craig, Jr., and E. S. Bumps, A metallographic description of fracture in impact specimens of a structural steel, J. Metals **1** (August 1949); Metals Trans. **185,** 481 (1950).

[11] L. D. Jaffe, E. L. Reed, and H. C. Mann, Discontinuous crack propagation—Further studies, J. Metals **1** (Oct. 1949); Metals Trans. **185,** 683 (1950).

[12] C. F. Tipper, Brittle fracture in mild-steel plates II, Engineering **165,** 594 (1948).

[13] G. R. Wilms and W. A. Wood, Mechanism of creep in metals, J. Inst. Metals **75,** 693 (1949).

[14] D. Hanson and M. A. Wheeler, The deformation of metals under prolonged loading. I—The flow and fracture of aluminium, J. Inst. Metals Proc. **45,** 229 (1931).

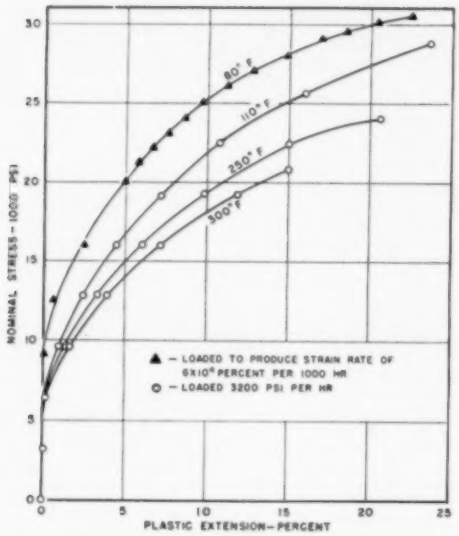
NOMINAL STRESS - 1000 PSI
PLASTIC EXTENSION-PERCENT
80° F
110° F
250° F
300° F
▲ - LOADED TO PRODUCE STRAIN RATE OF 6X10⁻⁴ PERCENT PER 1000 HR
○ - LOADED 3200 PSI PER HR

FIGURE 1. *Effect of nominal stress on plastic extension at different temperatures.*

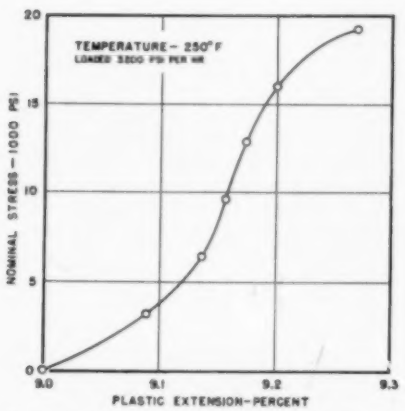

FIGURE 3. *Effect of nominal stress on plastic extension at 250° F.*

The specimen was initially extended 9 percent in tension at 80° F. The values for extension are those obtained 1 hour after the application of the loads.

FIGURE 5. *Effect of rate of loading and prior thermal-mechanical history on plastic extension at 110° F.*

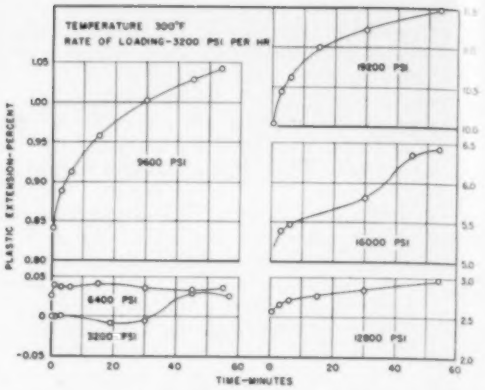

FIGURE 2. *Variation in plastic extension with time at 300° F with different nominal stresses.*

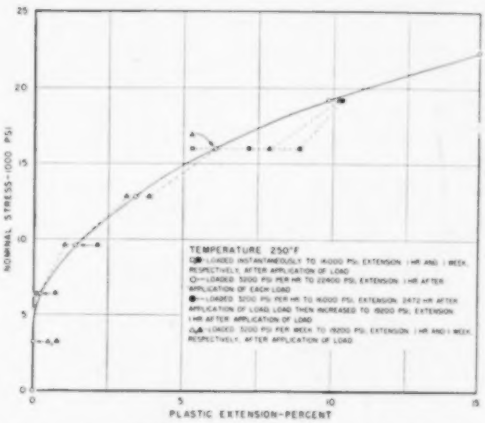

FIGURE 4. *Effect of rate of loading on plastic extension at 250° F.*

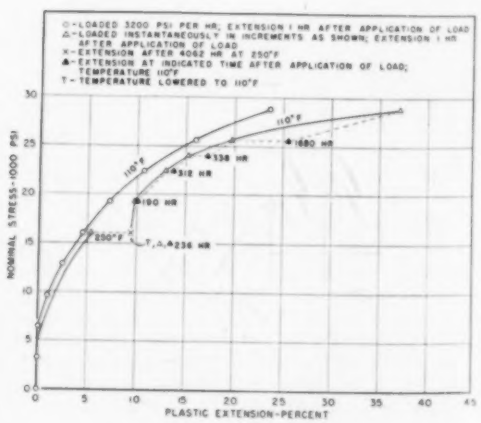

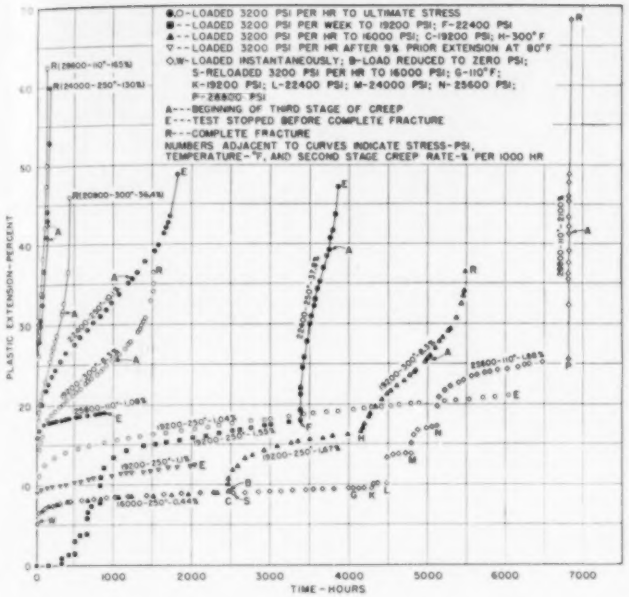

FIGURE 6. *Summary of extension-time curves for specimens tested in creep under the various conditions used.*

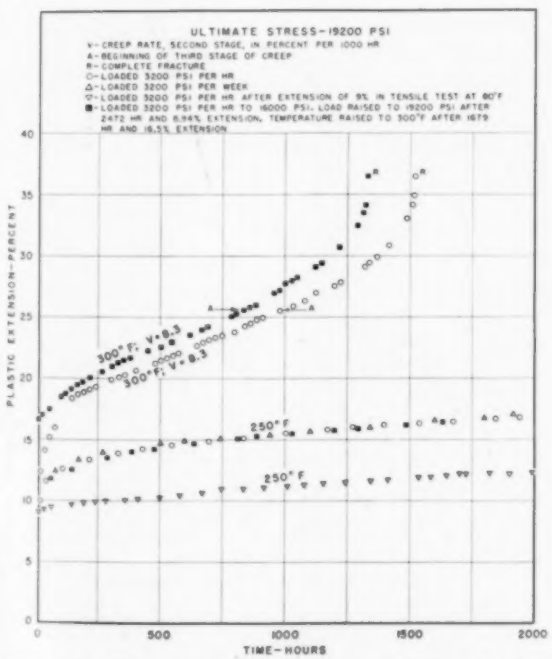

FIGURE 7. *Effect of rate of loading on creep at 250° and 300° F.*

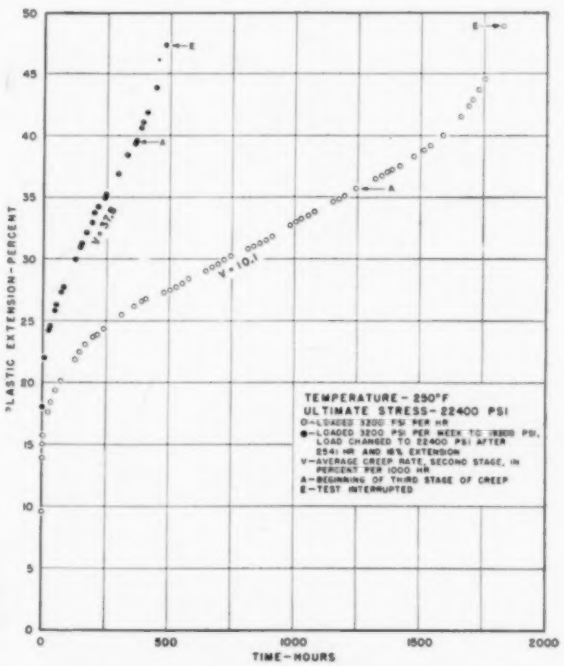

FIGURE 8. *Effect of rate of loading on creep at 250° F.*

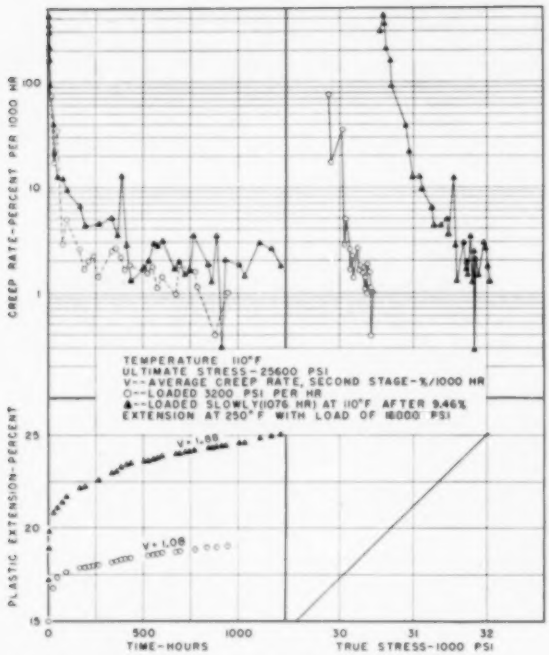
CREEP RATE-PERCENT PER 1000 HR
PLASTIC EXTENSION-PERCENT
TEMPERATURE 110°F
ULTIMATE STRESS-25600 PSI
V--AVERAGE CREEP RATE, SECOND STAGE-%/1000 HR
O--LOADED 3200 PSI PER HR
▲--LOADED SLOWLY(1076 HR) AT 110°F AFTER 9.46% EXTENSION AT 250°F WITH LOAD OF 18000 PSI
V=1.88
V=1.08
TIME-HOURS
TRUE STRESS-1000 PSI

FIGURE 9. *Effect of rate of loading on creep at 110° F.*

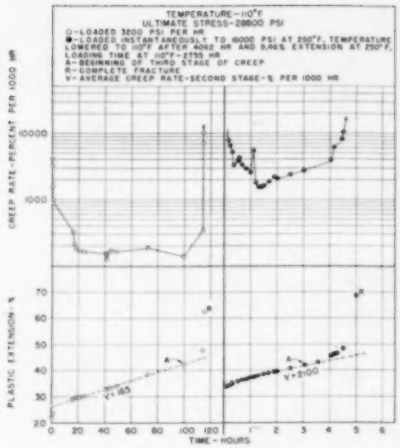
TEMPERATURE-110°F
ULTIMATE STRESS-28800 PSI
O-LOADED 3200 PSI PER HR
●-LOADED INSTANTANEOUSLY TO 16000 PSI AT 250°F, TEMPERATURE LOWERED TO 110°F AFTER 4062 HR AND 5.46% EXTENSION AT 250°F, LOADING TIME AT 110°F-2755 HR
A-BEGINNING OF THIRD STAGE OF CREEP
R-COMPLETE FRACTURE
V-AVERAGE CREEP RATE-SECOND STAGE-% PER 1000 HR
CREEP RATE-PERCENT PER 1000 HR
PLASTIC EXTENSION-%
V=.165
V=2100
TIME-HOURS

FIGURE 10. *Effect of rate of loading on creep at 110° F.*

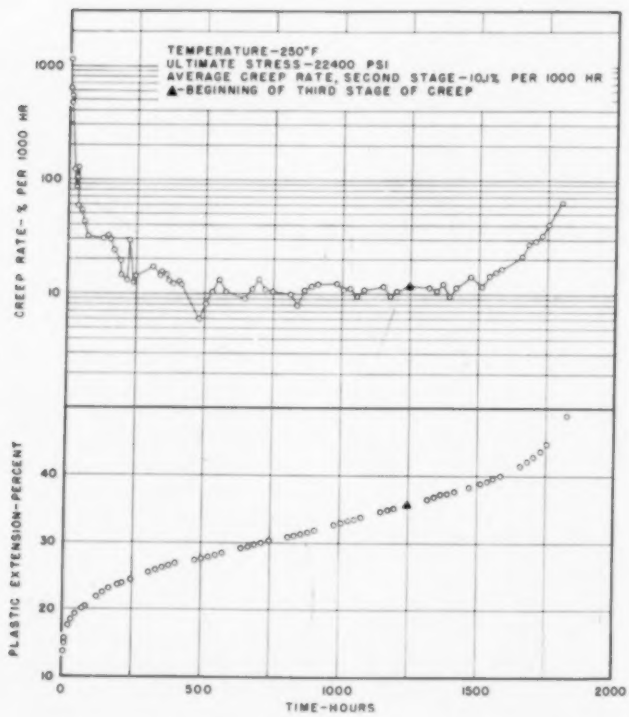

FIGURE 11. *Extension-time and creep rate-time relations for a specimen tested at 250° F with a nominal stress of 22,400 psi.*

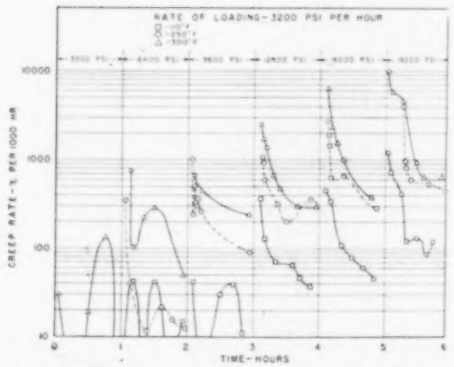

FIGURE 12. *Variation in creep rate in the first stage with time at different temperatures and with different nominal stresses.*

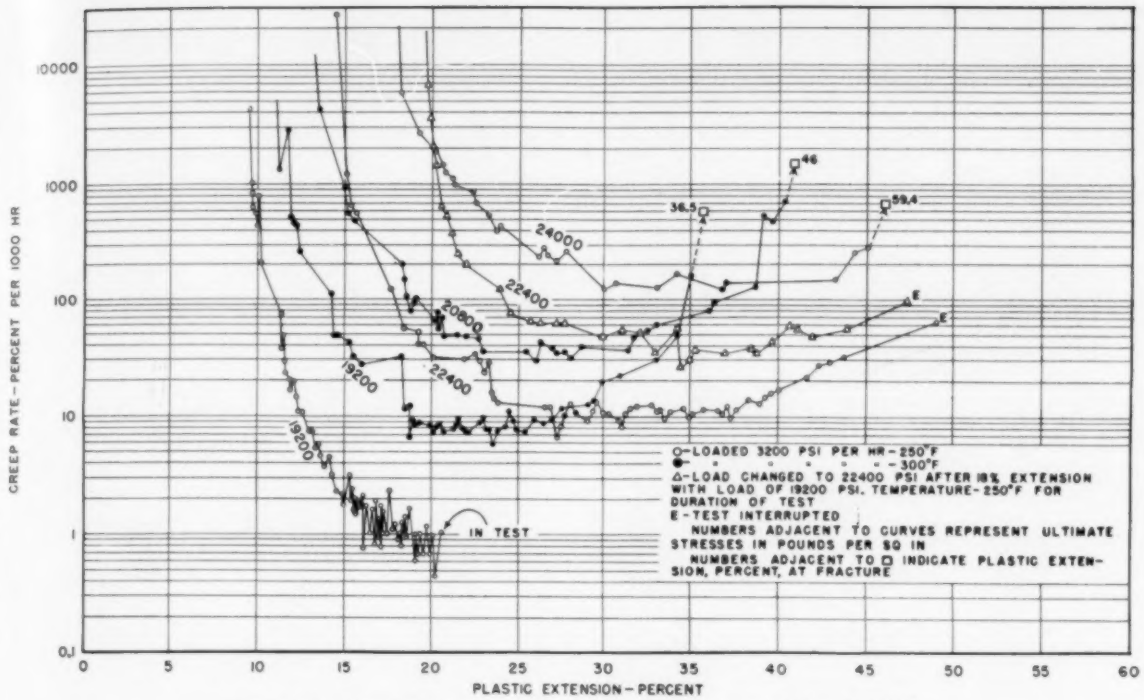
CREEP RATE – PERCENT PER 1000 HR
PLASTIC EXTENSION – PERCENT
24000
22400
20800
19200
22400
19200
IN TEST
36.5
46
59.4
E
E
○–LOADED 3200 PSI PER HR – 250°F
●– " " " " – 300°F
△–LOAD CHANGED TO 22400 PSI AFTER 18% EXTENSION WITH LOAD OF 19200 PSI. TEMPERATURE – 250°F FOR DURATION OF TEST
E–TEST INTERRUPTED
NUMBERS ADJACENT TO CURVES REPRESENT ULTIMATE STRESSES IN POUNDS PER SQ IN
NUMBERS ADJACENT TO □ INDICATE PLASTIC EXTENSION, PERCENT, AT FRACTURE

FIGURE 13. *Variation in creep rate with plastic extension at 250° and 300° F.*

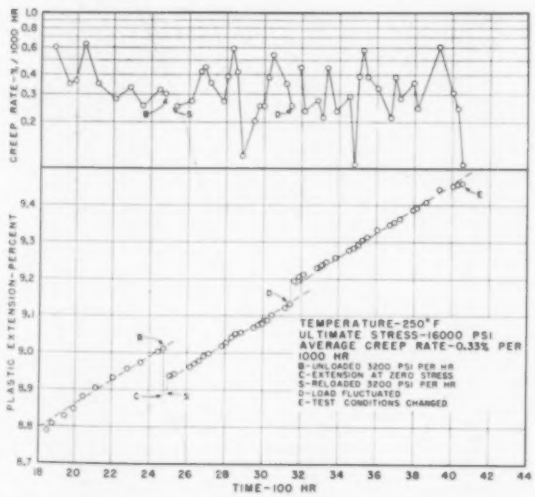
CREEP RATE – % / 1000 HR
PLASTIC EXTENSION – PERCENT
TIME – 100 HR
TEMPERATURE – 250° F
ULTIMATE STRESS – 16000 PSI
AVERAGE CREEP RATE – 0.33% PER 1000 HR
B–UNLOADED 3200 PSI PER HR
C–EXTENSION AT ZERO STRESS
S–RELOADED 3200 PSI PER HR
D–LOAD FLUCTUATED
E–TEST CONDITIONS CHANGED

FIGURE 14. *Variations in plastic extension and creep rate with time at 250° F.*

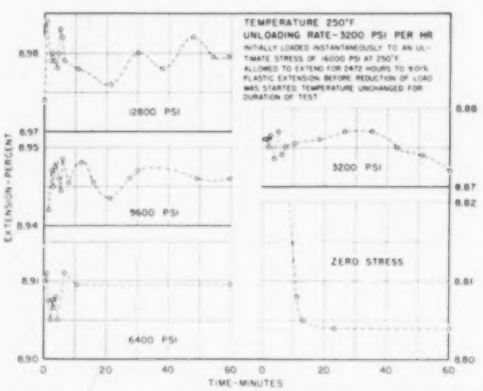
TEMPERATURE 250°F
UNLOADING RATE – 3200 PSI PER HR
INITIALLY LOADED INSTANTANEOUSLY TO AN ULTIMATE STRESS OF 16000 PSI AT 250°F
ALLOWED TO EXTEND FOR 2472 HOURS TO 9.0% PLASTIC EXTENSION BEFORE REDUCTION OF LOAD WAS STARTED. TEMPERATURE UNCHANGED FOR DURATION OF TEST
12800 PSI
9600 PSI
6400 PSI
3200 PSI
ZERO STRESS
EXTENSION – PERCENT
TIME – MINUTES

FIGURE 15. *Change in extension with time at 250° F of a specimen unloaded from 16,000 psi.*

Some creep characteristics of this specimen before and after unloading and reloading are given in figure 14.

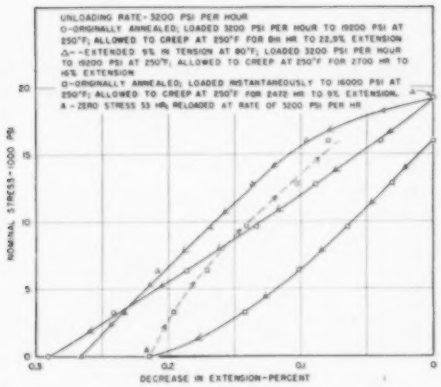
UNLOADING RATE - 3200 PSI PER HOUR
O - ORIGINALLY ANNEALED; LOADED 3200 PSI PER HOUR TO 19200 PSI AT 250°F; ALLOWED TO CREEP AT 250°F FOR 84 HR TO 22.9% EXTENSION
Δ - - EXTENDED 9% IN TENSION AT 80°F; LOADED 3200 PSI PER HOUR TO 19200 PSI AT 250°F, ALLOWED TO CREEP AT 250°F FOR 2700 HR TO 16% EXTENSION
O - ORIGINALLY ANNEALED; LOADED INSTANTANEOUSLY TO 16000 PSI AT 250°F; ALLOWED TO CREEP AT 250°F FOR 2472 HR TO 5% EXTENSION.
A - ZERO STRESS 53 HR, RELOADED AT RATE OF 3200 PSI PER HR
NOMINAL STRESS - 1000 PSI
DECREASE IN EXTENSION - PERCENT

FIGURE 16. *Change in total extension at 250° F during unloading specimens initially at stresses of 16,000 or 19,200 psi.*

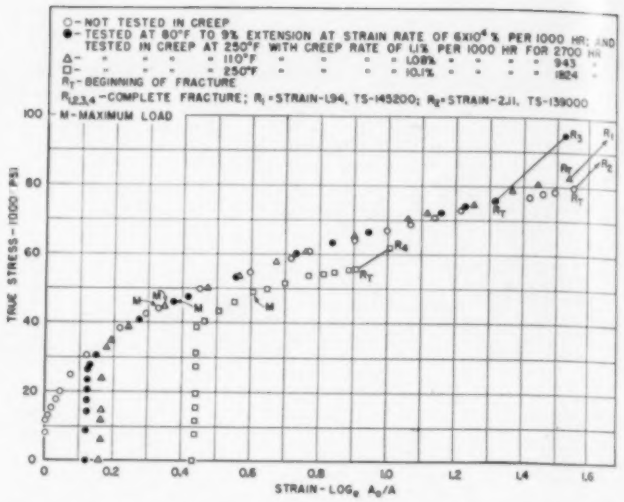
○ - NOT TESTED IN CREEP
● - TESTED AT 80°F TO 9% EXTENSION AT STRAIN RATE OF 6X10⁻⁴ % PER 1000 HR; AND TESTED IN CREEP AT 250°F WITH CREEP RATE OF 1.1% PER 1000 HR FOR 2700 HR
Δ - " " " " 110°F " " " 1.08% " " " 943 "
□ - " " " " 250°F " " " 10.1% " " " 1824 "
R_T - BEGINNING OF FRACTURE
R_1,2,3,4 - COMPLETE FRACTURE; R_1 = STRAIN-1.94, TS-145200; R_2 = STRAIN-2.11, TS-139000
M - MAXIMUM LOAD
TRUE STRESS - (1000 PSI)
STRAIN - LOG_e A_o/A

FIGURE 19. *Effect of extending in creep at different temperatures on the tensile properties at room temperature of initially annealed copper.*

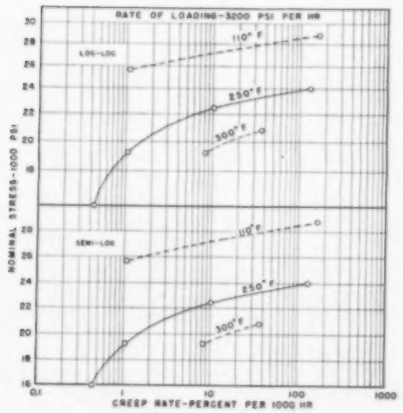

FIGURE 17. *Relation between nominal stress and creep rate at different temperatures.*

The creep rate is the average value obtained during the second stage.

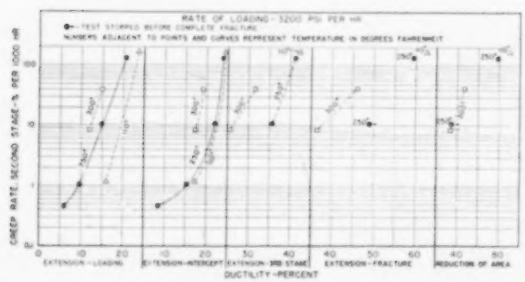
RATE OF LOADING - 3200 PSI PER HR
CREEP RATE, SECOND STAGE - % PER 1000 HR
EXTENSION - LOADING
EXTENSION - INTERCEPT
EXTENSION - 3RD STAGE
EXTENSION - FRACTURE
REDUCTION OF AREA
DUCTILITY - PERCENT

FIGURE 18. *Influence of creep rate on ductility at different temperatures.*

The creep rate is the average value obtained during the second stage.

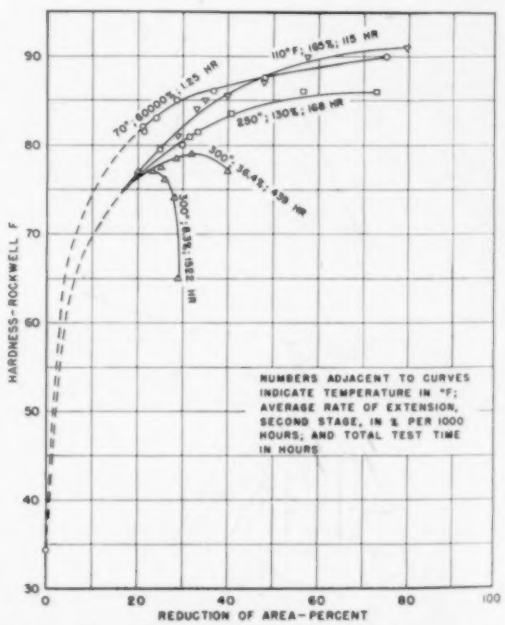
70°; 60000%; 125 HR
110° F; 165%; 115 HR
250°; 130%; 168 HR
300°; 36.4%; 439 HR
300°; 76.9%; 251 HR
NUMBERS ADJACENT TO CURVES INDICATE TEMPERATURE IN °F; AVERAGE RATE OF EXTENSION, SECOND STAGE, IN % PER 1000 HOURS; AND TOTAL TEST TIME IN HOURS
HARDNESS - ROCKWELL F
REDUCTION OF AREA - PERCENT

FIGURE 20. *Effect of plastic deformation at different temperatures and rates on hardness at room temperature.*

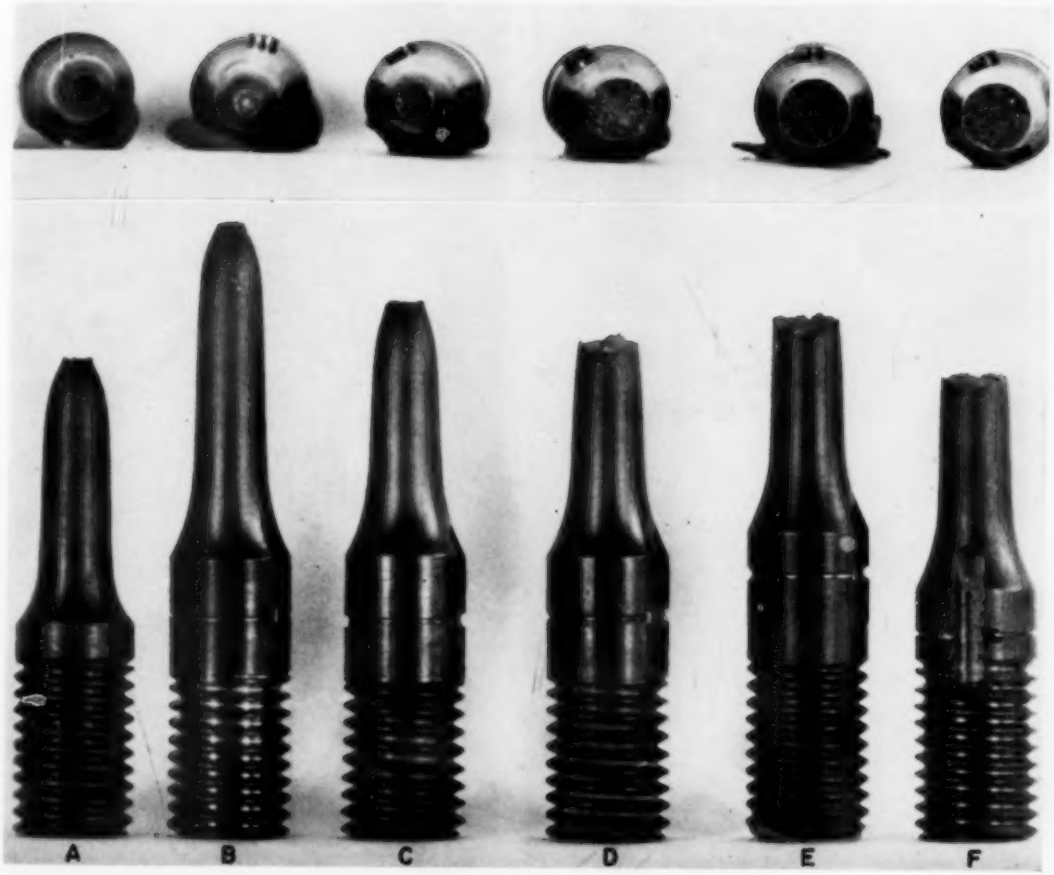

FIGURE 21. *Specimens after fracturing at different temperatures and rates; ×1.*

	Test		Elongation in 2 in.	Reduction of area
	Temperature	Strain rate		
	°F	%/1,000 hr	%	%
A	80	60,000	51.0	88
B	110	165	62.5	90
C	250	130	59.4	79
D	300	36.4	46.0	47
E	300	8.3	36.5	29
F	300	8.3	36.5	29

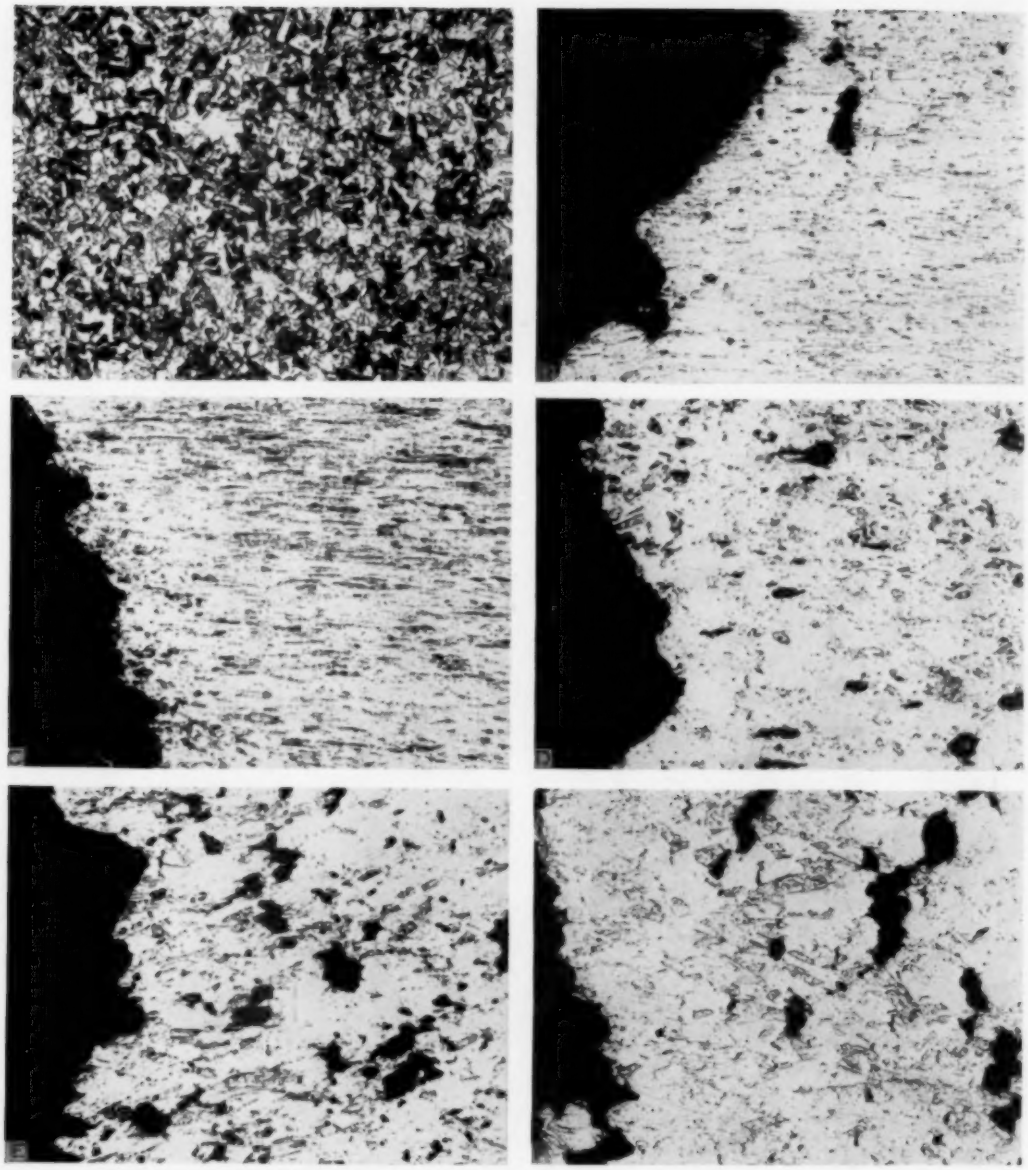

FIGURE 22. *Grain size of annealed copper and structures at fracture of specimens tested at different temperatures and rates.*

Longitudinal sections etched in equal parts NH_4OH and H_2O_2 (3%).

	Test		Elongation in 2 in.	Reduction of area	Remarks
	Temperature	Strain rate,			
	° F	%/1,000 hr	%	%	
A					×75; as annealed; 0.025-mm diam of average grain.
B	80	60,000	51.0	88	×100.
C	110	165	62.5	90	×100.
D	250	130	59.4	79	×100.
E	300	36.4	46.0	47	×100.
F	300	8.3	36.5	29	×100.

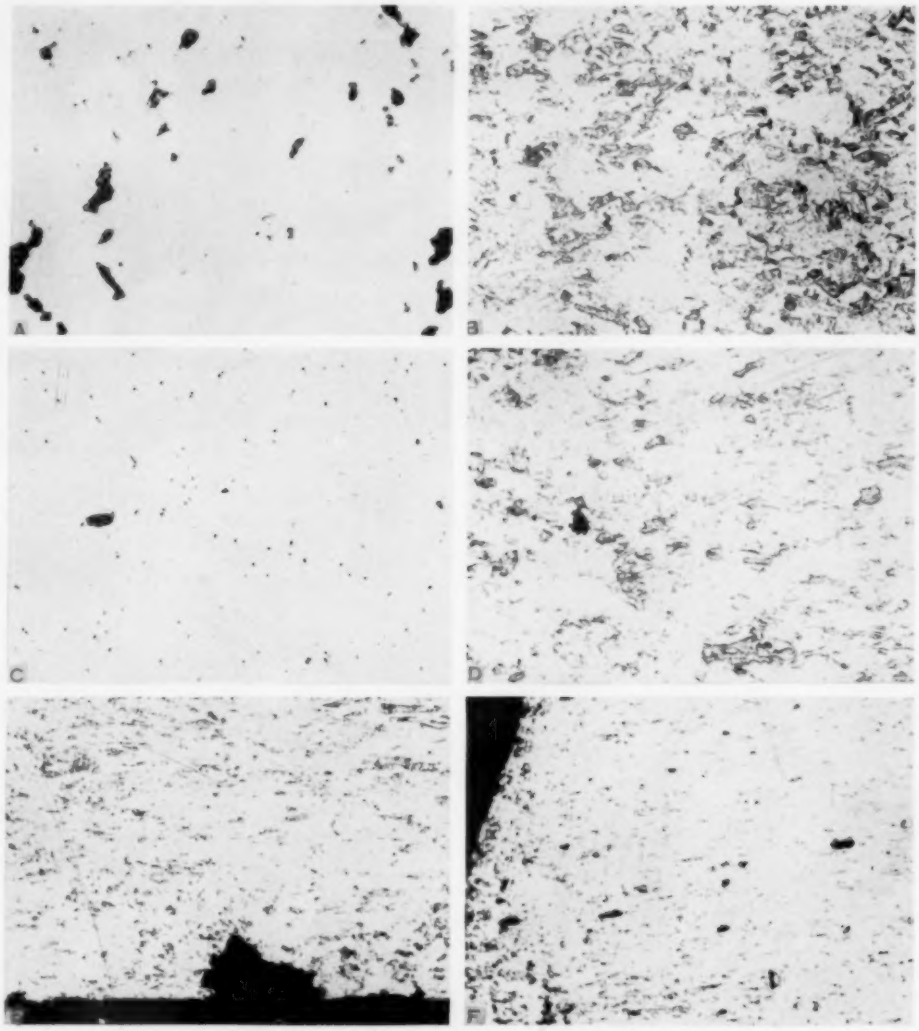

FIGURE 23. *Effect of temperature, rate, and plastic deformation on microcracking.*

Longitudinal sections near axis of specimen, except as indicated, etched in equal parts of NH_4OH and H_2O_2 (3%). Original magnification, ×100 (reduced one-tenth in reproduction).

	Test		Remarks
	Temperature	Strain rate	
	°F	%/1,000 hr	
A	300	8.3	Structure 0.05 in. from complete fracture. Structure at fracture is shown in fig. 22, *F*.
B	300	8.3	Same specimen as above, structure at deformation corresponding to the beginning of third stage.
C	250	1.5(a)	(a) 19,200 psi for 2,540 hr; (b) 22,400 psi for 483 hr; stopped in third stage; structure at deformation corresponding to the beginning of third stage.
	250	37.8(b)	
D	250	10.1	Stopped in third stage; fractured at room temperature; structure at deformation corresponding to the beginning of third stage.
E	250	10.1	Same specimen as above; structure at surface 0.05 in. from complete fracture.
F	250	1.15	Extended 9% at room temperature; 19,200 psi at 250° F for 2,700 hr; stopped in second stage and then fractured at room temperature; structure at complete fracture.

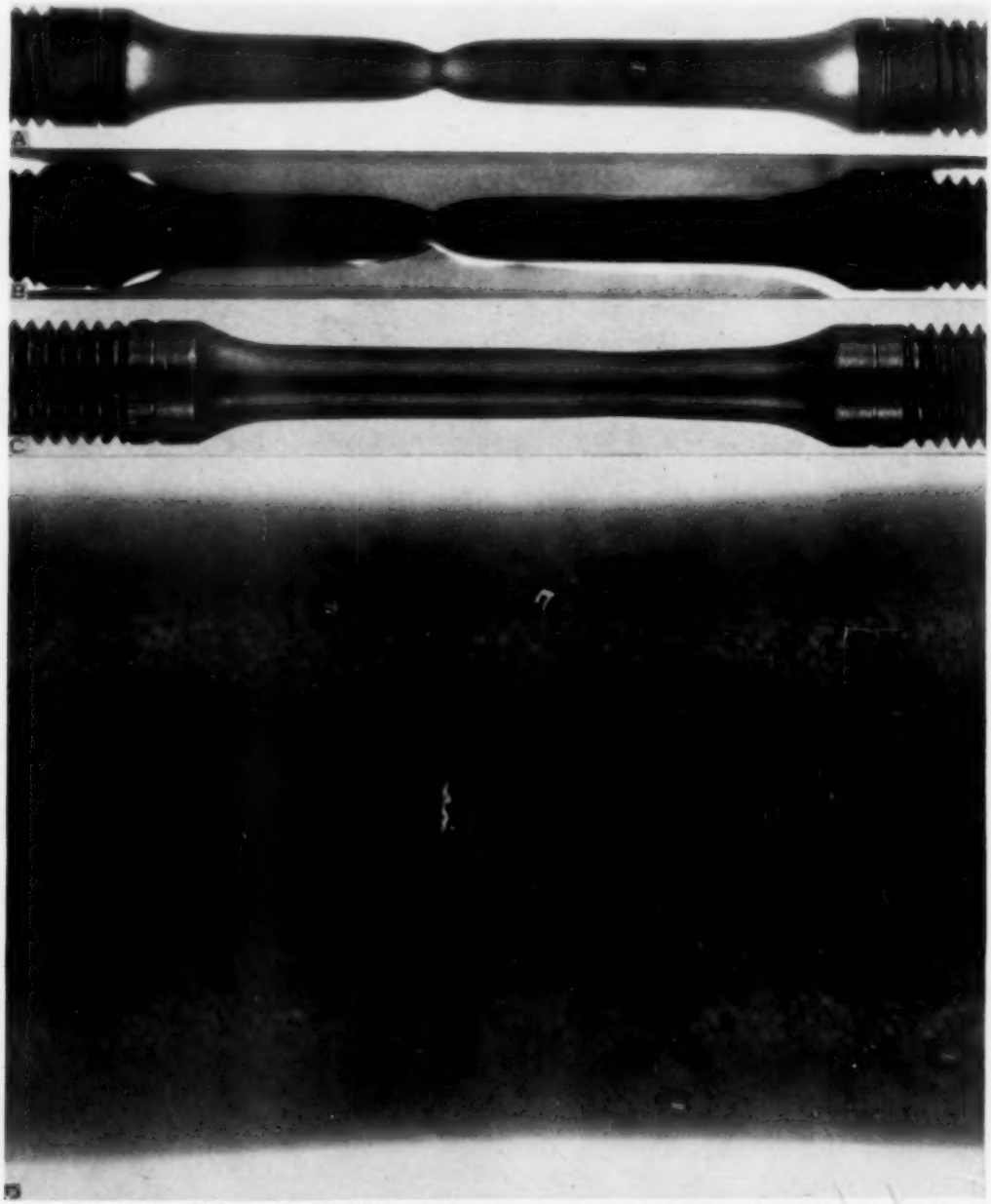

FIGURE 24. *Photographs and radiograph of specimens after testing at different temperatures and rates.*

	Test		Remarks
	Temperature	Strain rate	
	°F	%/1,000 hr	
A	80	60,000	Photograph, ×1.
B	80	60,000	Radiograph of above specimen, indicating the presence of a crack in the necked section.
C	250	1.5 (a)	(a) 19,200 psi for 2,540 hr; (b) 22,400 psi for 483 hr; photograph ×1.
		37.8 (b)	
D	250	1.5	Photograph, ×10 of above specimen showing the presence of a crack at the surface of the necked section.
		37.8	

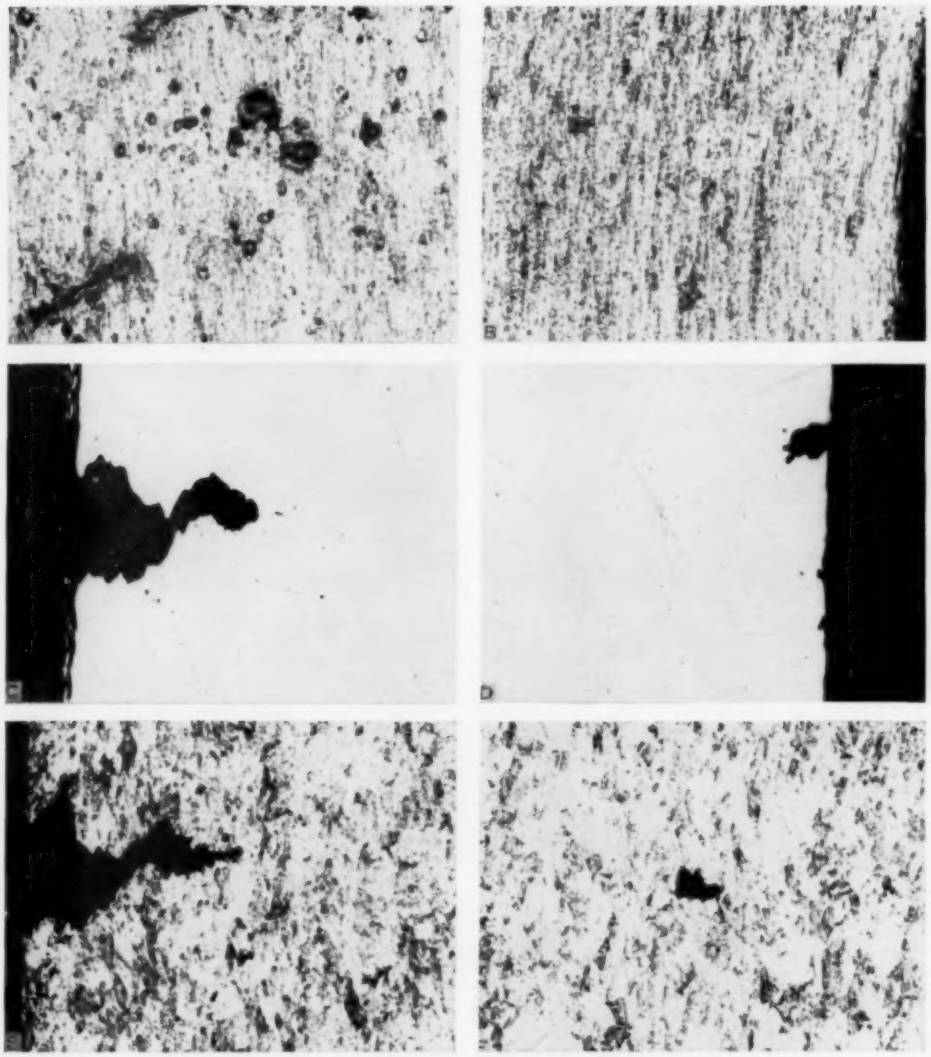

FIGURE 25. *Effect of testing conditions on the initiation of microcracks.*

Longitudinal sections, *A*, *B*, *E*, and *F* etched in equal parts NH_4OH and H_2O_2 (3%), *C* and *D* unetched. Original magnification, ×100 (reduced one-tenth in reproduction).

	Test		Remarks
	Temperature	Strain rate	
	° *F*	%/1,000 hr	
A	80	60,000	Structure at the axis of necked section of specimen shown in fig. 24, *A* and *B*.
B	80	60,000	Structure at the surface of the necked section of above specimen.
C	250	1.5	Structure at the surface of necked section of specimen shown in fig. 24, *C* and *D*.
		37.8	
D	250	1.5	Same as *C*, except that the surfaces are diametrically opposite.
		37.8	
E	250	1.5	Same section as *C*, after etching.
		37.8	
F	250	1.5	Same section as *C*, structure at the axis of the specimen.
		37.8	

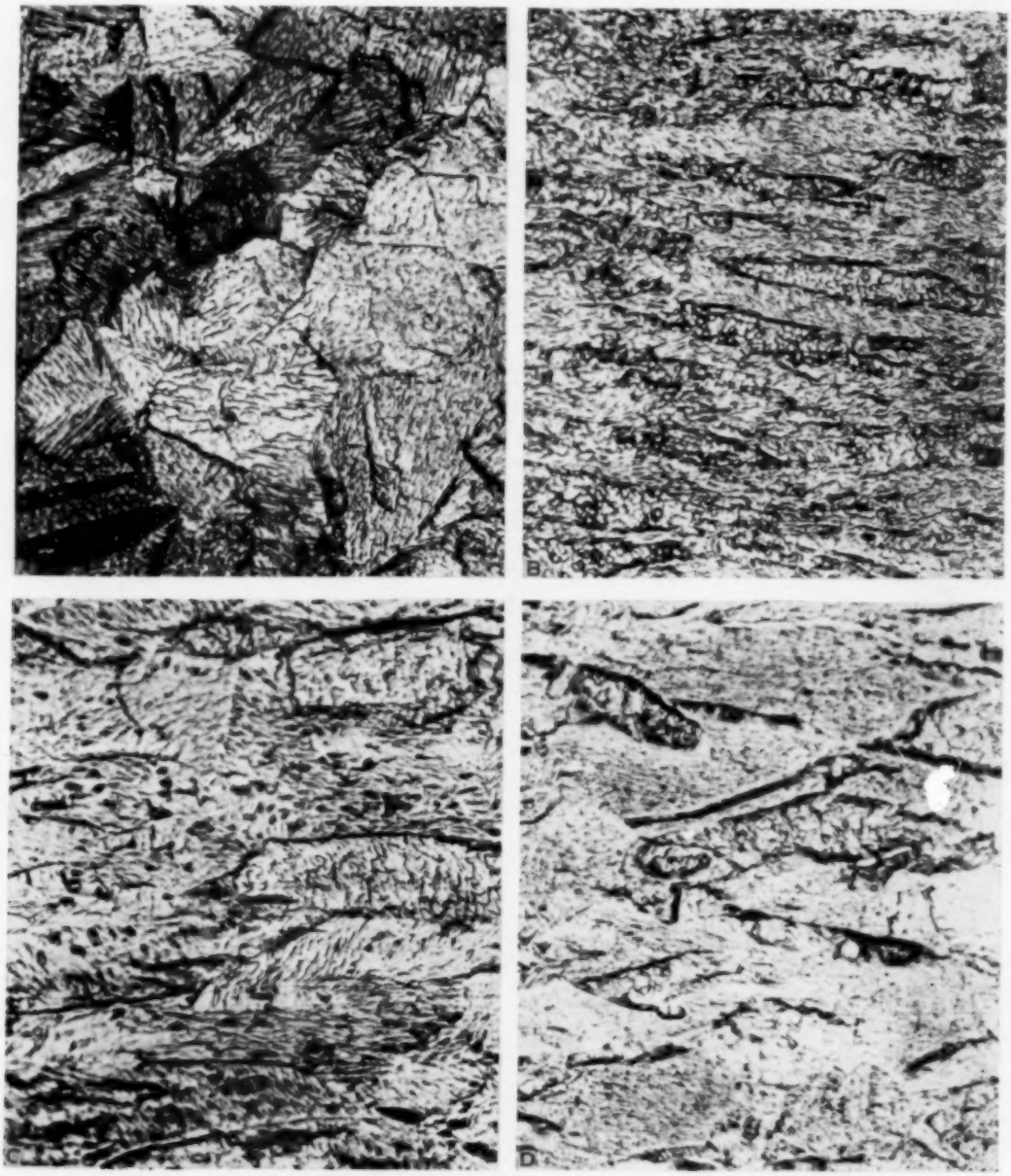

FIGURE 26. *Effect of testing conditions on the structure of copper initially as annealed.*

Longitudinal sections etched in 3.5 parts glacial acetic acid, 4.5 parts nitric acid (conc.), and 2 parts absolute alcohol. ×750.

	Test		Remarks
	Temperature	Strain rate	
	°F	%/1,000 hr	
A			As annealed.
B	80	60,000	Structure near axis of specimen 0.10 in. from position of complete fracture.
C	110	165	Do.
D	250	130	Do.

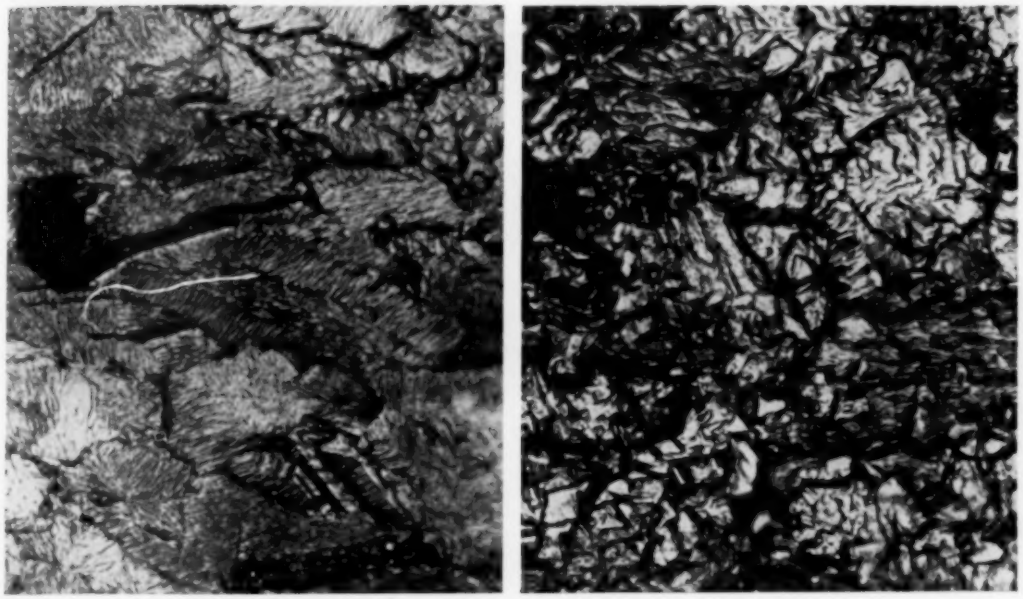

FIGURE 27. *Effect of testing conditions on structure of copper initially as annealed.*

Longitudinal sections etched in 3.5 parts glacial acetic acid and 4.5 parts nitric acid (conc.), and 2 parts absolute alcohol, ×750.

	Test		Remarks
	Temperature	Strain rate	
	°F	%/1,000 hr	
A	300	36.4	Structure near axis of specimen 0.10 in. from position of complete fracture.
B	300	8.3	Do.

Journal of Research of the National Bureau of Standards Vol. 45, No. 2, August 1950 Research Paper 2122

Purification, Purity, and Freezing Points of Twenty-Nine Hydrocarbons of the API-Standard and API-NBS Series[1]

By Anton J. Streiff,[2,3] Laurel F. Soule,[2] Charlotte M. Kennedy,[2] M. Elizabeth Janes,[2,3] Vincent A. Sedlak,[2] Charles B. Willingham,[4] and Frederick D. Rossini[3]

This report describes the purification and determination of freezing points and purity of the following 29 hydrocarbons of the API-Standard and API-NBS series: 2,2,4,6,6-pentamethylheptane; 1,1,2-trimethylcyclopropane; *cis*-2-hexene; *cis*-3-hexene; 2-methyl-1-pentene; 4-methyl-1-pentene; 3-methyl-trans-2-pentene; 4-methyl-*cis*-2-pentene; 4-methyl *trans*-2-pentene; 4,4-dimethyl-1-pentene; 4,4-dimethyl-*trans*-2-pentene; 2,3,3-trimethyl-1-butene; *trans*-4-octene; 1-nonene; 1-decene; 1-undecene; 1,3-butadiene;1,2-pentadiene; 1,*cis*-3-pentadiene; 1,*trans*-3-pentadiene; 1,4-pentadiene; 2,3-pentadiene; 2-methyl-1,3-butadiene (isoprene); 1,5-hexadiene; 2,3-dimethyl-1,3-butadiene; 4-ethenyl-1-cyclohexene-(4-vinyl-1-cyclohexene); *cis*-decahydronaphthalene; *trans*-decahydronaphthalene; 2,3-dihydroindene (indan).

[1] This investigation was performed at the National Bureau of Standards as part of the work of the American Petroleum Institute Research Project 6 on the Analysis, Purification, and Properties of Hydrocarbons.

[2] Research Associate on the American Petroleum Institute Research Project 6.
[3] Present address: Carnegie Institute of Technology, Pittsburgh, Pa.
[4] Present address: Mellon Institute of Industrial Research, Pittsburgh, Pa.

890983—50——5

TABLE 1. *Information on the purification of 29 API–Standard and API–NBS hydrocarbons*—Continued

Compound	Laboratory [a] providing starting material	Hydrocarbon charged for distillation		Distillation [b]							Volume of selected sample	
		Volume	Purity	Kind [c]	Azeotrope-forming substance [d]	Amount of hydrocarbon in the azeotropic distillate [e]	Distilling column number [b]	Number of theoretical plates [b] (approx.)	Reflux ratio [b] (approx.)	Rate of collection of distillate	Results plotted in figure	API Standard	API–NBS
		Liters	*Mole %*			*% by volume*				*ml/hour*		*ml*	*ml*
4,4-Dimethyl-1-pentene	APIRP45	6.90	99.34 ±0.12	Reg			5	125	125/1	12.5	22		
4,4-Dimethyl-*trans*-2-pentene	APIRP45	3.01	99.79 ±0.08	Reg			11A	200	160/1	4.5	23	1,060	250
2,3,3-Trimethyl-1-butene	General Motors	4.98	99.43 ±0.06	Reg			12A	200	160/1	4.5	24	1,075	300
		15.00	98.64 ±0.12	Reg			6	125	125/1	12.5	25		
		6.20	99.93 ±0.04	Reg			11A	200	160/1	4.5	26	1,550	500
trans-4-Octene	APIRP45	4.66	93.8 ±0.2	Reg			3A	200	160/1	4.5	27	1,115	350
1-Nonene	APIRP45	2.50	98.59 ±0.24	Reg			4	200	160/1	4.5	28		
		2.06	99.70 ±0.18	Azeo	Cell	52	2A	200	160/1	4.5	29	1,150	355
1-Decene	APIRP6 [g]	12.00		Reg			6	125	125/1	12.5	30		
		5.65	99.76 ±0.07	Reg			12A	200	160/1	4.5	31	1,695	500
1-Undecene	APIRP45	4.10	99.71 ±0.08	Reg			13	130	145/1	8.5	32	1,300	360
1,3-Butadiene	Phillips	2.90	99.83 ±0.06	Reg			1A	150	120/1	2.25	33	1,860	440
1,2-Pentadiene	Penn State	1.66	95.7 ±0.3	Reg			11A	200	180/1	4.0	34	470	150
1,*cis*-3-Pentadiene	Rubber Reserve	[i] 5.10		Reg			9	135	185/1	4.0	35		
		[m] 4.57		Azeo	Methanol	84	4	200	160/1	4.5	36	1,075	290
1,*trans*-3-Pentadiene	Rubber Reserve	[i] 5.10		Reg			9	135	185/1	4.0	35		
		[m] 4.30		Azeo	Methanol	85	4	200	160/1	4.5	37	1,050	220
1,4-Pentadiene	APIRP45	2.03	99.80 ±0.06	Reg			1A	150	170/1	1.5	38	1,050	255
2,3-Pentadiene	Penn State	2.60	91.2 ±0.1	Reg			9	135	185/1	4.0	39	950	285
2-Methyl-1,3-butadiene(Isoprene)	APIRP6 [n]	[k] 6.60	93.7 ±0.3	Reg			13	130	145/1	8.5	40		
		[i] 4.16	99.87 ±0.06	Reg			2A	200	160/1	4.5	41	1,900	400
1,5-Hexadiene	Penn State	1.94	99.84 ±0.08	Reg			13	130	145/1	8.5	42	1,050	310
2,3-Dimethyl-1,3-butadiene	Penn State	2.30	98.17 ±0.10	Reg			4	200	160/1	4.5	43	960	250
4-Ethenyl-1-cyclohexene (4-Vinyl-1-cyclohexene)	APIRP6 [o]	[p] 5.80		Reg			14	125	125/1	12.5	44		
		[q] 5.80	99.84 ±0.07	Reg			4	200	160/1	4.5	45	1,750	490
cis-Decahydronaphthalene	APIRP6 [r]	[s] 5.30		Reg			7	130	145/1	8.5	46		
		[t] 5.30		Reg			11A	200	160/1	4.5	47	1,100	300
trans-Decahydronaphthalene	APIRP6 [r]	[s] 5.30		Reg			7	130	145/1	8.5	46		
		[t] 5.12		Reg			11A	200	160/1	4.5	48	1,180	270
2,3-Dihydroindene (Indan)	APIRP45	2.67		Reg			12	135	185/1	4.0	49		
		2.25	99.67 ±0.04	Reg			15A	200	160/1	4.5	50	1,050	200

[a] The abbreviations represent the following laboratories APIRP45; American Petroleum Institute Research Project 45 at the Ohio State University, Columbus, Ohio. Penn State; Hydrocarbon Laboratory, Pennsylvania State College, State College, Pa. Anglo-Iranian; Anglo-Iranian Oil Co., Research Laboratories, Sunbury-on Thames, England. General Motors; General Motors Corporation, Detroit, Mich. Phillips; Phillips Petroleum Co., Bartlesville, Okla. Rubber Reserve; Office of Rubber Reserve, Washington, D. C. APIRP6; American Petroleum Institute Research Project 6 at the National Bureau of Standards, Washington, D. C.

[b] See Reference [6] for further details.

[c] The abbreviations are: Azeo., azeotropic; Reg., regular.

[d] The abbreviations are: Me. Carb., methyl Carbitol (diethylene glycol monomethyl ether); Cell., Cellosolve (ethylene glycol monoethyl ether).

[e] Approximate value obtained from the actual volume of hydrocarbon recovered by extracting the azeotrope-forming substance with water in separatory funnels.

[f] After 28 days of distillation of this material, the remaining hydrocarbon was converted to higher boiling isomers, and approximately 20% of the charge was not recoverable as 1,1,2-trimethylcyclopropane

[g] Obtained by purchase of commercially available material from the Connecticut Hard Rubber Co., New Haven, Conn.

[h] One of two similar charges.

[i] This charge consisted of material having substantially the same composition from each of the two previous distillations (see footnote h).

[j] One of two charges of similar material, one of which was 6.2 liters, and the other of which was 15.0 liters. Both 4-methyl-*cis*-2-pentene and 4-methyl-*trans*-2-pentene were obtained from this material (see fig. 18).

[k] This charge consisted of material having substantially the same composition from each of the two previous distillations (see footnote j).

[l] One of two similar charges. Both 1,*cis*-3-pentadiene and 1,*trans*-3-pentadiene were obtained from this material (see fig. 35).

[m] This charge consisted of material having substantially the same composition from each of the two previous distillations (see footnote l).

[n] Obtained by purchase of commercially available material from Newport Industries, Inc., Pensacola, Fla.

[o] Obtained by purchase of commercially available material from Koppers Co., Inc., Pittsburgh, Pa.

[p] One of three similar charges.

[q] This charge consisted of material having substantially the same composition from each of the three previous distillations (see footnote k).

[r] Obtained by purchase of commercially available material from the Eastman Kodak Co., Rochester, N. Y.

[s] One of three similar charges. Both *cis*- and *trans*-decahydronaphthalene were obtained from this material (see fig. 46).

[t] This charge consisted of material having substantially the same composition from each of the three previous distillations (see footnote s).

III. Purification

The procedures followed in the process of purification and determination of purity were the same as those described in the previous reports [2, 3, 4, 5].

In addition to the name of the laboratory supplying the starting materials, table 1 and its footnotes give complete information for each distillation for each of the compounds.

Details of the distillation apparatus and operations are described in reference [6].

Figures 1 to 50 inclusive show graphically the results of the distillation operations listed in table 1. These figures give each of the following properties

890982—59——6

as a function of volume of hydrocarbon distillate: the refractive index (n_D at 25° C, to ±0.0001), the boiling point of the distillate (at the controlled pressure of 725 mm Hg, to ±0.01° C), the freezing point of selected fractions of hydrocarbon distillate (in air at 1 atm, usually with a precision near ±0.003° C), and the purity of the hydrocarbon distillate. The letters W, X, Y, and Z, indicate the disposition of the material as follows: W, returned to the laboratory supplying the material; X, blended for redistillation; Y, used for the API–Standard material; and Z, used for the API–NBS material.

As demonstrated in the previous reports [2, 3, 4, 5], the blending of fractions of distillate for the preparation of material of the highest purity can be done safely only on the basis of the freezing points of selected fractions.

IV. Freezing Points, Cryoscopic Constants, and Purity

Table 2 gives the following information for each of the 29 compounds, except as otherwise indicated: The kind of time-temperature curves, whether freezing or melting, used to determine the freezing point [7]; the freezing point of the actual sample, in air at 1 atm [7], for both the API–Standard and API–NBS lots; the calculated value of the freezing point for zero impurity [7]; the value of the cryoscopic constant, determined from the lowering of the freezing point on the addition of a known amount of a suitable impurity [7]; and the resulting calculated amount of impurity in the API–Standard and API–NBS material.

TABLE 2. *Freezing points and purity of 29 API-Standard and API-NBS hydrocarbons*

Compound	Kind of time-temperature observations used to determine the freezing point [a]	Freezing point of the actual selected sample in air at 1 atm		Freezing point for zero impurity in air at 1 atm	Cryoscopic constant [a] A	Calculated amount of impurity in the actual selected sample [b]	
		API-Standard	API-NBS			API-Standard	API-NBS
		°C	°C	°C	*Mole fraction/deg*	*Mole %*	*Mole %*
2,2,4,6,6-Pentamethylheptane	M	−66.967	−66.967	−66.92 ±0.03	0.0129	0.06 ±0.04	0.06 ±0.04
1,1,2-Trimethylcyclopropane	M		−138.209	−138.180 ±0.020	.0418		.12 ±0.08
cis-2-Hexene	M	−141.170	−141.146	−141.135 ±0.020	.0585	0.20 ±0.12	.06 ±0.03
cis-3-Hexene	F	−137.845	−137.839	−137.820 ±0.020	.0522	.13 ±0.08	.10 ±0.08
2-Methyl-1-pentene	M	−135.803	−135.791	−135.760 ±0.020	.0449	.19 ±0.09	.14 ±0.06
4-Methyl-1-pentene [c]	F	−153.69(I)	−153.68(I)	−153.63 ±0.04(I)	.03	.18 ±0.12	.15 ±0.12
				−154.90 ±0.04(II)(u)			
3-Methyl-*trans*-2-pentene	M	−134.872	−134.866	−134.840 ±0.020	.0425	.14 ±0.09	.11 ±0.09
4-Methyl-*cis*-2-pentene	M	−134.447	−134.446	−134.430 ±0.015	.0461	.08 ±0.07	.07 ±0.07
4-Methyl-*trans*-2-pentene	M	−140.960	−140.826	−140.810 ±0.015	.0494	.25 ±0.07	.08 ±0.07
4,4-Dimethyl-1-pentene	F and M	−136.635	−136.635	−136.600 ±0.020	.0417	.15 ±0.08	.15 ±0.08
4,4-Dimethyl-*trans*-2-pentene	M	−115.263	−115.262	−115.235 ±0.010	.0327	.09 ±0.03	.09 ±0.03
2,3,3-Trimethyl-1-butene	F	−110.010	−109.994	−109.85 ±0.10	.00367	.06 ±0.04	.05 ±0.04
trans-4-Octene	M	−93.838	−93.838	−93.810 ±0.020	.0571	.16 ±0.11	.16 ±0.11
1-Nonene	M	−81.41	−81.41	−81.37 ±0.03	.0591	.24 ±0.18	.24 ±0.18
1-Decene	F	−66.329	−66.326	−66.310 ±0.020	.0594	.11 ±0.07	.09 ±0.07
1-Undecene	F	−49.206	−49.206	−49.185 ±0.020	.0421	.09 ±0.08	.09 ±0.08
1,3-Butadiene	F	−108.939	−108.937	−108.915 ±0.010	[d] .03560	.08 ±0.04	.08 ±0.04
1,2-Pentadiene	M	−137.326	−137.301	−137.26 ±0.03	.0512	.34 ±0.15	.21 ±0.13
1,*cis*-3-Pentadiene	F	−140.840	−140.836	−140.820 ±0.010	.0414	.08 ±0.04	.07 ±0.04
1,*trans*-3-Pentadiene	F	−87.501	−87.483	−87.470 ±0.010	.0264	.08 ±0.03	.03 ±0.03
1,4-Pentadiene	M	−148.288	−148.287	−148.275 ±0.010	.0521	.07 ±0.05	.06 ±0.05
2,3-Pentadiene	M	−125.680	−125.680	−125.650 ±0.020	.0384	.15 ±0.07	.11 ±0.07
2-Methyl-1,3-butadiene (isoprene)	M	−145.962	−145.962	−145.950 ±0.020	[d] .0330	.04 ±0.03	.04 ±0.03
1,5-Hexadiene	M	−140.702	−140.698	−140.680 ±0.015	.0505	.11 ±0.08	.09 ±0.08
2,3-Dimethyl-1,3-butadiene	M	−76.026	−76.020	−76.005 ±0.010	.0274	.06 ±0.03	.04 ±0.03
4-Ethenyl-1-cyclohexene (4-Vinyl-1-cyclohexene)	M	−108.748	−108.745	−108.720 ±0.020	.0367	.10 ±0.07	.09 ±0.07
cis-Decahydronaphthalene	M	−43.070	−43.048	−43.01 ±0.03	.0180	.11 ±0.05	.07 ±0.05
trans-Decahydronaphthalene	M	−30.415	−30.410	−30.400 ±0.015	.0291	.04 ±0.03	.03 ±0.03
2,3-Dihydroindene (Indan)	F	−51.430	−51.410	−51.400 ±0.010	.0204	.06 ±0.02	.02 ±0.02

[a] F indicates freezing, and M indicates melting. See reference [7] for experimental details and the definition of the cryoscopic constant.

[b] The values in this column were calculated as described in reference [7], using the values of the cryoscopic constants and freezing points for zero impurity given in the preceeding columns.

[c] This hydrocarbon has more than one crystalline form. The two forms indicated are labeled I and II in order of decreasing temperature of fusion (or freezing point). Form II will be, at its freezing point, in metastable equilibrium with the undercooled liquid, but will be unstable with respect to transition to the other solid form at the same temperature and pressure (1 atm). This is indicated by "u" in parentheses following the roman numeral.

[d] Not determined in this investigation. See reference [8].

Grateful acknowledgment is made to the organizations and individuals listed in section II of this report for their contributions of materials.

V. References

[1] National Bureau of Standards Tech. News Bull., No. 350 (June 1946).

[2] A. J. Streiff, E. T. Murphy, V. A. Sedlak, C. B. Willingham, and F. D. Rossini, J. Research NBS **37,** 331 (1946) RP1752.

[3] A. J. Streiff, E. T. Murphy, J. C. Cahill, H. F. Flanagan, V. A. Sedlak, C. B. Willingham, and F. D. Rossini, J. Research NBS **38,** 53 (1947) RP1760.

[4] A. J. Streiff, E. T. Murphy, J. C. Zimmerman, L. F. Soule, V. A. Sedlak, C. B. Willingham, and F. D. Rossini, J. Research NBS **39,** 321 (1947) RP1833.

[5] A. J. Streiff, J. C. Zimmerman, L. F. Soule, M. T. Butt, V. A. Sedlak, C. B. Willingham, and F. D. Rossini, J. Research NBS **41,** 323 (1948) RP1929.

[6] C. B. Willingham and F. D. Rossini, J. Research NBS **37,** 15 (1946) RP1724.

[7] A. R. Glasgow, Jr., A. J. Streiff, and F. D. Rossini, J. Research NBS **35,** 355 (1945) RP1676.

[8] A. R. Glasgow, Jr., N. C. Krouskop, J. Beadle, G. D. Axilrod, and F. D. Rossini, Anal. Chem. **20,** 410 (1948).

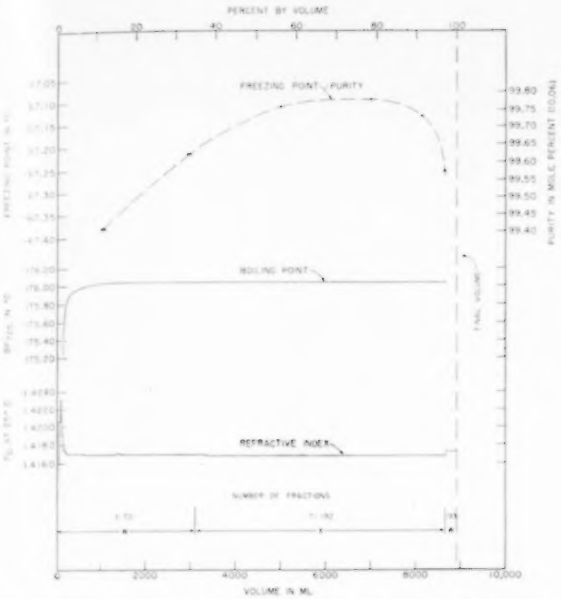

FIGURE 1. *First distillation of 2,2,4,4,6,6-pentamethylheptane.*
Regular distillation at 725 mm Hg in still 6(10/21/47 to 11/24/47).

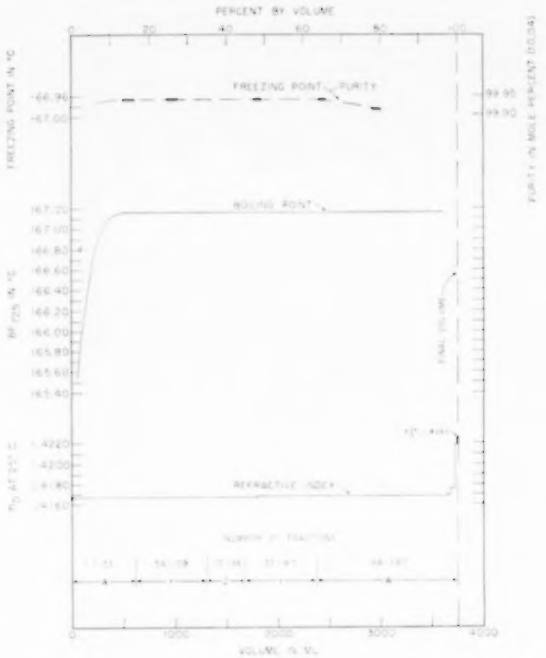

FIGURE 3. *Third and final distillation of 2,2,4,6,6-pentamethylheptane.*
Azeotropic distillation with diethylene glycol monomethyl ether at 725 mm Hg in still 12A (3/25/48 to 5/19/48).

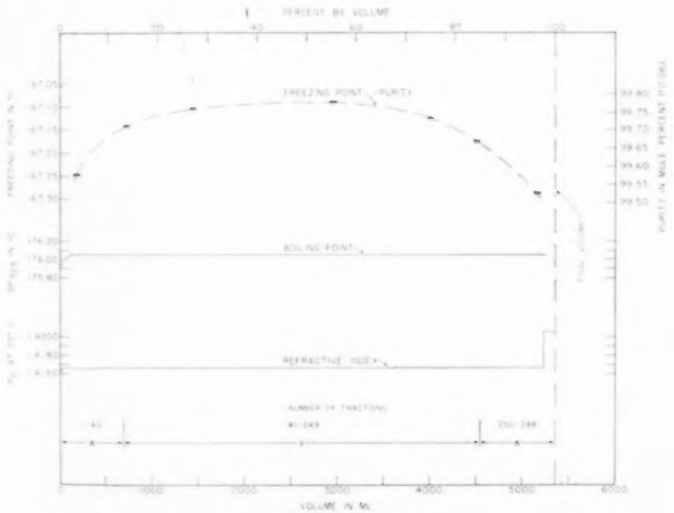

FIGURE 2. *Second distillation of 2,2,4,6,6-pentamethylheptane.*
Regular distillation at 725 mm Hg in still 2A (1/8/48 to 3/1/48).

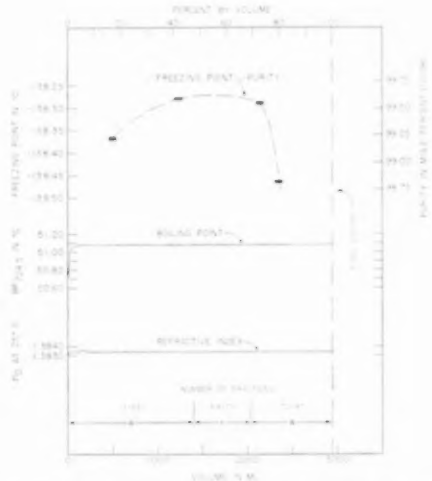

FIGURE 4. *First distillation of 1,1,2-trimethylcyclapropane.*
Regular distillation at 725 mm Hg in still 12A (7/18/47 to 8/16/47).

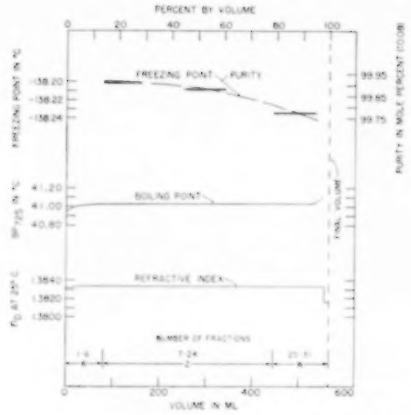

FIGURE 5. *Second and final distillation of 1,1,2-trimethylcyclopropane.*

Azeotropic distillation with acetone at 725 mm Hg in still 13(9/3/47 to 9/10/47).

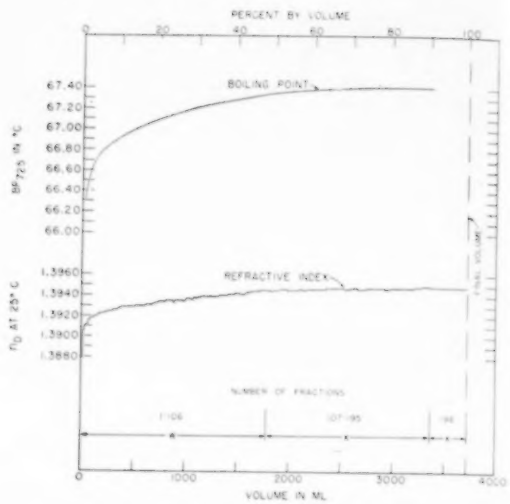

FIGURE 6. *First distillation of cis-2-hexene.*

Regular distillation at 725 mm Hg in still 4(12/24/48 to 1/27/49). The residue from the distillation (marked "x") was azeotropically distilled with ethanol and the hydrocarbon portion added to fractions 107 to 195 for redistillation.

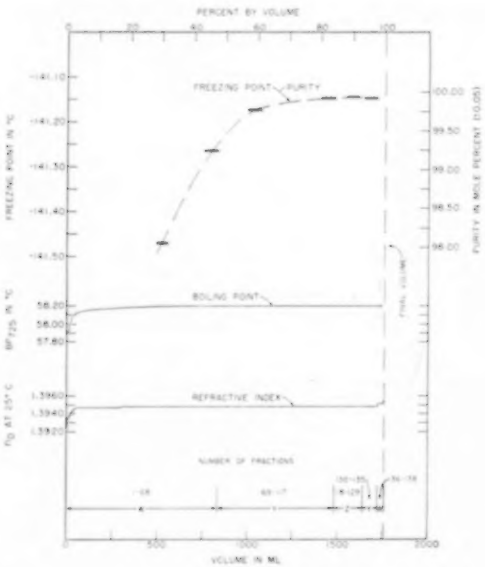

FIGURE 7. *Second and final distillation of cis-2-hexene.*

Azeotropic distillation with ethanol at 725 mm Hg in still 4(3/7/49 to 4/1/49).

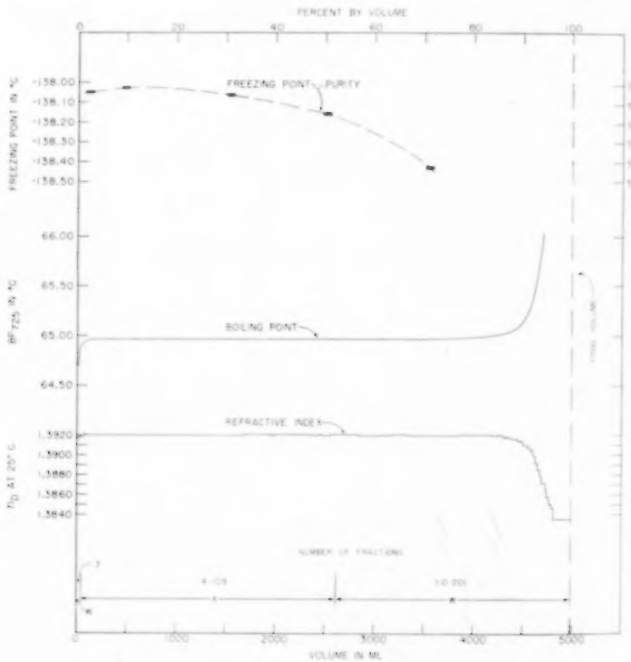

FIGURE 8. *First distillation of cis-3-hexene.*

Regular distillation at 725 mm Hg in still 10A(9/30/48 to 11/15/48).

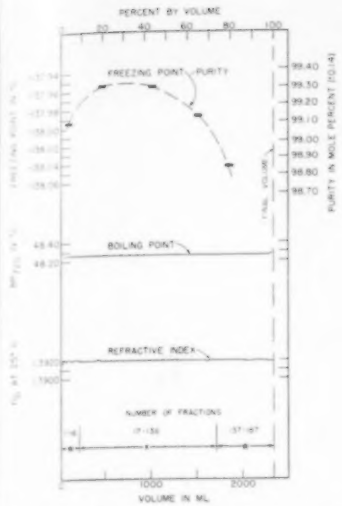

FIGURE 9. *Second distillation of cis-3-hexene.*

Azeotropic distillation with methanol at 725 mm Hg in still 15A (12/3/48 to 1/5/49).

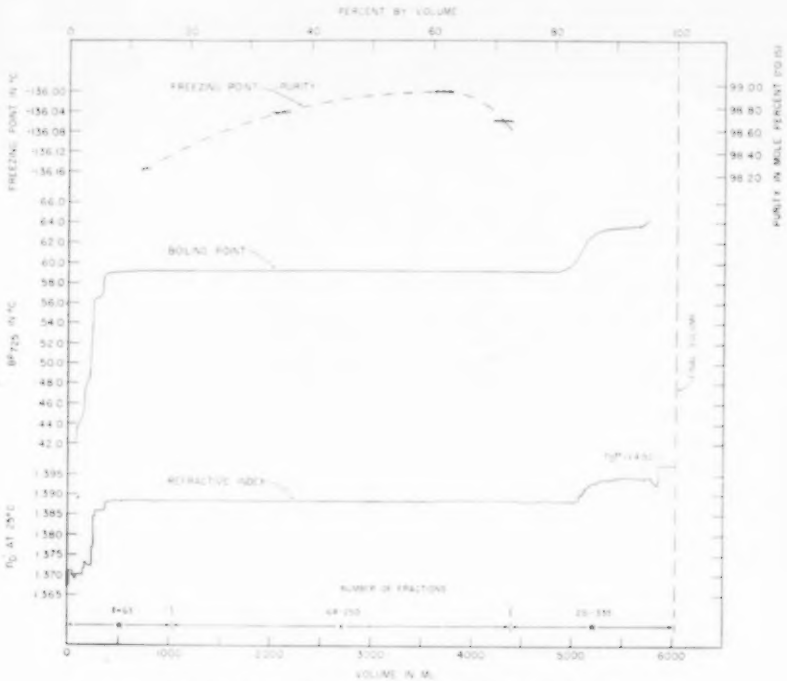

FIGURE 11. *First distillation of 2-methyl-1-pentene.*

Regular distillation at 725 mm Hg in still 9(8/1/47 to 10/7/47). This is one of two similar distillations.

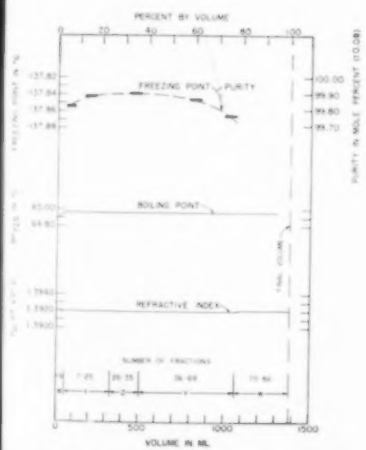

FIGURE 10. *Third and final distillation of cis-3-hexene.*

Regular distillation at 725 mm Hg in still 4(2/4/49 to 3/4/49).

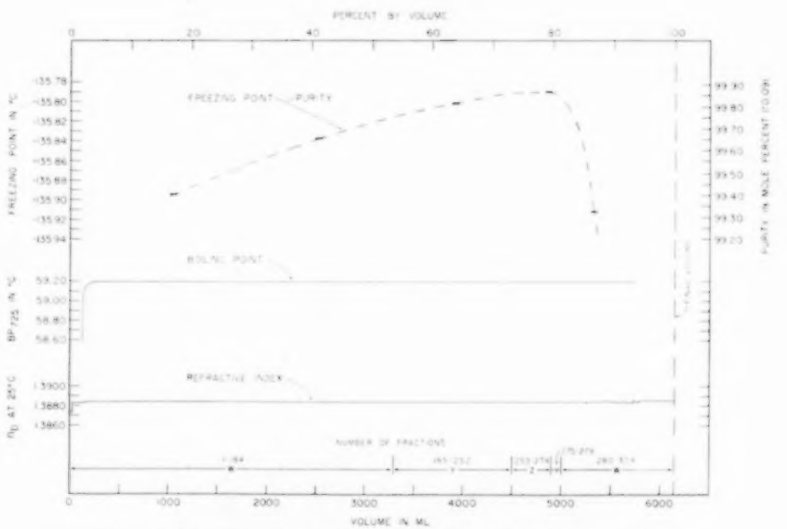

FIGURE 12. *Second and final distillation of 2-methyl-1-pentene.*

Regular distillation at 725 mm Hg in still 4(1/2/48 to 3/1/48). See footnote i of table 1.

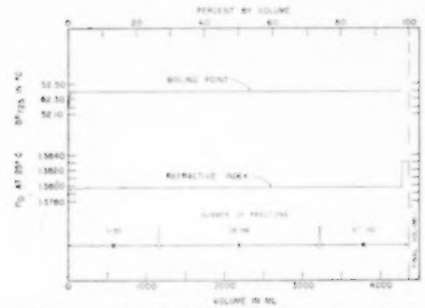

FIGURE 13. *First distillation of 4-methyl-1-pentene.*

Regular distillation at 725 mm Hg in still 13(4/4/47 to 4/28/47). One of two similar distillations.

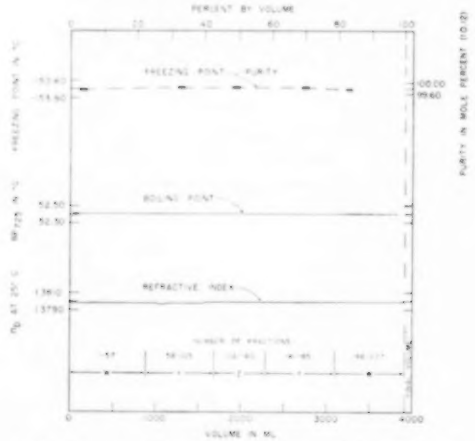

FIGURE 14. *Second and final distillation of 4-methyl-1-pentene.*

Regular distillation at 725 mm Hg in still 3A (5/27/47 to 7/7/47). See footnote i of table 1.

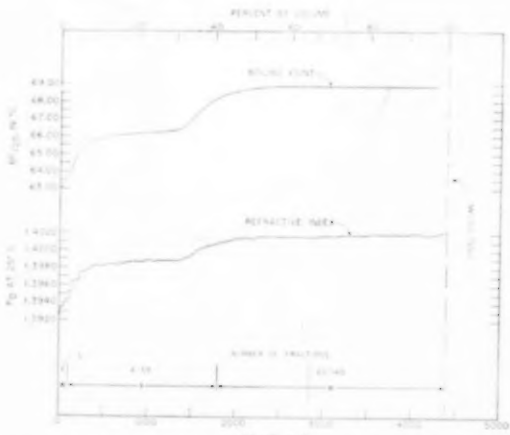

FIGURE 15. *First distillation of 3-methyl-trans-2-pentene.*

Regular distillation at 725 mm Hg in still 8(3/2/48 to 3/29/48). One of two similar distillations.

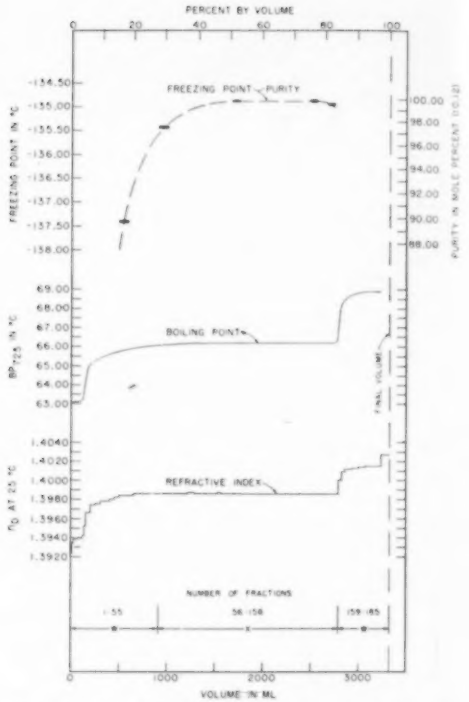

FIGURE 16. *Second distillation of 3-methyl-trans-2-pentene.*

Regular distillation at 725 mm Hg in still 2A (4/19/48 to 5/24/48). See footnote i of table 1.

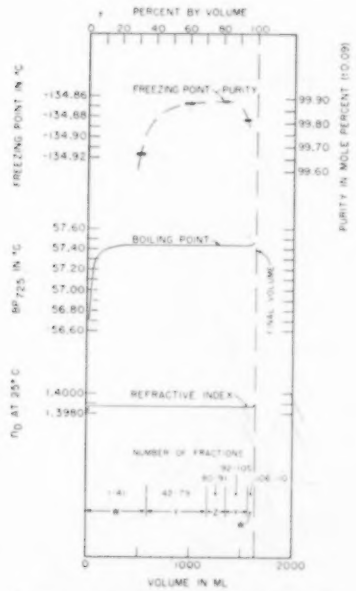

FIGURE 17. *Third and final distillation of 3-methyl-trans-2-pentene.*

Azeotropic distillation with ethanol at 725 mm Hg in still 12A (7/21/48 to 8/10/48).

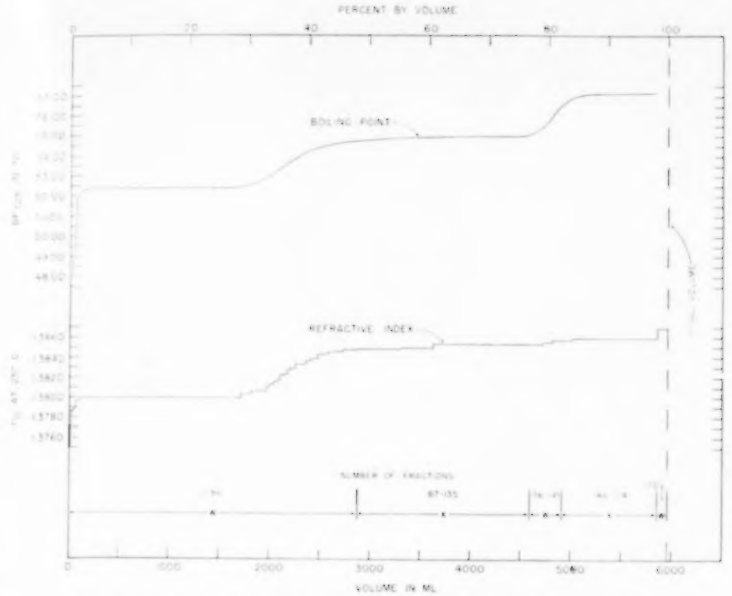

FIGURE 18. *First distillation of 4-methyl-2-pentene (cis + trans).*

Regular distillation at 725 mm Hg in still 13(6/26/47 to 7/28/47). One of two distillations of similar material. See footnote j of table 1. Fractions 87 to 135 were redistilled to obtain 4-methyl-*cis*-2-pentene (see fig. 19), and fractions 146–174 were redistilled to obtain 4-methyl-*trans*-2-pentene (see fig. 20).

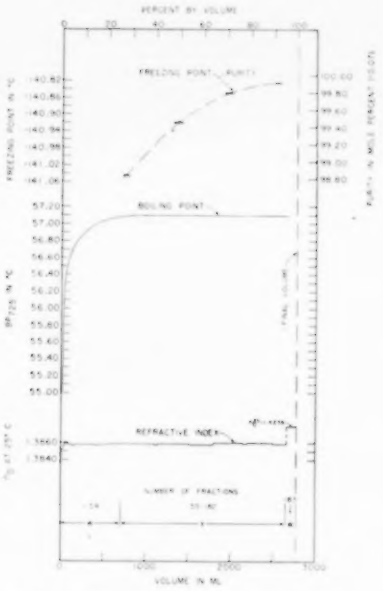

FIGURE 20. *Second distillation of 4-methyl-trans-2-pentene.*

Regular distillation at 725 mm Hg in still 11A (2/5/48 to 3/15/48). See footnote k of table 1.

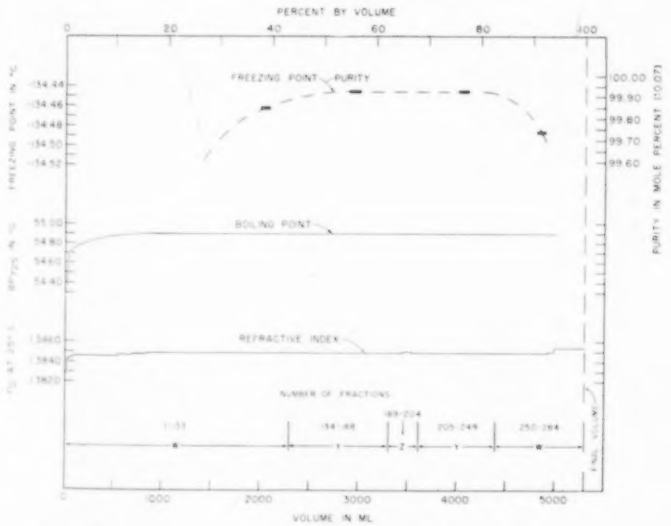

FIGURE 19. *Second and final distillation of 4-methyl-cis-2-pentene.*

Regular distillation at 725 mm Hg in still 15A (1/23/48 to 3/16/48). See footnote k of table 1.

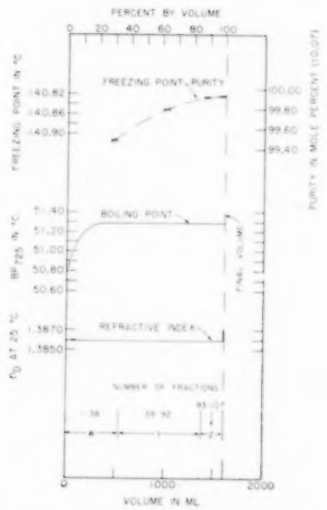

FIGURE 21. *Third and final distillation of 4-methyl-trans-2-pentene.*

Azeotropic distillation with ethanol at 725 mm Hg in still 3A (7/14/48 to 8/1/48).

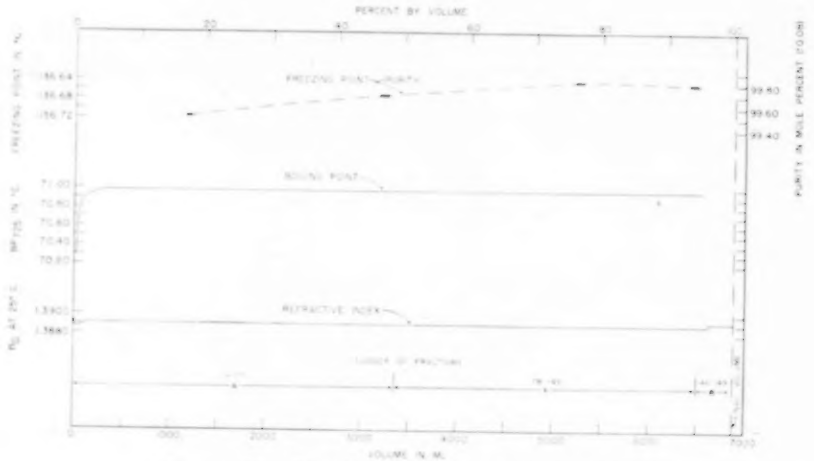

FIGURE 22. *First distillation of 4,4-dimethyl-1-pentene.*
Regular distillation at 725 mm Hg in still 5 (9/19/47 to 10/20/47).

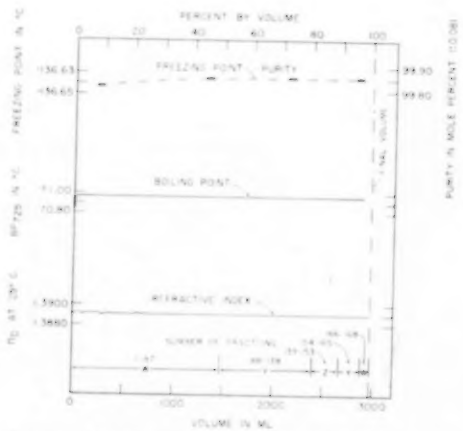

FIGURE 23. *Second and final distillation of 4,4-dimethyl-1-pentene.*
Regular distillation at 725 mm Hg in still 11A (10/30/47 to 12/1/47).

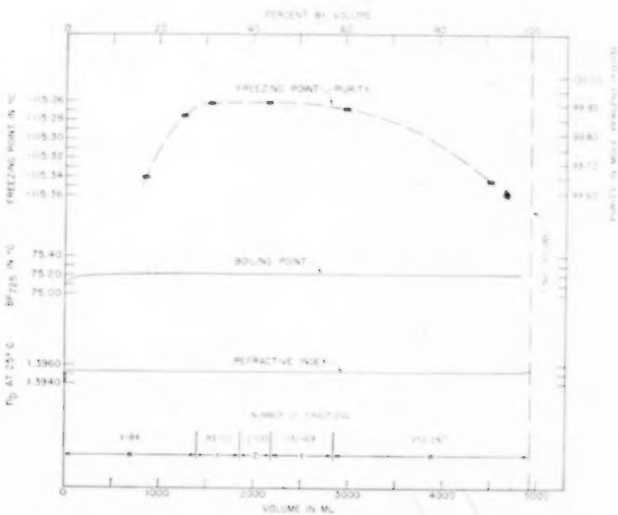

FIGURE 24. *First and only distillation of 4,4-dimethyl-trans-2-pentene.*
Regular distillation at 725 mm Hg in still 12A (1/19/49 to 3/9/49).

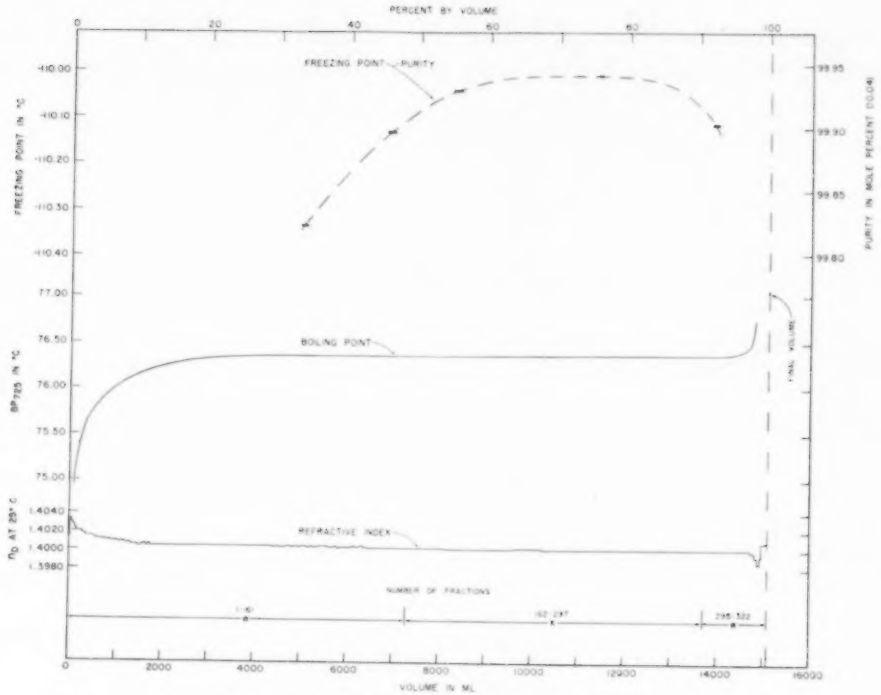

FIGURE 25. *First distillation of 2,3,3-trimethyl-1-butene.*
Regular distillation at 725 mm Hg in still 6 (8/22/47 to 10/20/47).

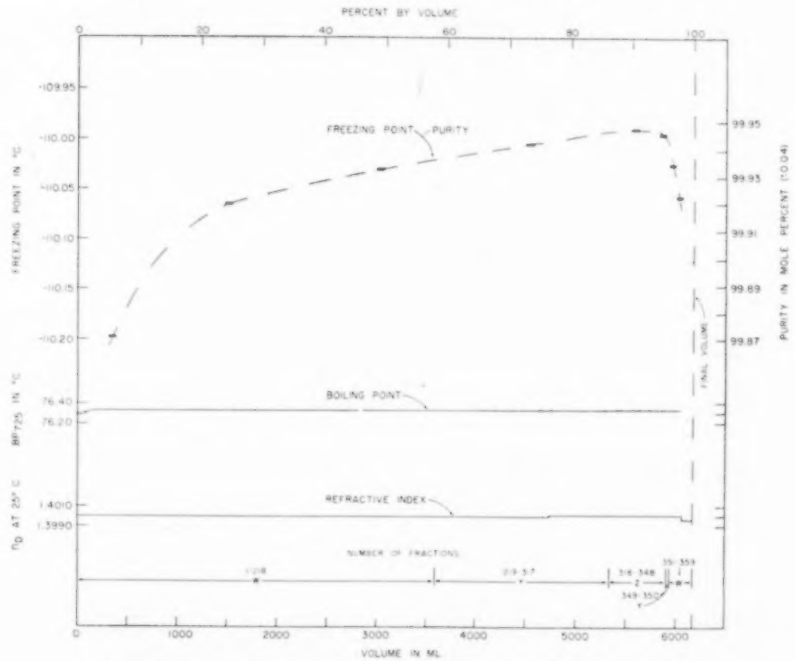

FIGURE 26. *Second and final distillation of 2,3,3-trimethyl-1-butene.*
Regular distillation at 725 mm Hg in still 11A (12/3/47 to 2/4/48).

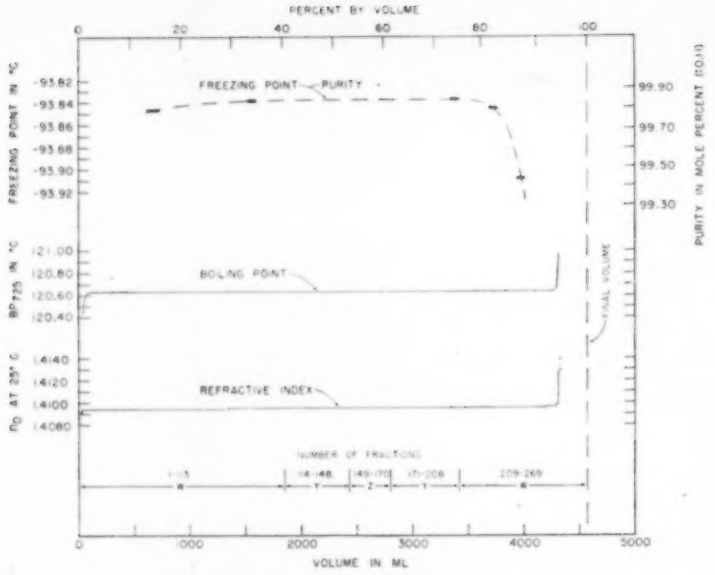

FIGURE 27. ***First and only distillation of trans-4-octene.***

Regular distillation at 725 mm Hg in still 3A (10/6/47 to 11/21/47).

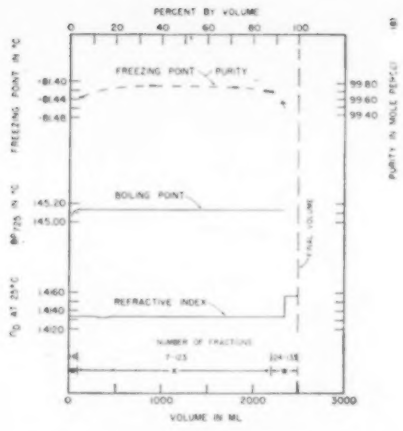

FIGURE 28. ***First distillation of 1-nonene.***

Regular distillation at 725 mm Hg in still 4 (10/7/47 to 11/4/47).

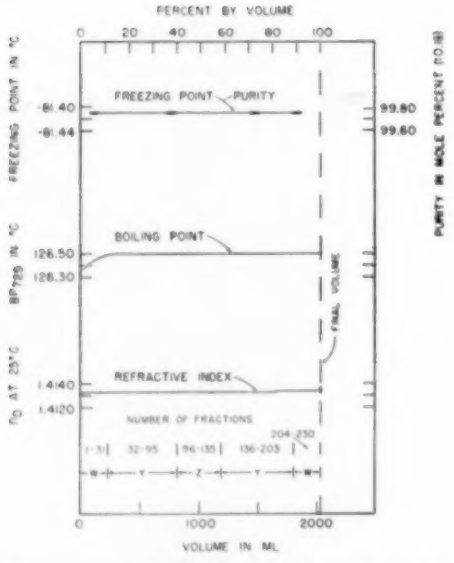

FIGURE 29. ***Second and final distillation of 1-nonene.***

Azeotropic distillation with ethylene glycol monoethyl ether at 725 mm Hg in still 2A (11/26/47 to 1/7/48).

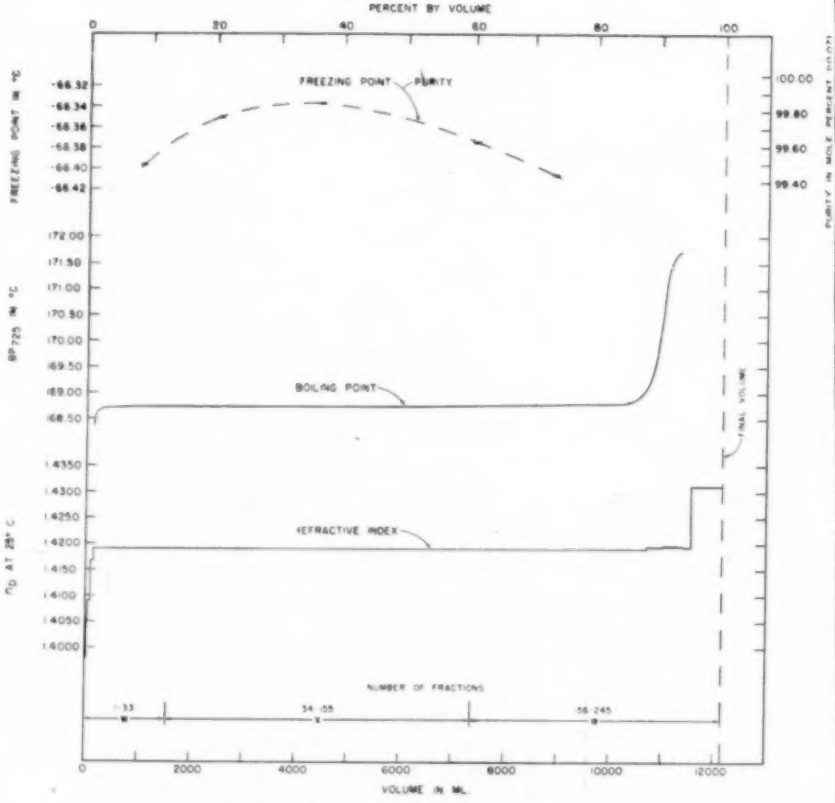

FIGURE 30. ***First distillation of 1-decene.***

Regular distillation at 725 mm Hg in still 6 (5/22/47 to 7/7/47).

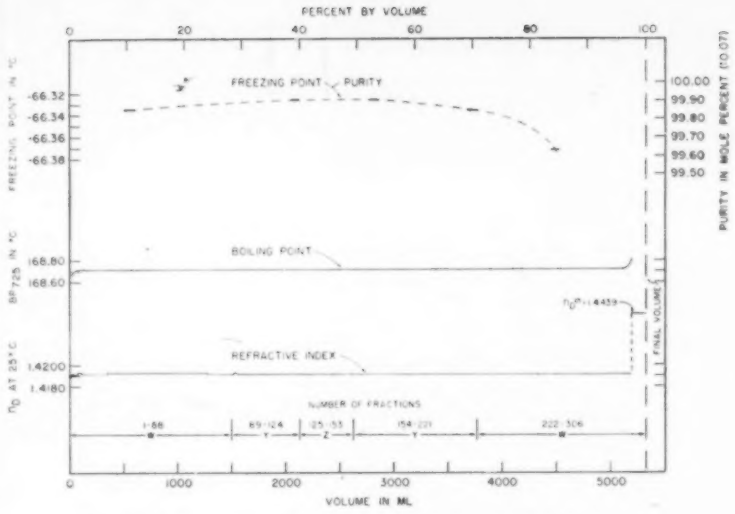

FIGURE 31. ***Second and final distillation of 1-decene.***
Regular distillation at 725 mm Hg in still 12A (10/27/47 to 1/12/48).

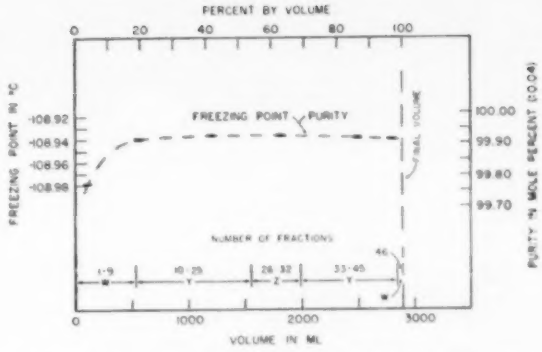

FIGURE 33. ***First and only distillation of 1,3-butadiene.***
Regular distillation at 1 atm in still 1A (10/8/47 to 11/28/47).

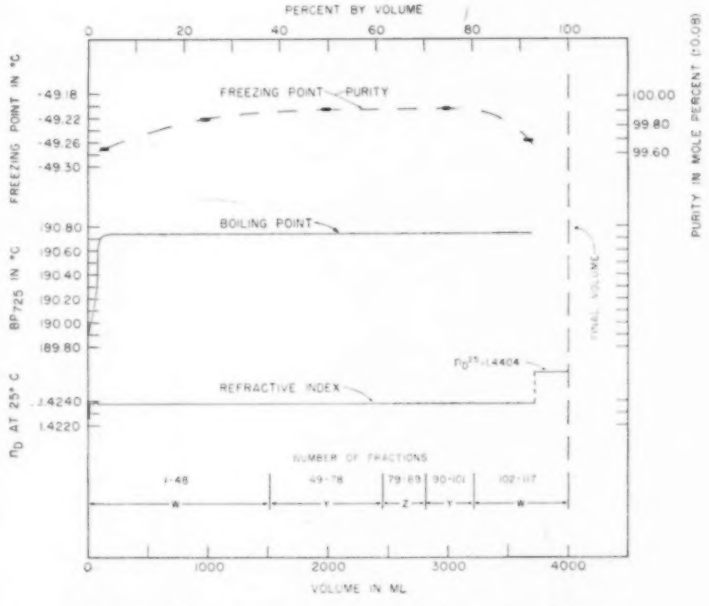

FIGURE 32. ***First and only distillation of 1-undecene.***
Regular distillation at 725 mm Hg in still 13 (4/20/48 to 5/12/48).

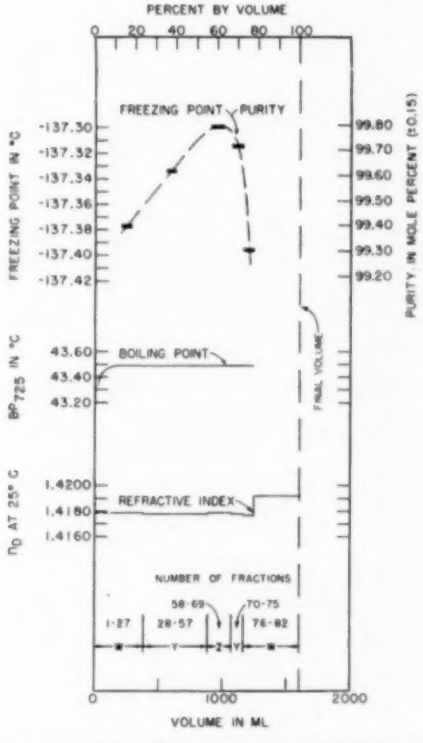

FIGURE 34. ***First and only distillation of 1,2-pentadiene.***
Regular distillation at 725 mm Hg in still 11A (7/14/48 to 8/3/48).

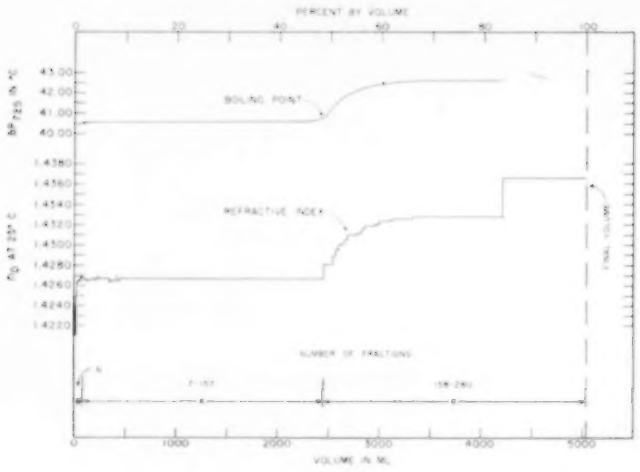

FIGURE 35. *First distillation of 1,3-pentadiene (cis+trans).*

Regular distillation at 725 mm Hg in still 9 (5/14/48 to 7/6/48). One of two similar distillations. See footnote 1 of table 1. Fractions 7 to 157 were redistilled to obtain 1,*trans*-3-pentadiene (see fig. 37), and fractions 158 to 280 were redistilled to obtain 1,*cis*-3-pentadiene (see fig. 36).

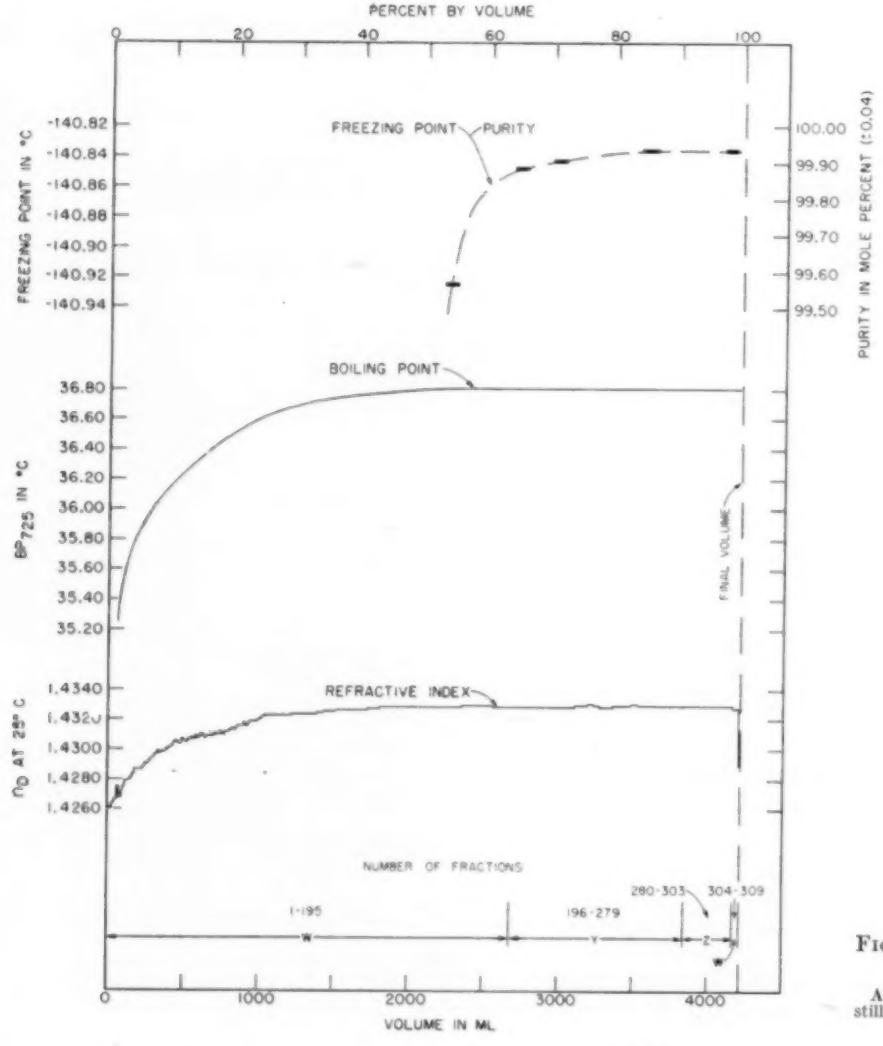

FIGURE 36. *Second and final distillation of 1,cis-3-pentadiene.*

Azeotropic distillation with methanol at 725 mm Hg in still 4 (9/30/48 to 11/23/48). See footnote m of table 1.

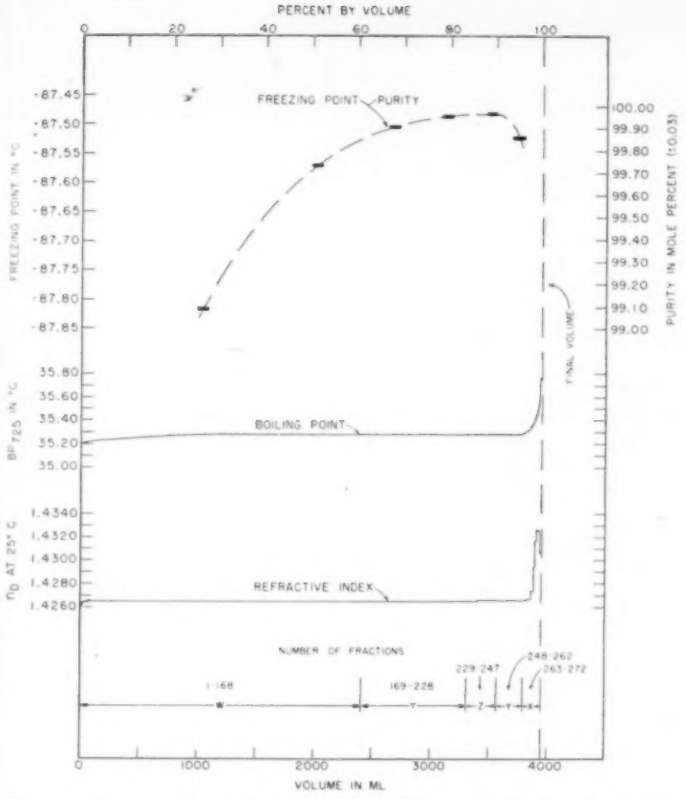

FIGURE 37. *Second and final distillation of 1,trans-3-pentadiene.*

Azeotropic distillation with methanol at 725 mm Hg in still 4 (8/11/48 to 9/28/48). See footnote m of table 1.

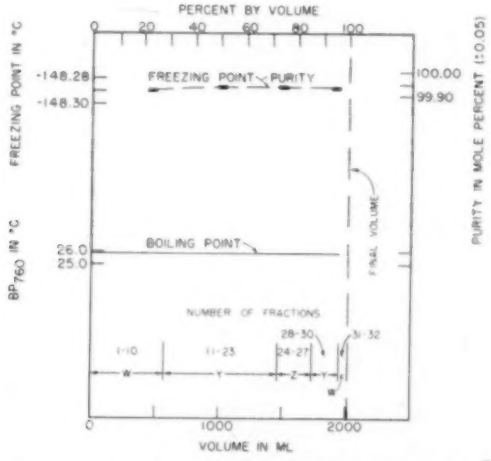

FIGURE 38. *First and only distillation of 1,4-pentadiene.*

Regular distillation at 725 mm Hg in still 1A(8/25/48 to 10/4/48).

FIGURE 39. *First and only distillation of 2,3-pentadiene.*

Regular distillation at 725 mm Hg in still 9(7/8/48 to 8/3/48).

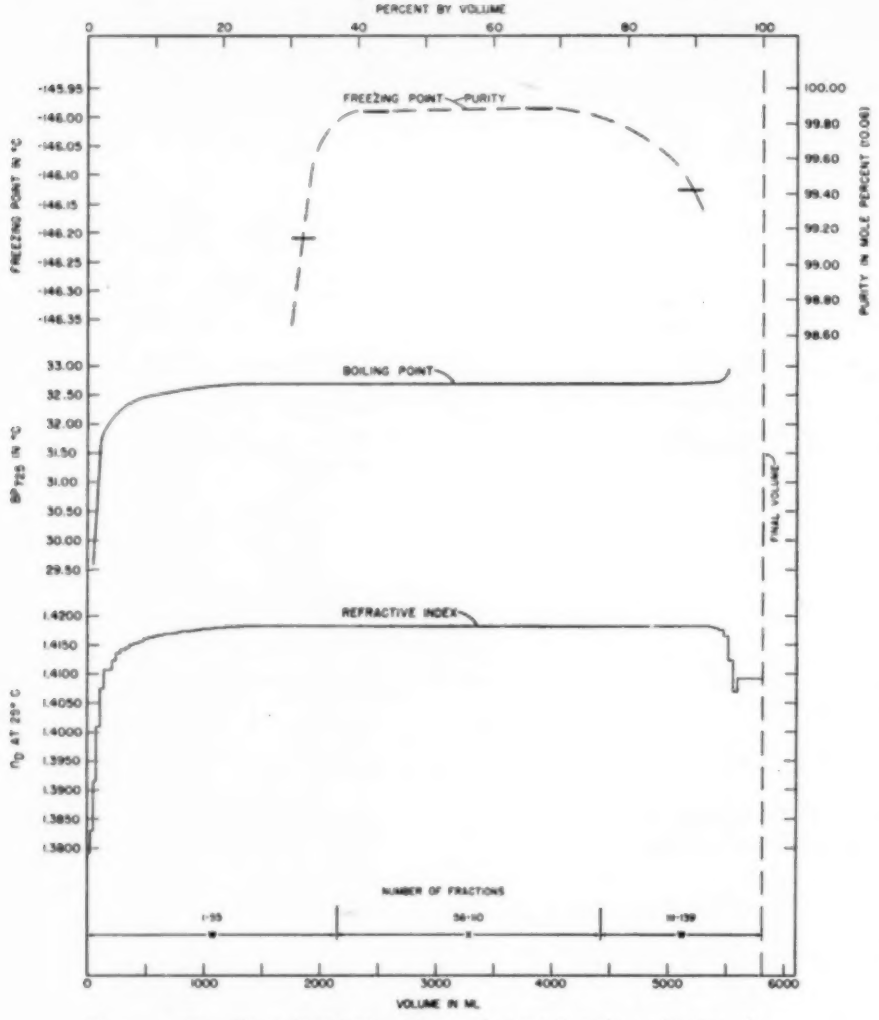

FIGURE 40. *First distillation of 2-methyl-1,3-butadiene (isoprene).*

Regular distillation at 725 mm Hg in still 13(1/20/47 to 2/20/47). One of two similar distillations.

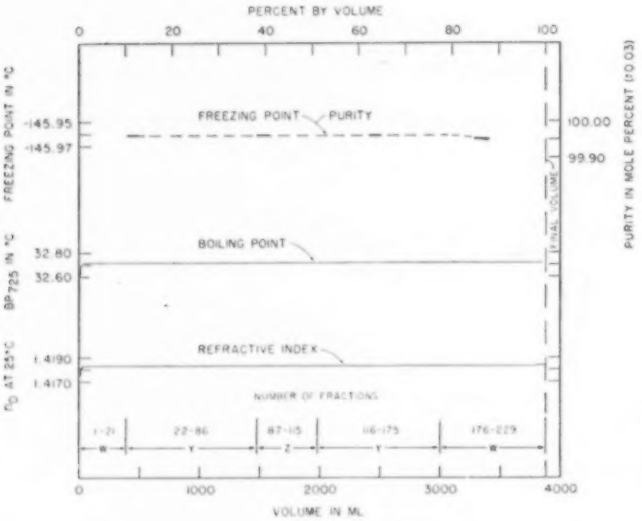

FIGURE 41. *Second and final distillation of 2-methyl-1,3-butadiene (isoprene).*

Regular distillation at 725 mm Hg in still 2A(10/7/47 to 11/17/47). See footnote 1 of table 1.

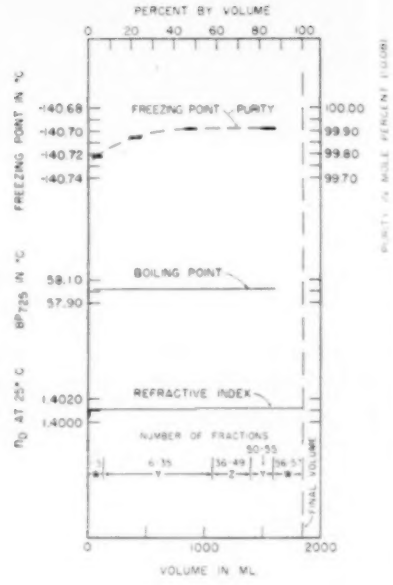

FIGURE 42. *First and only distillation of 1,5-hexadiene.*

Regular distillation at 725 mm Hg in still 13(11/7/47 to 11/25/47).

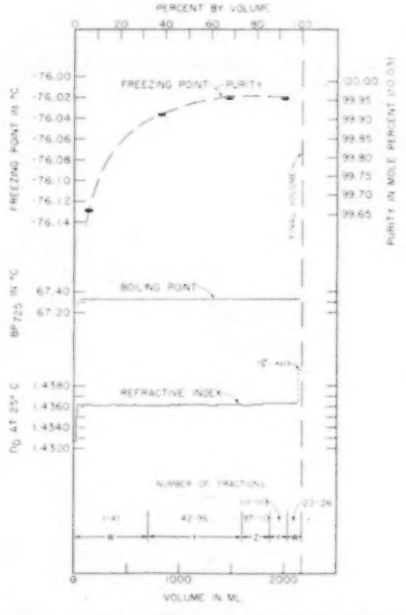

FIGURE 43. *First and only distillation of 2,3-dimethyl-1,3-butadiene.*

Regular distillation at 725 mm Hg in still 4(11/26/48 to 12/20/48).

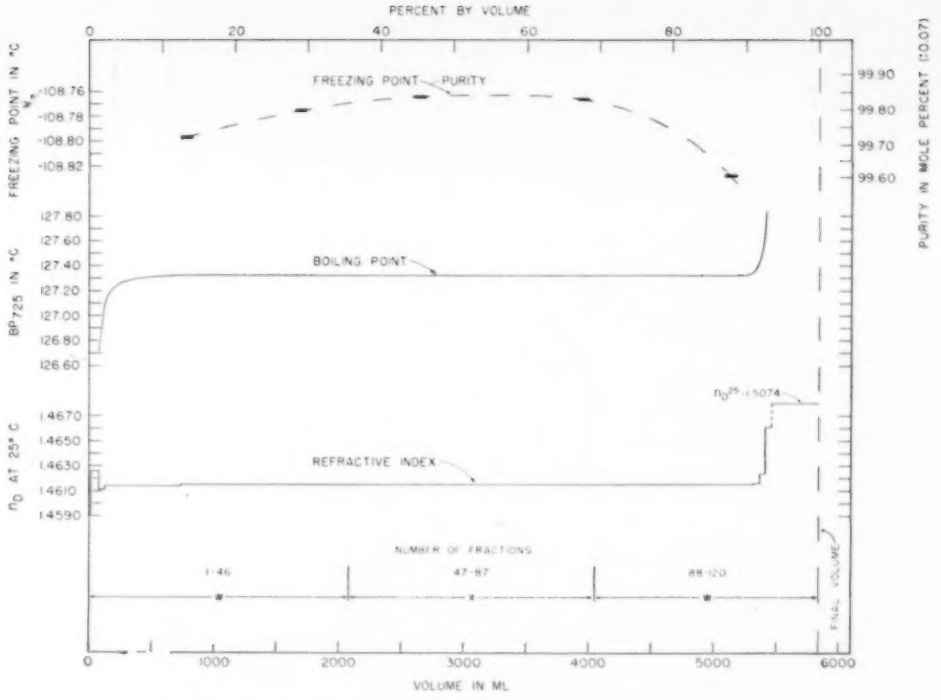

FIGURE 44. ***First distillation of 4-ethenyl-1-cyclohexene (4-vinyl-1-cyclohexene).***
Regular distillation at 725 mm Hg in still 14(12/2/47 to 12/23/47). One of three similar distillations.

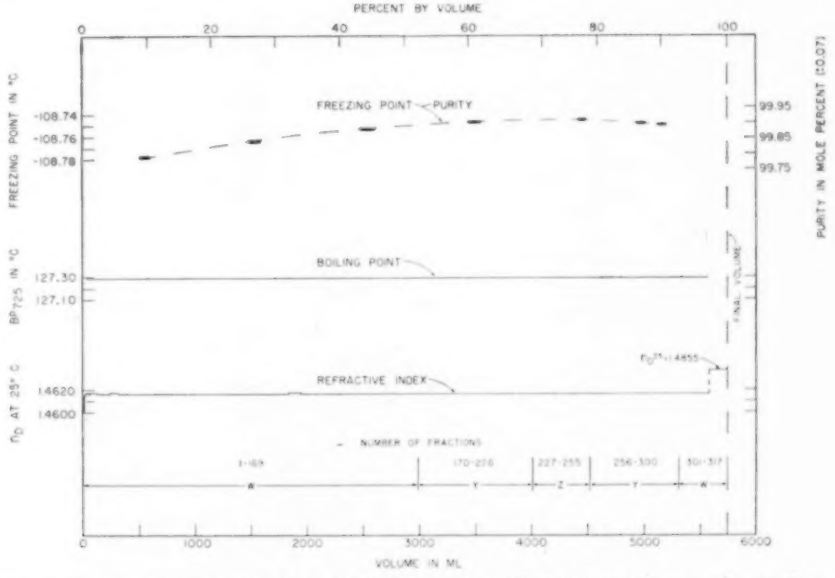

FIGURE 45. ***Second and final distillation of 4-ethenyl-1-cyclohexene (4-vinyl-1-cyclohexene).***
Regular distillation at 725 mm Hg in still 4(5/3/48 to 6/28/48). See footnote q of table 1.

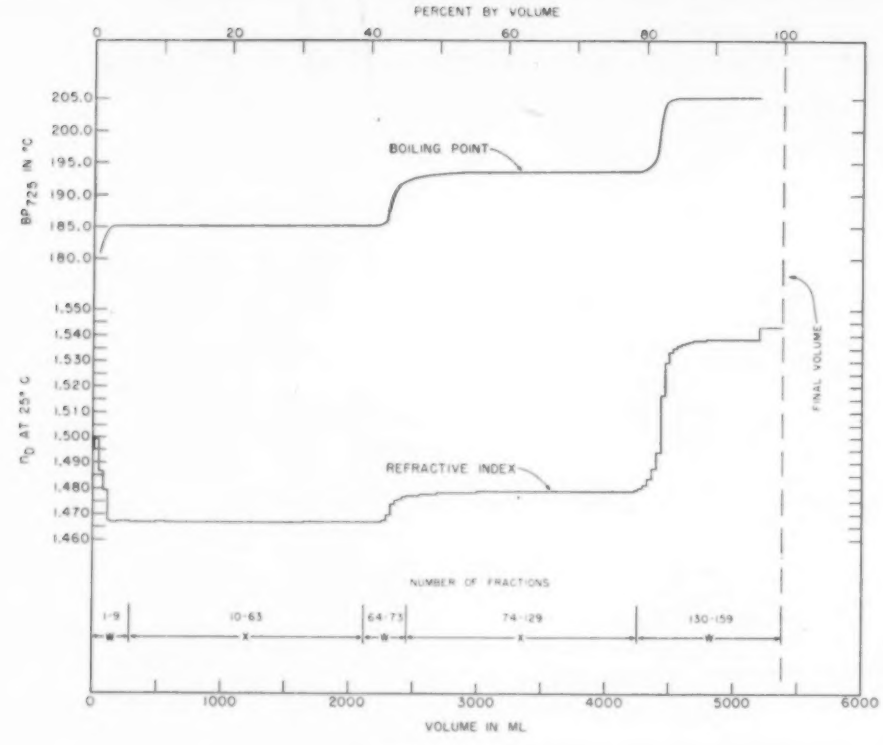

FIGURE 46. *First distillation of decahydronaphthalene (cis+trans).*

Regular distillation at 725 mm Hg in still 7(12/22/47 to 1/21/48). One of three similar distillations. See footnote s of table 1. Fractions 10 to 63 were redistilled to obtain *trans*-decahydronaphthalene (see fig. 48), and fractions 74 to 129 were redistilled to obtain *cis*-decahydronaphthalene (see fig. 47).

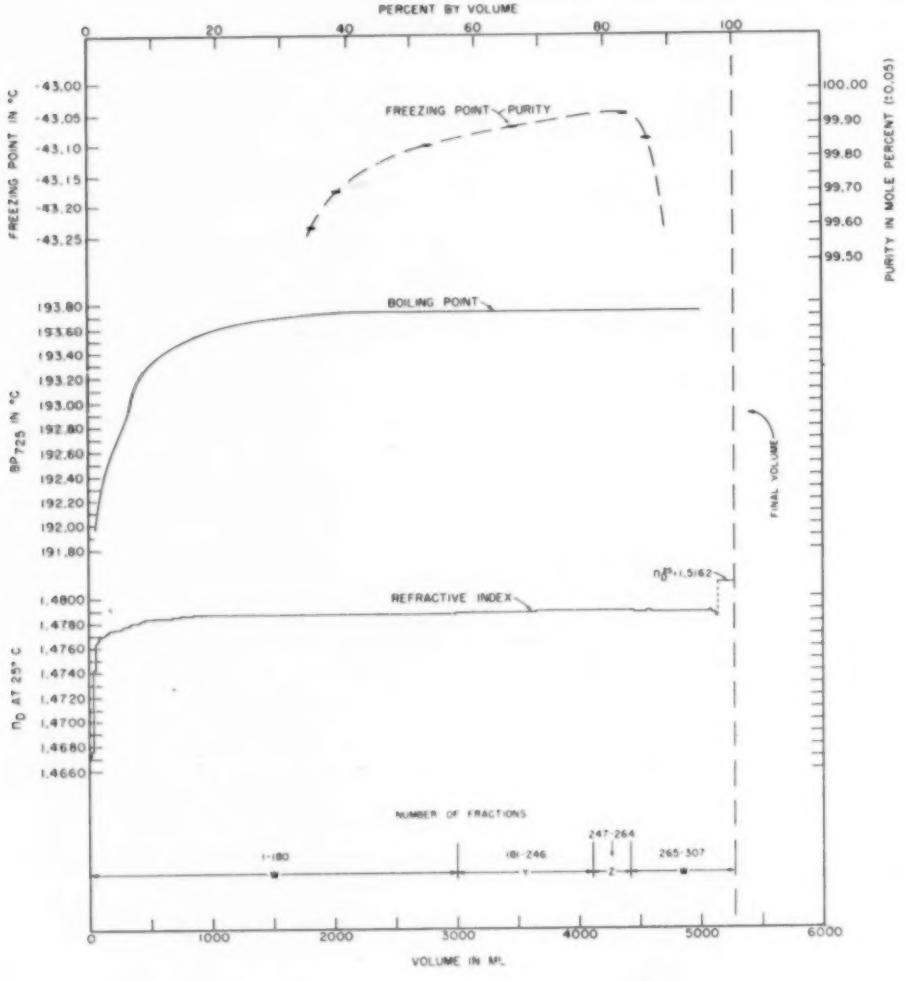

FIGURE 47. *Second and final distillation of cis-decahydronaphthalene.*

Regular distillation at 725 mm Hg in still 11A (5/10/48 to 7/12/48). See footnote t of table 1.

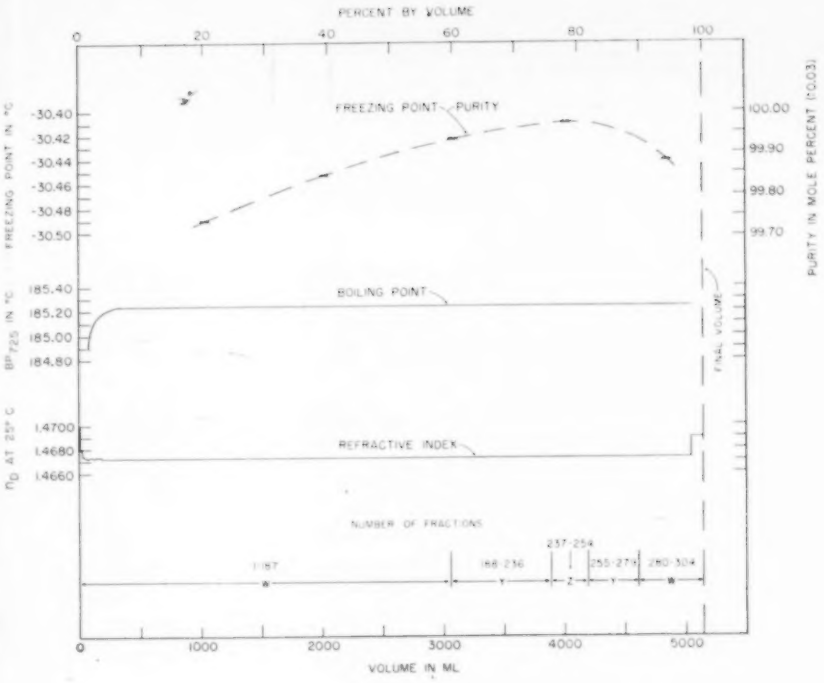

FIGURE 48. *Second and final distillation of trans-decahydronaphthalene.*

Regular distillation at 725 mm Hg in still 11A (3/16/48 to 5/10/48). See footnote t of table 1.

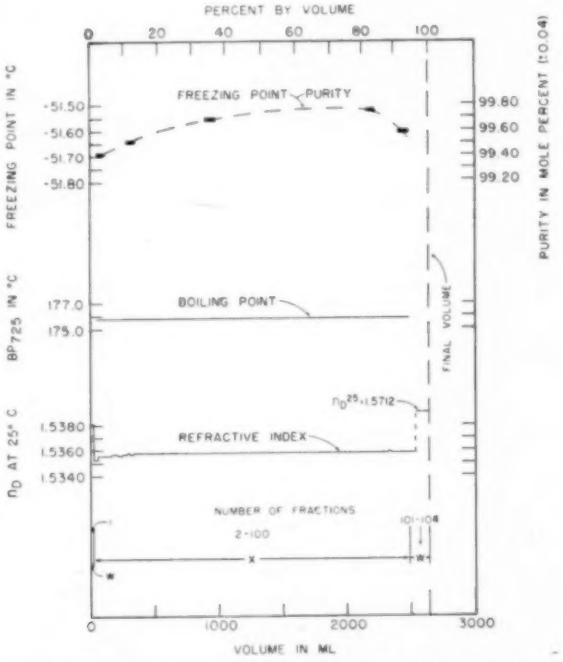

FIGURE 49. *First distillation of 2,3-dihydroindene (indan).*

Regular distillation at 725 mm Hg in still 12 (5/15/45 to 6/13/45).

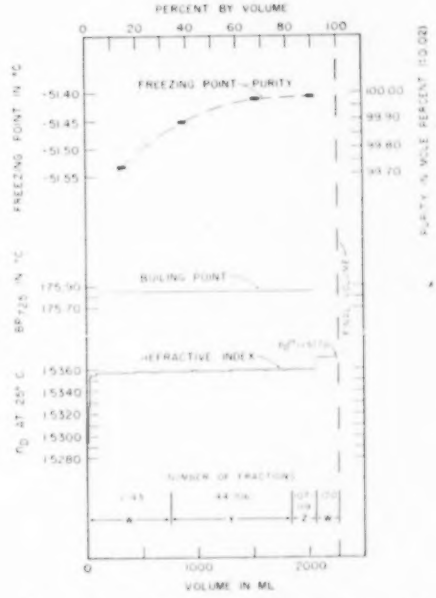

FIGURE 50. *Second and final distillation of 2,3-dihydroindene (indan).*

Regular distillation at 725 mm Hg in still 15A. (3/18/48 to 4/9/48).

WASHINGTON, May 8, 1950.

Contents

Journal of Research of the National Bureau of Standards Vol. 45, No. 2 August 1950

Page

Cotton powder for infrared transmission measurements. Florence H. Forziati, Walter K. Stone, John W. Rowen, and William D. Appel. RP2116. 109

Gravimetric analysis of exhaust gas from gas turbine combustion chambers. Fillmer W. Ruegg and Carl Halpern. RP2117. 113

Absorption of near-infrared energy by certain glasses. Jack M. Florence, Charles C. Allshouse, Francis W. Glaze, and Clarence H. Hahner. RP2118. 121

Tensile properties of ingot iron at low temperatures. Glenn W. Geil and Nesbit L. Carwile. RP2119. 129

Effects of pressure and other variables on determinations of octane number. William J. Levedahl. RP2120. 148

Creep of high-purity copper. William D. Jenkins and Thomas G. Digges. RP2121. 153

Purification, purity, and freezing points of twenty-nine hydrocarbons of the API-Standard and API-NBS series. Anton J. Streiff, Laurel F. Soule, Charlotte M. Kennedy, M. Elizabeth Janes, Vincent A. Sedlak, Charles B. Willingham, and Frederick D. Rossini. RP2122. 173

The above Research Papers may be obtained from the Superintendent of Documents, Government Printing Office, Washington 25, D. C., as follows: RP2116, 10¢; RP2117, 10¢; RP2118, 10¢; RP2119, 15¢; RP2120, 10¢; RP2121, 15¢; RP2122, 15¢.

For sale by the Superintendent of Documents, U. S. Government Printing Office, Washington 25, D. C. • Price 45 cents
$4.50 per year on subscription
UNITED STATES GOVERNMENT PRINTING OFFICE, WASHINGTON : 1950